# Instrumentation for the Control of Biological Function through Electrical Stimulation

by

Martina Charlotte Leistner

A thesis submitted to The Johns Hopkins University in conformity with the requirements for the degree of Master of Science in Engineering.

Baltimore, Maryland

May, 2016

# Abstract

Electrical signals play a vital role in the makeup and processing of biological systems. While crucial for desired biological functions, they are also directly involved in degenerative and undesirable activity in these systems. Controlling biological function through targeted electrical stimulation is possible in both non-excitable cells and excitable cells. For each cell type, instrumentation for one specific application is covered in the following.

Firstly, this thesis studies electrical stimulation setups and instrumentation for the enhancement of transgene expression in gene therapy. Although the applications of this work are manifold, the focus here is on improving wound healing and tissue regeneration, which is especially important in the treatment of non-closing wounds. Specifically, the ability of iontophoresis to enhance transgene expression in dermal and epidermal cells is assessed. For this, an electrical stimulation circuit with electrodes is developed and employed in *in vivo* experiments. The genes, in the form of charged DNA plasmids, are injected subcutaneously at the wound border of an adult rat model. An electrical field is applied to the tissue via the electrodes, which

forces the plasmids onto a trajectory and forms pores in the cell's membranes to enhance transfection. Various stimulation parameters and setups, as well as different luciferase encoding plasmids, are tested to determine the optimal experimental setup for transgene expression.

Secondly, this thesis studies neural implants for the excitation and inhibition of neurons. Neural implants are vital in the treatment of neurological diseases, and allow us to better understand how the brain processes information. The brain is a complex organ which is known to function by its multiple parts working together. Wireless sub-millimeter implants placed individually throughout the brain can imitate natural spatio-temporal stimulation patterns, while causing only minimal tissue destruction. In this thesis, the design of such an implant is elucidated in its entirety, with special focus on the wireless power link. Power from an external primary inductor will inductively be transferred to a secondary inductor that is implanted in the brain. The design trade-offs in selecting the geometry and configuration of the inductors are described and the analysis, simulation, and testing results are presented with the suggestion of an optimal design.

Primary Reader: Dr. Ralph Etienne-Cummings

Secondary Reader: Dr. Nitish Thakor

Tertiary Reader: Dr. John Harmon

# Acknowledgments

This Master's thesis is a result of my research conducted at Johns Hopkins University (JHU) in Baltimore, USA, while pursuing a M.S.E degree in Biomedical Engineering. Support from numerous individuals has helped make this thesis possible.

In particular, I am indebted to my advisor Dr. Ralph Etienne-Cummings, who provided me with the opportunity to conduct research at his lab, motivated me to make the impossible possible, and supported me in many ways, to Dr. Nitish Thakor thanks to whom I first came to JHU for my undergraduate research and who taught me how to design biomedical instrumentation, and to Dr. John Harmon who let me collaborate with his lab, allowing me to gather hands-on experience of how to bridge the gap between medicine and engineering. All three of them have provided invaluable guidance throughout my research and writing.

A special word of thanks is due to John Penn for the crucial input and support regarding inductor design, simulation, and measurement, to Adam Khalifa for the great team work on the micro-bead, and to Frank Lay for the wonderful collaboration and help regarding gene therapy.

ACKNOWLEDGMENTS

I would futher like to express my thanks to Dr. Andreas Andreou for allowing me to use his lab equipment, to Dr. Philippe Pouliquen for his invaluable help regarding inductor chip design, to Dr. James Wilson, Kerron Duncan and Milad Alemohammad for their insights regarding RF design and measurements, to Meg Chow for the teamwork on preliminary inductor studies, to Sathappan Ramesh for his help with equipment, and to Samantha Wang for her help regarding iontophoresis.

I am grateful to all members of the Computational Sensory-Motor Systems Lab, Harmon Lab, and Andreou Lab, including notably Jie (Jack) Zhang, Jamal Molin, Elliot Greenwald, John Rattray, Louis Born, Ali Karim Ahmed, Gaspar Tognetti and Martin Villemur, for their help in various ways.

Further, I would like to thank MOSIS for providing fabrication services, and Sonnet Software for providing me with software.

I would like to express my appreciation also to everyone else who assisted me, especially in the Department of Biomedical Engineering and in the Department of Electrical and Computer Engineering at JHU. In this regard, a special word of thanks goes to Sam Bourne.

Finally, I would like to thank my family and friends for their moral support at all times.

# Dedication

This thesis is dedicated to peace.

# Contents

# List of Tables

# List of Figures

# I

# Introduction

In order for an organism to be healthy and intact, it is vital that its cells work together, and that individual cells are effective at fulfilling their assigned functions. Certain diseases, or accidents, might, however, impose too great of a challenge and can either render cells ineffective in repairing or even make them counteractive and destructive.

Given the countless diseases that could be healed through a change in cell behavior, it is thus of great interest to find ways that can direct these cells back to fulfilling their function even in the face of additional challenges such as disease.

Electrical signals play a vital role in the makeup and processing of biological systems, and they can be changed by therapeutic electrical stimulation. The membrane potential of a cell is an electrical signal that affects the cell function, and it exists in every cell. When it is changed through electrical stimulation, cell properties such as the membrane barrier of non-excitable skin cells, or the spiking behavior of excitable neurons, are affected as a result of this. Even therapeutic methods that use drugs or gene therapy, can be enhanced by electrical stimulation to direct charged particles to a desired location.

A cell's genes or DNA sequences code for cellular processes and functions, making them an ideal target for changing cell behavior. One approach to doing this is introducing new genes into a cell's genetic code as gene therapy. Genes in the form of DNA plasmids can enter the cell's nucleus once they pass the barriers formed by the cell membrane and nuclear membrane. Appropriate electrical stimulation reduces the

barrier function of these membranes, allowing for the plasmids to enter the nucleus and thus to add to the cell's genetic material. Electrical stimulation in the form of iontophoresis can further direct the movement of the charged plasmids, thus allowing for targeted selection of the cells to be modified. The first part of this thesis presents instrumentation design and *in vivo* implementation for the electrical enhancement of cutaneous wound healing in gene therapy.

While electrical stimulation can modify cell properties of non-excitable cells, it can also directly affect the real-time behavior of excitable cells, e.g. causing excitation or inhibition of cells in the nervous system.

Excitable cells such as neurons or muscle cells react strongly and immediately to electrical stimulation. Neurons form the nervous system, and process and communicate information amongst each other in the form of electrical signals. Exciting or inhibiting neurons through electrical stimulation thus allows us to steer this behavior in a controlled way. This can be used to impose a state of healthy neural behavior or a certain state of mind onto the diseased or healthy brain. The second part of this thesis presents instrumentation in the form of neural stimulation implants and their wireless power supply for a holistic and minimally invasive approach to electrical stimulation of the brain.

Designing instrumentation for the control of biological function through electrical stimulation is best approached in four steps (figure 0.1): The theory tells us which laws and concepts are at play - thus, which results can be expected for a certain

approach. If any of the subsequent steps brings unexpected or undesired results, it is important to go back to the theory and to take more concepts, geometrical details, parametric deviations, etc. into account so that the theoretical model becomes a more accurate representation of the reality with respect to the desired functionality. This will allow to identify bugs, missing details, or allow for the discovery of new effects at play, thus lead to a better product. Simulation is the numerical analysis of a theoretical model and allows us to verify the intuitive expectations made based on the theory. It determines which results can be expected according to the theory that was included into the model. The simulation can only be as accurate as the model is. Bench top experimentation verifies whether the numerical simulation model is a good representation of the dominant effects occurring in reality, thus is a first test to see if the designed instrumentation actually works. *In vivo* experimentation is the final stage in the design of biomedical instrumentation to see if the design works in the environment that it was made for, and further, whether it has the desired effects on the biological organism. This experimentation setup includes the typical variations of geometrical values and electrical parameters that occur *in vivo*. All natural laws and effects at once are at play, making it a scenario that is more detailed and complex than any numerical simulation could model.

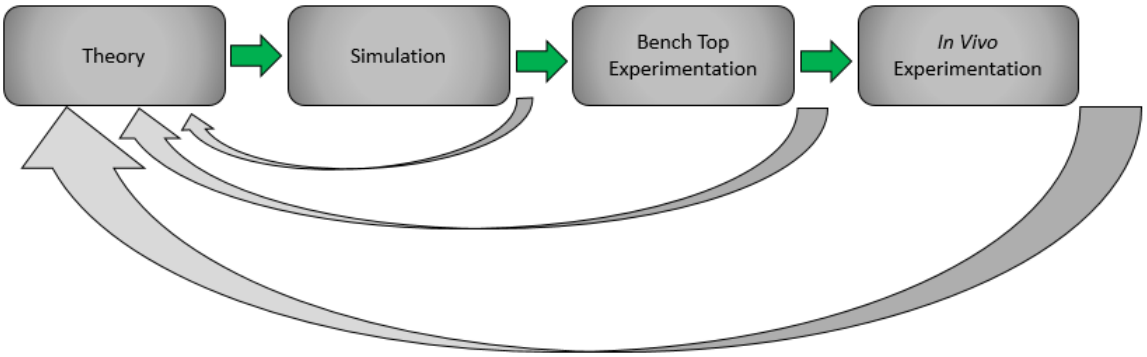


**Figure 0.1:** Four steps in the design of instrumentation for the control of biological function through electrical stimulation.

# II

# Electrical Stimulation in Gene Therapy

# Chapter 1

# Introduction

## 1.1 Motivation

Gene therapy is the modification of a cell's genetic material by therapeutic delivery of nucleic acids to the cell nucleus, and has many applications[16] including the therapy of AIDS,[17] Alzheimer's Disease,[18] cancer[1920] , cystic fibrosis,[21] sickle cell disease[22] and cutaneous wounds.[23]

Non-healing wounds show delayed wound healing when treated with conventional methods, which can put the patient at high risk: open wounds compromise the mechanical protection of the underlying tissue, impair the use of the affected body part, are prone to infection and can cause pain. Non-healing wounds often occur in the case of diabetic foot lesions, arterial insufficiency ulcers, compromised skin grafts or musculo-cutaneous flaps.[24] Elderly patients, or those with diabetis are especially af-

fected. The transcription factor Hypoxia Inducible Factor - 1 (HIF-1) plays a major role in wound healing. It mobilizes and homes progenitor cells to the wound where they promote wound healing. Wound healing was shown to be improved by increasing levels of HIF-1[25][26] . It is, however, required that the peptide transcription factor HIF-1 is delivered via DNA instead of directly, since dermal peptidases destroy such peptides rapidly. The respective DNA could be delivered using viral vectors, but such therapy often leads to immune system responses, rejection, and is prone to causing gene mutation of existing genetic cell material. Non-viral methods such as the use of DNA plasmids are more accepted, but often require additional methods to overcome the barrier function of the cell's membranes in order to allow for the entering of the rather large plasmid DNA. Applying an electrical field to a cell reduces the barrier function of its membranes and is thus a suitable approach. Such electrical stimulation has the additional advantage of enhancing wound healing even when no gene therapy is involved[27][28] . This makes it especially interesting compared to other techniques such as e.g. applying mechanical pressure. Electroporation - pore induction in the cell's membrane due to the application of high voltage (200 V - 1200 V) pulses - was shown to be effective for transfection enhancement.[29] It is applied locally in order to maximize (within limits) the voltage across individual cells and therefore less suitable for large wounds. Although it is only applied for durations on the order of milliseconds, the high voltages used pose additional risks, including electrical shock, pain and tissue damage. Iontophoresis refers to the application of a defined current

at comparably low voltages (10V - 50V) - usually for a duration on the order of minutes - and could overcome these issues. Under the assumption that each cell has the same impedance, a defined current could ensure a defined voltage drop over each cell while this would depend on the total number of cells in the case of a defined voltage. This makes iontophoresis especially suitable for therapy devices that treat wounds of different sizes. The possibilities and challenges of this transfection enhancement method are examined for intradermally injected luciferase plasmid, and appropriate instrumentation is developed.

## 1.2 Prior Art

While electroporation[30] has been used extensively for improving DNA plasmid transfection , there is very little prior experience with iontophoresis. For iontophoresis, the sole publications describing naked plasmid transfection were for the retina.[31] The other significant publication describes the use of cationic nanoparticles in conjunction with iontophoresis to deliver DNA to the dermis.[32]

In contrast to the limited experience with DNA plasmid transfection, iontophoresis has been used extensively in other fields. This includes the treatment of hyperhidrosis,[33] glucose monitoring,[34] the delivery of antibiotics[35] or local anesthetics.[36] The effects of alternating current iontophoresis on drug delivery have also previously been studied.[37]

Existing electrical current stimulation devices for iontophoresis include programmable devices,[38] or the commercial Lectro Patch device (General Medical Co., CA), GlucoWatch Biographer (Cygnus Inc., CA), LidoSite Topical System (Vyteris, Inc., NJ), IONSYS E-TRANS system (Alz Corp., CA) or Numby Stuff Phoresor system (Iomed, Inc., UT).[39]

# Chapter 2

# Background

## 2.1 Gene Therapy

In gene therapy, genetic material is introduced into a cell where genes encode for proteins. Viruses do this too, and thus viral vectors can be used to deliver such genetic material. There is, however, a high risk of this leading to undesired and dangerous mutations. Non-viral vectors can also introduce genetic material into the cell, and have the advantage that they involve a much lower chance of mutations happening. Plasmids are an example of such non-viral vectors. They are circular self contained genetic structures and can encode for proteins. Chemical enhancers, physical pressure, ultrasound, electroporation, iontophoresis, gene gun can all enhance gene delivery of plasmids.[40]

## 2.2 Skin

The skin is a large organ that forms a protective barrier around most of our body. It separates the environment within the body from that outside of it and plays an important role in the regulation of body processes and sensing. Various layers containing cells and extracellular matrix form the skin. The surface of the skin is formed by the epidermis which is an avascular layer that receives blood supply from the dermis and acts as a protective barrier against the outside environment. The stratum corneum is the top layer of the epidermis and is formed by dead cells. It is highly resistive and impermeable[41] and prevents the loss of body fluids as well as the entry of foreign substances. Below the epidermis lies the dermis which controls infection, provides nutritional support to itself and the epidermis, thermoregulation through its superficial vasculature, and sensation through its nerve receptors. Subcutaneous tissue, or hypodermis, is loose and fatty connective tissue lying below the dermis that contains large blood vessels and nerves. Skin appendages such as sweat glands, fingernails and toenails, and hair are also part of the skin. In addition, various substances produced by the various cell types of the skin are present in the skin.[42] Usually, a muscle layer lies below these layers of skin.

## 2.3 Wound Healing

Cutaneous wounds of any size compromise the barrier function of the skin and can lead to pain, infections, major disability or in the extreme cases even death. It is therefore of major importance to achieve wound healing in a timely manner after a wound occured in order to restore the original structure, form and function of the skin after a wound occured.[42]

The process of wound healing can be divided into four phases: 1.coagulation and haemostasis, 2.inflammation 3.proliferation and 4. wound remodeling with scar tissue formation. The extracellular matrix and action of growth factors and cytokines, as well as various cell types are involved in wound healing.[43] The Hypoxia-inducible factor-1 (HIF-1) transcription factor plays an important role in wound healing by mobilizing and homing progenitor cells to the wound where they promote wound healing. It regulates oxygen homeostasis and contributes to all stages of wound healing by affecting growth factor release, matrix synthesis, cell division, cell migration and cell survival under hypoxic conditions.[44]

Wound healing can be enhanced in various ways, including through electrical stimulation directly[27][28] .

It is to be noted, that while wound healing in rats does not perfectly mimic human skin wound healing due to different skin morphology (e.g. rats are loose-skin animals, while humans have a tight skin), rats are still a good animal model for wound healing due to their wide availability, the broad knowledge base on rat wound healing, and

their small size which, however, is large enough to provide a suitable area of skin for wound studies.[45]

# Chapter 3

# Methods

## 3.1 Iontophoresis

Iontophoresis[46] refers to the application of a defined current (and sometimes erroneously to the application of a low voltage between around 10 V and 50 V) to deliver charged molecules. The concept behind iontophoresis is that the charged molecules will form part of the defined current, thus leading to a movement of these molecules to the desired location. An increased current would correspond to an increased movement of these charged molecules (either more molecules at once, or faster movement of same number of molecules). While iontophoresis usually involves a DC current, there are also cases of AC iontophoresis, e.g. studied in human epidermal membrane.[47]

Electroporation refers to the application of high voltage pulses of around 200 V to 1200 V to form aqueous pores in the cell membrane under high membrane

potentials, as can be seen in figure 3.1. Iontophoresis is believed to also sometimes lead to the formation of such pathways, however, dependent on the resulting membrane potentials, and usually in hair follicles and other appendages[2] . Both methods use electrical stimulation of biological tissue to enhance the delivery of substances, such as drugs, and they are compared in figure 3.2.

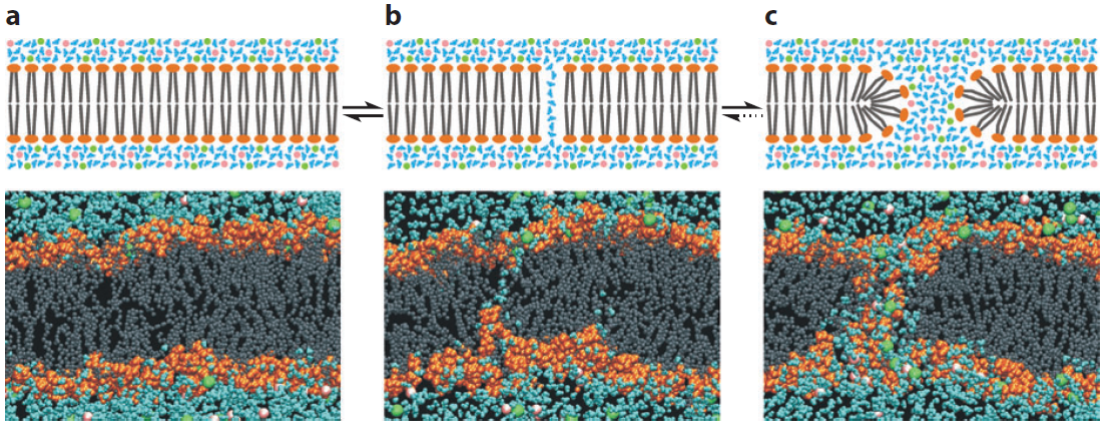


**Figure 3.1:** Formation of aqueous pores scheme and simulation. **a)** Intact bilayer membrane; **b)** Water molecules start penetrating the bilayer and form a water wire; **c)** Lipids adjacent to the water reorient their polar head groups to the water wire. This stabilizes the water wire and allows other polar molecules to enter. An aqueous pore is formed.[1]

## 3.2 Electrode-Tissue Interface

In order to inject a direct current (DC) into the tissue, resistive or faradayic stimulation is needed. In the metal of a current source, the charge is carried by electrons. Current in the biological tissue, however, is in the form of ions such as sodium, potassium or chloride, and the tissue can thus be seen as an electrolyte.

| | iontophoresis | electroporation |
|---|---|---|
| Primary mechanism | electric force on drug: electrically charged drug (ion) becomes part of current flow and migrates towards electrode of opposite polarity | permeabilization of skin: voltage across cell leads to formation of aqueous pores in membrane and thus new pathways for drug to enter |
| Secondary mechansim | formation of pathways in appendages (e.g. hair follicles) of skin | electric force on drug |
| defined electric parameter | current | voltage |
| typical waveform | DC | square wave pulses |
| typical resulting voltage amplitude | << 100 V [such as 10 V - 50 V] | > 100 V [ such as 200 V - 1200 V] |
| typical duration (on order of) | minutes | milliseconds |
| reversibility of skin | reversible at low current density | reversible at low pulse voltage |
| used extensively for | delivery of other drugs (not DNA plasmids) | improving DNA plasmid transfection |

**Figure 3.2:** Comparison of Iontophoresis and Electroporation.[2]

During stimulation, a transduction of charge carriers needs to occur at the interface between metal and electrolyte. This occurs in the form of electrochemical reactions along the interface, with reduction occuring at the negative electrode and oxidation occuring at the positive electrode. The exact reactions depend on the materials involved. Water is, however, usually present. The reactions for water are given below.[48] The reduction of water occurring at the negative electrode is

$$2H_2O + 2e^- \rightarrow H_2 \uparrow + 2OH^- \tag{3.1}$$

and the oxidation of water at the positive electrode is

$$2H_2O \rightarrow O_2 \uparrow + 4H^+ + 4e^- \tag{3.2}$$

The use of gel electrodes and electrolyte gel allows for a metal to electrode-electrolyte interface that is independent of the tissue, while the tissue-gel interface can be optimized for types of electrolyte transfer. Possible toxic reaction substances at the metal interface resulting from the metal are thus not touching the tissue. Such electrodes and gels provide chemical buffers, increasing the chance of reversible chemical reactions. The use of electrolyte gel further allows for an increase in surface area of the electrode tissue interface, since it can fill little gaps and rough surfaces. This makes for a lower resistive connection. The use of adhesive electrolyte gel has the additional advantage of sticking the electrode onto the tissue, thereby securing it in place.

## 3.3 Thermal Imaging

Current flow through the resistive tissue leads to power dissipation and thus heat generation where the current flows. Infrared cameras[49] capture the infrared thermal radiation radiated by objects with a non-zero Kelvin temperature. They can thus be used to determine where the tissue heats up and could thereby indicate the path of current flow in the tissue.

## 3.4 Improved Howland Current Source

The Howland current source is a biphasic voltage controlled current source and is a popular choice for stimulation in biomedical applications. It is simple yet precise and has comparable performance to more complicated current sources.[350] In order to increase the voltage range and thereby make it suitable for higher load impedances, as well as to reduce power consumption, an additional resistor can be introduced to the design, leading to the Improved Howland current source[3] seen in figure 3.3. It is stable and biocompatible. The Improved Howland current source has a positive and a negative feedback path. These are balanced when the resistors are matched according to the following equation:[3]

$$\frac{R_4}{R_3} = \frac{R_{2A} + R_{2B}}{R_1} \tag{3.3}$$

In this ideal case, the Improved Howland current source has a fully differential input. In order to avoid unnecessary distortion in the case of slight deviation in the matching, it is, however, recommended to drive only one input and ground the other one. This is based on the fact that the different input terminals depend on different resistors. Grounding the negative input terminal $V_{in-}$ and driving the positive input terminal allows for a positive transconductance. The output current is thus controlled by the input voltage according to the following equation:[3]

$$i_{out} = v_{in+} \cdot \frac{R_{2A} + R_{2B}}{R_1 \cdot R_{2B}} \tag{3.4}$$

In the case of $R_1 = R_{2A} + R_{2B}$ (and thus, according to equation 3.3, $R_3 = R_4$), this results in:

$$i_{out} = v_{in+} \cdot \frac{1}{R_{2B}} \tag{3.5}$$

Given an operational amplifier with a saturation voltage of $V_{sat}$, and given a range of load resistances $Z_L \in [R_{L_{min}}; R_{L_{max}}]$, the maximal output current through the load can be calculated using:[3]

$$i_{out_{max}} = \frac{v_{sat}}{R_{2B} + R_{L_{max}}} \tag{3.6}$$

This is based on the fact that the output current is supplied by the output of the operational amplifier and thus needs to pass the resistor $R_{2B}$.

The resistor values can be chosen based on the above equations. It should be taken into consideration, that the source impedance of the voltage source driving the Howland current source is in series with the resistor $R_1$.[3] Also, the resistors $R_1$, $R_{2A} + R_{2B}$, $R_3$ and $R_4$ should be much larger than the driven load resistance, since the circuit will otherwise be unbalanced and will no longer function correctly.

A feedback capacitor can be added in the negative feedback loop,[51] parallel to $R_4$, for stability compensation which is especially useful when driving a capacitive load.

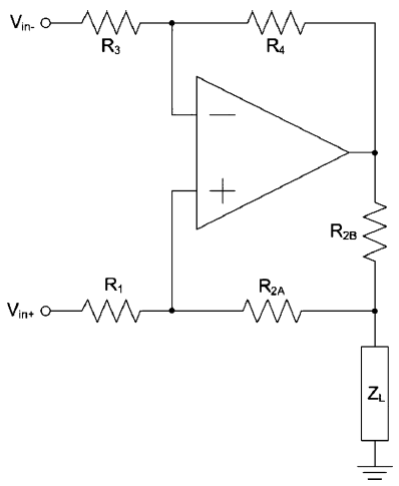


**Figure 3.3:** Improved Howland current source.[3]

## 3.5 Numerical Tissue Simulation

In order to analyze the path of current flow in the tissue for different electrode geometries, simulation of a numerical skin model can be performed for current stimulation.[4] The local current density distribution depends on the geometrical setup, and on the electrical parameters of the various structures. Rat skin can be modeled as a stack up of the conductive layers seen in figure 3.4 and the electrolyte gel can be modeled with a conductivity of around $\sigma = 4S/m$.[52] This tissue model accounts for DC tissue properties (conductivity), however, further complexity (dielectric constant $\epsilon$ ) is required to model the capacitive properties of the tissue in the AC case. The equivalent circuit of skin includes a resistor in series to the parallel connection of a resistor and a capacitor, as is shown in figure 3.5. This reduces to a series connection of two resistors in the DC case, but the capacitor comes into play and decreases the

magnitude of the impedance at higher frequencies.

| Skin Layer | Thickness [um] | Conductivity [S/m] |
|---|---|---|
| Stratum Corneum | 20 | 0.003 |
| Epidermis | 250 | 0.2 |
| Dermis | 1000 | 0.2 |
| Subcutaneous Tissue | 650 | 0.05 |

**Figure 3.4:** Model of rat skin.[4] The conductivity of the stratum corneum is around 30 times higher than in real rat skin.

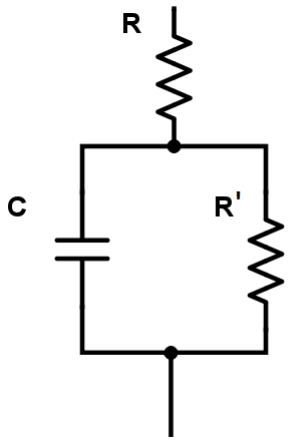


**Figure 3.5:** Equivalent circuit model of skin.[5]

# Chapter 4

# Experimental Setup

## 4.1 Simulation

### 4.1.1 Improved Howland Current Source

The Improved Howland current source is designed in LTspice, as shown in figure 4.1.

Based on preliminary *in vivo* experiments with a commercial DC current source, a load impedance of up to $10k\Omega$ is determined for the rat as the load (voltage drops of up to 20 V were seen for a 2 mA current). Accordingly, higher resistor values are chosen for each branch of the Improved Howland current source to ensure balancing of the current source. This is done with the help of simulations and with a safety margin that accounts for unexpected increases above this determined load impedance. The

resistors $R_3$, $R_4$ and $R_{2A}$ are chosen to be $100k\Omega$. The resistor $R_{2B}$ is chosen to be $1k\Omega$, which (according to equation 3.5) leads to a transfer function of the Improved Howland current source that converts an input voltage in volts to an output current in mA of the same number. Given the maximal function generator output amplitude of 10 V (for the function generator which is used for the experimentation), this would lead to a maximal output current amplitude of 10 mA. In order to fulfill the matching condition given by equation 3.3, $R_1$ is chosen to be $101k\Omega$, and formed by a series connection of a $100k\Omega$ and $1k\Omega$ resistor.

Various load conditions are evaluated using simulation.

### 4.1.2 Current Measurement Circuit

In order to allow for the verification of a correct current flow through the load of the Improved Howland current source, the photodiodes of two optocouplers are connected in series to the load, right at the output of the Improved Howland current source. These photodiodes are connected in parallel to each other, with opposite polarity to allow for the detection of current flow in both directions.

When a current flows through one of the photodiodes (the direction of the output current determines through which photodiode it flows) the phototransistor corresponding to this diode will drive a current. This assumes that the phototransistor is powered, e.g. with a supply of 5 V. A pull-down resistor of $100\Omega$ connected in series to the phototransistor registers this current by showing a voltage drop. This

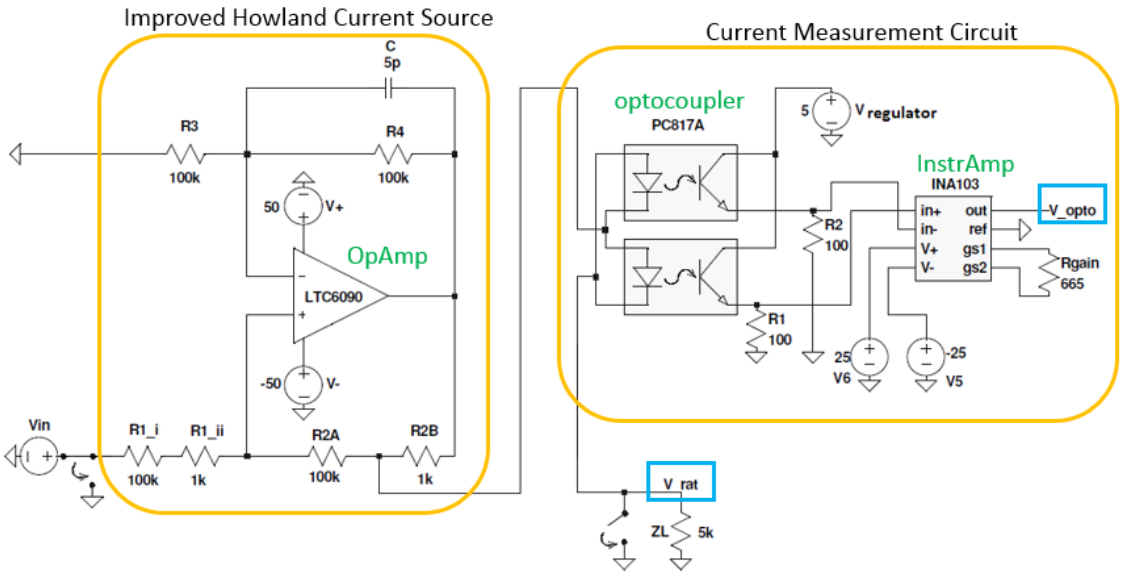


**Figure 4.1:** Circuit model designed and simulated in LTspice: The Improved Howland current source (left) and the current measurement circuit with an optocoupler (right) are shown. The input of the Improved Howland current source can be grounded, or connected to a voltage input signal $V_{in}$ with a switch. The corresponding output current of the Improved Howland current source passes the optocoupler and then goes through the load impedance $Z_L$ (which represents the rat) to ground. The load impedance can be shorted with a parallel switch to avoid current flow through the load. Resistance values are given in Ω (e.g. 1k corresponds to 1kΩ), voltage values are given in volts. Locations at which voltages are measured in the bench top and *in vivo* experiments are encircled in light blue. A 5kΩ load impedance is connected here instead of a rat. On the PCB, the optocoupler is different from the one used here, and the 5V supply to the phototransistors is provided by a regulator that downregulates 25 V to 5 V.

voltage drop is amplified by an instrumentation amplifier. The pull-down resistor that corresponds to the photodiode which lets positive current pass is connected to the positive input terminal of the instrumentation amplifier. The pull-down resistor that corresponds to the photodiode which lets negative current pass is connected to the negative input terminal of the instrumentation amplifier. As such, the output voltage measured at the output of the instrumentation amplifier corresponds to the amplitude and polarity of the output current of Improved Howland current source which flows through the load. The gain of this current measurement circuit, however, is amplitude dependent due to the optocoupler's non-linear gain, but this can be accounted for by documenting which output corresponds to which current flowing through a defined resistor (like a look-up table).

The optocoupler setup ensures that the current measurement does not affect the output current through the load in any way.

### 4.1.3 Current Density in Tissue

COMSOL Multiphysics is used to simulate the current density in a tissue model as defined in figure 3.4, with square electrodes of a size of 2.5 cm x 2.5 cm, as well as long small electrodes with a size of 2.5 cm x 1 cm (and one rounded edge as seen by the outline in figure 5.1 B). These electrodes are placed 7 mm away from the wound border of a 8 mm diameter wound which is modeled as air. A 4 mA DC current is applied through the electrodes that are touching the skin of the 8 cm diameter

cylinder skin model based on figure 3.4. The resulting current density is plotted at slices parallel to the skin surface, leveled at the height of the middle of each respective skin layer.

## 4.2 Bench Top Experimentation

The assembled printed circuit board (PCB), with two copies of the Improved Howland current source and the corresponding current measurement circuits, is shown in figure 4.2. The circuit hardware implementation is greatly based on the LT spice simulations.

### 4.2.1 Improved Howland Current Source

The resistors forming the Howland current source are hand selected for improved matching. The power handling capacity of $R_{2B} = 1k\Omega$ is chosen to be 1/4 Watts which corresponds to a maximal current of $I = \sqrt{(\frac{P}{R})} = 15.8mA$ going through $R_{2B}$ and thus through the load. The resistor $R_{1_{ii}}$ on figure 4.1 is implemented as a $2k\Omega$ potentiometer that can be tuned to the resistance of $R_{2B} = 1k\Omega$ to allow for improved ability to meet the matching condition of equation 3.3).

A tunable feedback capacitor (TZB4Z250BA10R00, 4 - 25 pF, Murata Electronics North America) is chosen for the feedback loop to allow for dynamic adaptation of the compensation (it is kept fixed at its factory value here, due to good performance).

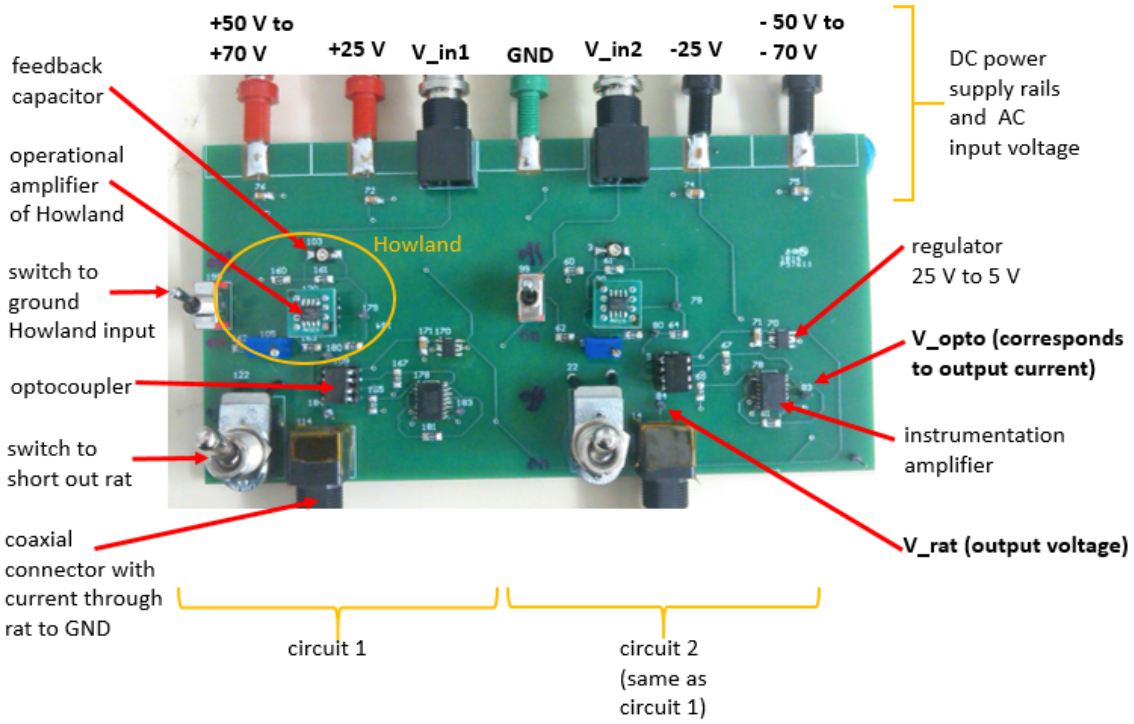


**Figure 4.2:** Two Improved Howland current source stimulation circuits ('Howland') with current measurement circuits including optocoupler, instrumentation amplifier and regulator, on a PCB.

The operational amplifier LTC6090 (Linear Technology) is chosen based on its dual supply with high voltage rails of up to $\pm 70V$, while allowing for a relatively high bandwidth with a slew rate of $21V/\mu s$ and high output current of up to 50 mA. The high voltage rails are of special importance when driving current into a high impedance load.

### 4.2.2 Current Measurement Circuit

The optocoupler ILD615 (Vishay Semiconductors) is chosen. It contains two optocouplers in the same DIP8 package, which ensures the same gain characteristics for both optocouplers here. This is important for comparing the magnitude of current in each direction. Maximal forward current, forward voltage drop voltage, reversal break voltage and bandwidth were taken into account when choosing the optocoupler in order to guarantee good performance without breaking.

The regulator MC78L05ABDR2G (ON Semiconductor) is used to provide a 5 V supply to the phototransistors of the optocoupler by down-regulating 25 V to 5 V.

The instrumentation amplifier INA103 (Burr-Brown) is used, which is chosen based on its low input current, appropriate bandwidth, low noise and low distortion.

**Consideration of Alternative Approaches for Current Measurement:** A shunt resistor could have been used instead of the photodiodes and optocouplers etc. It would either be connected between the load and the ground, or between the output of the current source and the load. The first case would have led to not grounding the

load (rat), as well as possible distortions of the ground. The second case would have created great challenges in measuring the voltage across it, which is due to the fact that the ground connectors of the oscilloscope probes are connected to earth ground: Measuring a voltage drop across a resistor that is not grounded on either side directly with an oscilloscope, can only be correctly achieved by calculating the difference of two measured signals (thus not connecting the ground connector of the oscilloscope to the resistor, which would ground that point). Using an instrumentation amplifier to amplify this voltage drop would output a voltage with respect to ground that is an amplified version of the drop across the resistor. Again, problems can arise in either case, due to the high offset voltage at the location of the resistor which is caused by a high voltage drop across the load. (This voltage drop is limited by the output voltage of the operational amplifier (opamp) of the Improved Howland current source (which is almost $\pm 70V$ for the opamp used here.) Subtracting two oscilloscope measurement signals would lead to imprecise measurements due to the high offset voltage. Instrumentation amplifiers used to amplify the small voltage across a small resistor would see a high common mode voltage corresponding to the voltage across the rat. Instrumentation amplifiers found on the market did not allow for common mode input voltages as low as -70V while having minimal input bias current. (Significant input bias currents would decrease the current flowing through the load which must be avoided.) These alternatives were therefore not chosen.

### 4.2.3 General

A switch to short the load, and a switch to connect the input of the Improved Howland current source to ground instead of to the input voltage are installed to allow for increased safety.

The device is powered with bench top DC power supplies of 25 V, connected to form $\pm 50V$ supply rails, and a bench top function generator as the input voltage.

It is tested with different load resistors, as well as output current amplitudes at frequencies of interest. For this, the voltage drop over the load (i.e. rat or resistor) '$V_{rat}$', and the output voltage of the optocoupler current measurement circuit '$V_{opto}$' (which corresponds to the current through the load) are measured.

It is to be noted that the input voltage to the Improved Howland current source should be measured in order to verify the correct input voltage. The input of the Improved Howland current source is highly resistive, but many function generators with a 50 Ω source impedance assume a 50 Ω load impedance. The internal source voltage is thus internally set to be double of the desired voltage that was set by the user. A circuit diagram for this can be seen in figure 4.3. In the case of 50 Ω load resistance, everything works as expected and the voltage divider leads to $V_{out} = \frac{1}{2} \cdot V_{in}$. In the case of a load that is much bigger than 50 Ω, however, a load voltage of almost the entire source voltage drops over the load. Placing a 50 Ω resistor in parallel to the large load, will solve this problem, however, in a lossy way and only if the original load is not close to 50Ω.

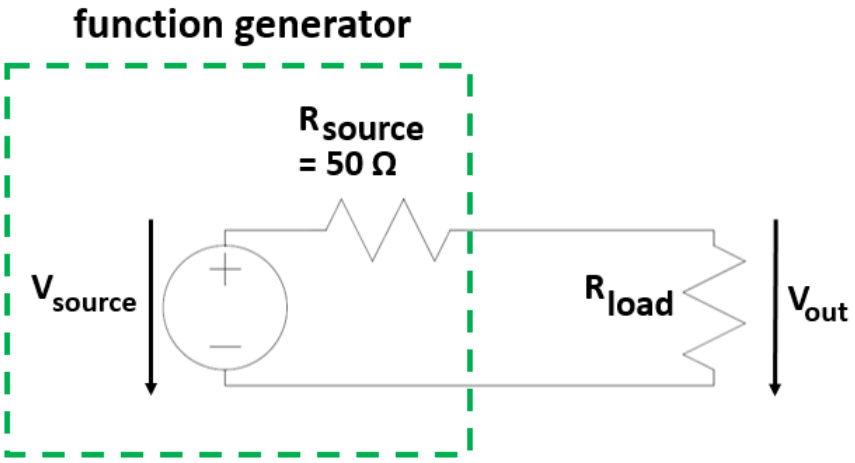


**Figure 4.3:** Circuit model of a function generator connected to a load impedance. The internal source impedance is 50 Ω, and often, a load impedance of 50 Ω is assumed by the function generator when internally setting $V_{source}$ to achieve the $V_{out}$ requested by the user.

## 4.3 *In vivo* Experimentation

All protocols were approved by the Animal Care and Use Committee, Johns Hopkins University.

### 4.3.1 Animal Preparation, Wounding and Plasmid Injection

IGS-Retired breeder rats are anesthetized with isofluorane. The area for the electrodes and wound on the dorsum is shaved using a commercial pet clipper. In one case, also part of the stratum corneum is removed using a BIC razor. The dorsum of the rats is wounded using a 8 mm diameter biopsy punch. Depending on the rat (see

| Rat Idx | injected plasmid | electrode size | average current [mA] | current type | current [mA] | duty cycle [%] | frequency [kHz] |
|---|---|---|---|---|---|---|---|
| a | 8385 | - | - | - | - | - | - |
| b | 8385 | 5 cm x 5 cm | 2 | DC | 2 | - | - |
| c | 8385 | 5 cm x 5 cm | 2 | AC (square) | + - 4 | 75 | 1.2 |
| d | 8385 | 5 cm x 5 cm | 2 | AC (square) | 2 + - 2 | 50 | 1.2 |
| e | 8385 | 5 cm x 5 cm | 4 | DC | 4 | - | - |
| f | 8385 | 5 cm x 5 cm | 4 | AC (square) | + - 8 | 75 | 5 |
| g | 8385 | 1 cm x 4 cm | 4 | DC | 4 | - | - |
| h | 8385 | 1 cm x 4 cm | 4 | AC (square) | + - 8 | 75 | 5 |

| Rat Idx | injected plasmid | electrode size | average current [mA] | current type | current [mA] | duty cycle [%] | frequency [kHz] |
|---|---|---|---|---|---|---|---|
| j | 8685 | - | - | - | - | - | - |
| k | 8685 | 5 cm x 5 cm; razor | 2 | DC | 2 | - | - |
| l | 8685 | 5 cm x 5 cm | 2 | DC | 2 | - | - |
| m | 8685 | 5 cm x 5 cm | 2 | AC (square) | + - 4 | 75 | 1.2 |
| n | 8685 | 5 cm x 5 cm | 2 | AC (square) | 2 + - 2 | 50 | 1.2 |

**Figure 4.4:** Experimental settings studied in different rats. Iontophoresis with average currents of 2 mA and 4 mA is investigated for two different luciferase plasmids. DC currents, as well as AC square wave currents with either a DC offset, or a dutycycle longer than 50 %, are studied. The AC frequency is experimentally determined by gradually increasing the frequency until muscle contraction is no longer visible in the rats. The effects of using a razor to remove the stratum corneum, and the effect of a decrease in electrode size, are further studied.

figure 4.4 for reference), the luciferase encoding plasmids NTC8385-VA1-Luc ('8385') or NTC8685-Luc ('8685') (Nature Technology Corporation; www.natx.com) are injected intradermally at 4 sites directly around the wound, as seen in figure 4.5. The volume injected per injection site is $50\mu l$ at a concentration of $1\frac{mg}{ml}$, thus corresponding to $50\mu g$. Animals are housed in single cages. After the procedures are finished, rats are given buprenorphine (0.1 mg/mL) for pain management.

### 4.3.2 Electrodes

Shortly after injecting the plasmid, the electrodes are placed on the shaved rat skin around the wound: TENS (transcutaneous electrical nerve stimulation) gel electrodes (5 cm x 5 cm; K.S. Choi Corporation, or Syrtenty) are either cut to be 1 cm x 4 cm with one of the 1 cm edges rounded, or left uncut. The smaller, cut electrodes are then fully covered in adhesive electrolyte gel (Tensive Conductive Adhesive Gel: Parker Laboratories, Inc.). The bigger, uncut electrodes are only covered in gel on one half, the half that will be facing the wound. The electrodes are then placed around the wound as shown by the schematics in figure 4.5 and the photograph in figure 4.7.

For the iontophoresis with 2 mA DC current, tape around the rat bodies is used to further secure the electrodes.

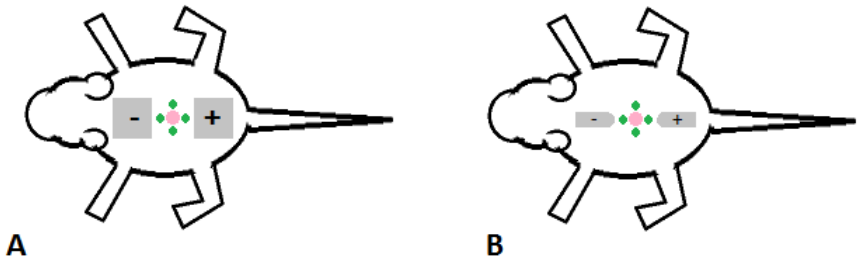


**Figure 4.5:** Schematic of rat setup: wound (pink), plasmid injections (green) and gel electrodes (grey): **A:** 5 cm x 5 cm electrodes; **B:** 1 cm x 4 cm electrodes with round edge.

### 4.3.3 Iontophoresis: Electrical Stimulation

Iontophoresis is administered between the two electrodes for 30 minutes. The current applied in each experiment is given in figure 4.4, where the AC current parameters refer to a square wave. Average currents of 2 mA and 4 mA are applied, with amplitudes of up to 8 mA in the case of AC square waves.

For direct current iontophoresis, a commercial iontophoresis current source is used (Chattanooga Ionto$^{TM}$, Patterson Medical). The equipment used in this case is shown in figure 4.6. The same equipment is used for the AC square wave stimulation, with the exception of the current source. In the AC case, the Improved Howland current source that is designed as part of this thesis is used instead.

#### 4.3.3.1 Electrical Measurement

In the DC case, the oscilloscope ground and signal probes are connected to the electrode leads to measure the voltage across the rats. The current delivered by the commercial current source is assumed to be correct, which has also been verified by

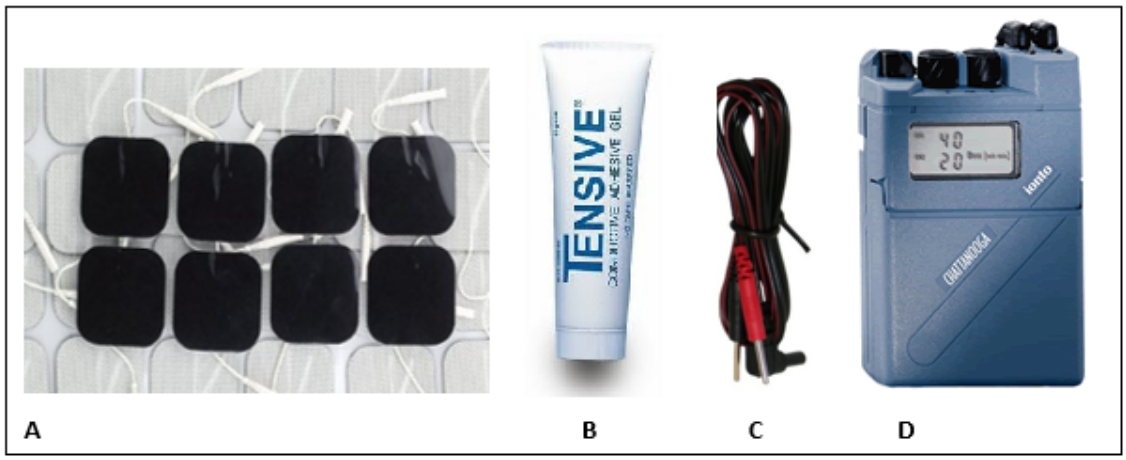


**Figure 4.6:** Equipment used for iontophoresis. **A:** Electrodes before being cut into shape; **B:** Adhesive electrolyte gel; **C:** Electrode leads connecting the electrodes to the leads of the current generator; **D:** Chattanooga Ionto (commercial DC current source for iontophoresis) - used here only for DC iontophoresis.

voltage measurement across defined resistors beforehand. In the AC case, thus when using the circuit designed as part of this thesis, the oscilloscope signal probes are connected to the measurement points indicated by $V_{rat}$ and $V_{opto}$ in figure 4.2 and 4.1. The oscilloscope ground connectors are connected to the ground of the circuit. Oscilloscope voltage readings are recorded using a Laptop and respective interface program to the oscilloscope (Keysight BenchVue, Keysight Technologies).

For the DC experiments, the voltage across the rats is recorded in continuous intervals with small breaks (required for saving data in between recordings). For the AC experiments, the voltage waveform $V_{rat}$ across the rat and the voltage waveforms $V_{opto}$ corresponding to the current through the rat are recorded every 5 minutes.

#### 4.3.3.2 Thermal Imaging

Relative thermal images (the absolute temperature is not recorded) of the shaved rat dorsum are taken before the placement of the electrodes, after the placement of the electrodes, and in regular intervals (every 5 minutes) during the iontophoresis application. This is done using an infrared camera (Seek Thermal) connected to an Android phone, which is securely placed on a stand at a fixed position. This can be seen in figure 4.7.

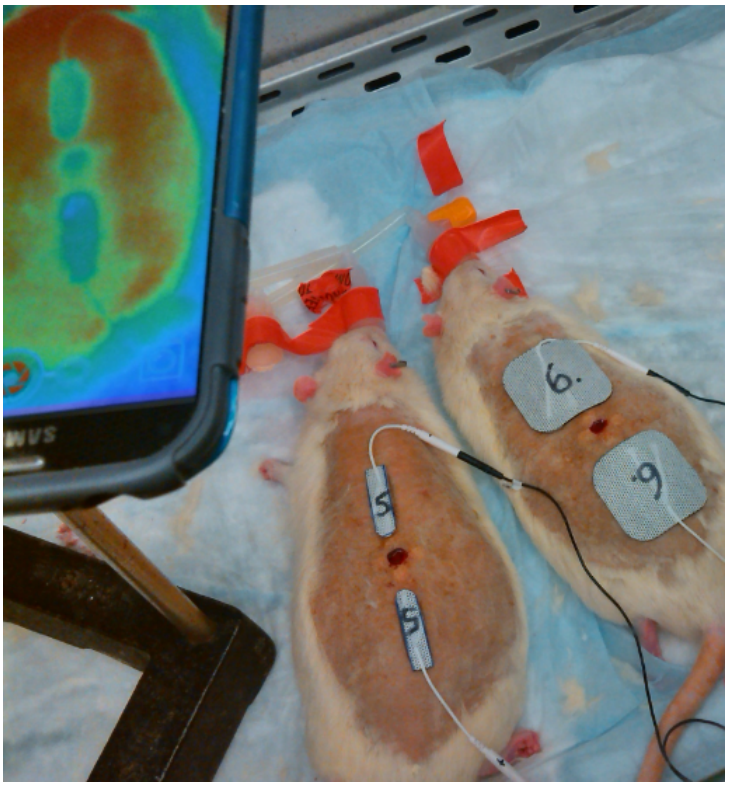


**Figure 4.7:** Experimental setup, including thermal imaging, using 1 cm x 4 cm, as well as 5 cm x 5 cm gel electrodes, for the 4 mA DC current experiments.

### 4.3.4 Luciferase Imaging and Processing

*In vivo* luciferase activity is assessed on day 1, 2 and 3 after transfection (day 0 is when plasmid injection and iontophoresis are performed). For this, the animals are sedated with isofluorane. They are injected intraperitoneally with a solution of luciferin in saline ($5ml$ of $15\frac{mg}{ml}$ solution of luciferin in saline). A conventional light photograph is taken and bioluminescent images are aquired 30 minutes after luciferin injection using a Xenogen Camera (IVIS, Xenogen, Alameda, CA). The camera is calibrated using a bioluminescent phantom. The bioluminescent images are overlaid onto the conventional image of each animal, and the light emission, corrected for background luminescence, is calculated for each injection site using image analysis software (Living Image, Xenogen, Alameda, CA). Maximal light emission per injection spot, as well as the light emission average per injection spot is determined. For each rat, the average of all four injection spots is calculated for these determined measures.

# Chapter 5

# Results and Conclusion

## 5.1 Simulation

The simulations of the designed circuit achieved results similar to the measured ones shown further below (but with no noise).

### 5.1.1 Current Density in Tissue

A plot of the simulated current density can be found in figure 5.1. Both electrode types show the following pattern: It can be seen that the highest current density occurs around the edges facing the respective other electrode of opposite polarity, thus facing the wound. This effect occurs especially in the case of the highly resistive stratum corneum, and gradually decreases for lower tissue layers. In the epidermis, the current density is generally higher than in other layers, and especially the area to

the left and right of the wound shows high current density. However, there seems to be an area between the electrodes and the wound that is shielded from the current flow. The dermis current density has a similar pattern as in the epidermis - they both have the same conductivity in the model, but the current density at the electrode borders is lower in the dermis since it is further away from the electrodes and the current thus less concentrated at this point. Almost no current reaches the subcutaneous tissue. In all layers, there seems to be hardly any current flow directly underneath the electrodes.

The smaller and more narrow, as well as partially rounded, electrode type leads to a better concentration of the current around the wound, and also to higher maximal current density values (not shown here). This is as expected, since a smaller area in the electrode-tissue interface for the same current passing, leads to a higher current density in this area.

## 5.2 Bench Top Experimentation

The designed Improved Howland current source reliably delivers square wave currents of frequencies up to 10 kHz (higher frequencies were not tested) to resistors of up to $20k\Omega$ (higher values were not tested). As with every current source, this only holds true when the set output current leads to a load voltage over the load that lies in the compliance voltage range of the circuit. The correct current delivery is

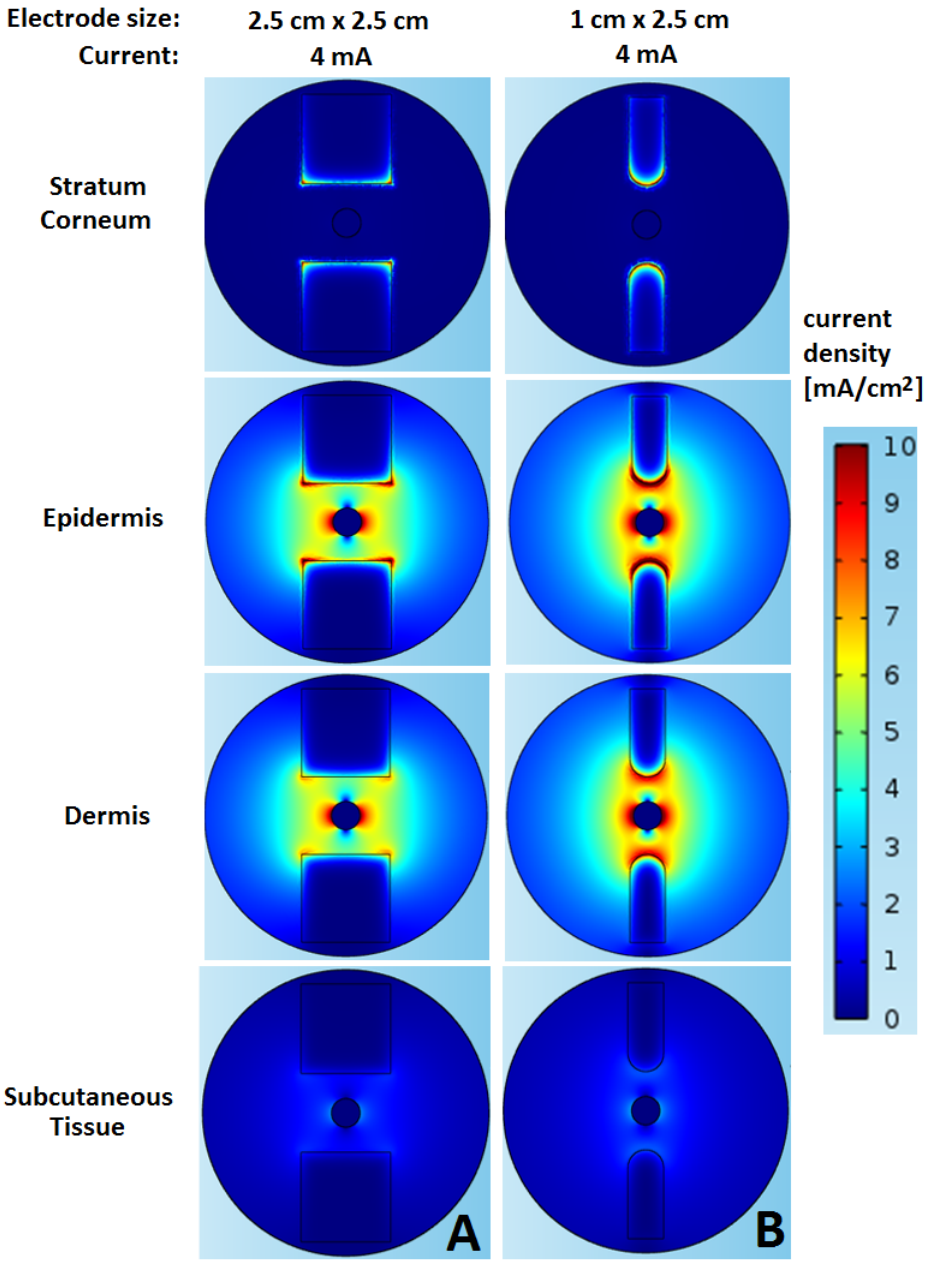


**Figure 5.1:** COMSOL simulations of current density in skin for electrodes of similar shapes (but slightly smaller) compared to those used *in vivo*. The plots show the current density along horizontal cuts placed at the middle of the respective skin layers for a 4 mA current. The small circle in the center of each plot is the wound. The electrodes are the square (**A**) and smaller long electrodes (**B**) seen below and above the wound. The colorbar was limited to 10 $\frac{mA}{cm^2}$ to allow for better visalization of lower current densities. Values higher than this limit are shown as the color of 10 $\frac{mA}{cm^2}$.

determined from the voltage drop measured across the resistors and Ohms law. The measured output voltage corresponding to the load current was independent of the load resistance and reliably gave the same output for the same current, also in the case of varying load resistance. Measurements with high oscilloscope resolution and thus very little ground noise were performed when verifying the functioning of the circuit. In order to match *in vivo* measurements, a lower oscilloscope resolution with more ground noise is chosen for the bench top measurements shown here. They can be seen in the figures 5.2, 5.3 and 5.4.

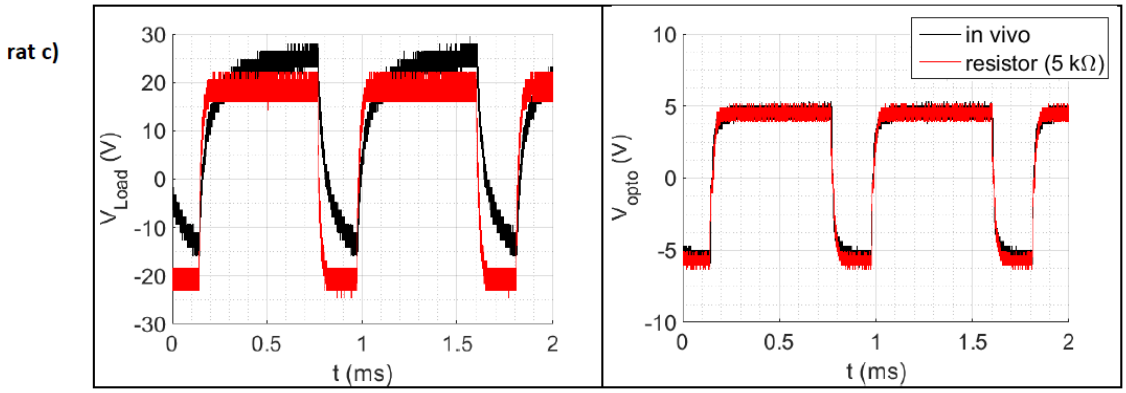


**Figure 5.2:** Voltage over load and voltage at output of optocoupler current measurement circuit (refer to figure 4.1 for circuit model). Comparison of measurements for rat (label c) and for a 5 $k\Omega$ resistor as load.

rat d)

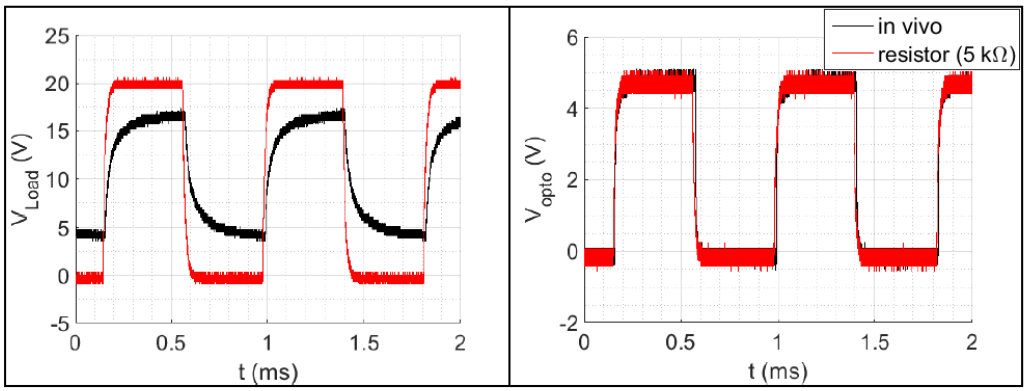


**Figure 5.3:** Voltage over load and voltage at output of optocoupler current measurement circuit (refer to figure 4.1 for circuit model). Comparison of measurements for rat (label d) and for a 5 $k\Omega$ resistor as load.

rat f)

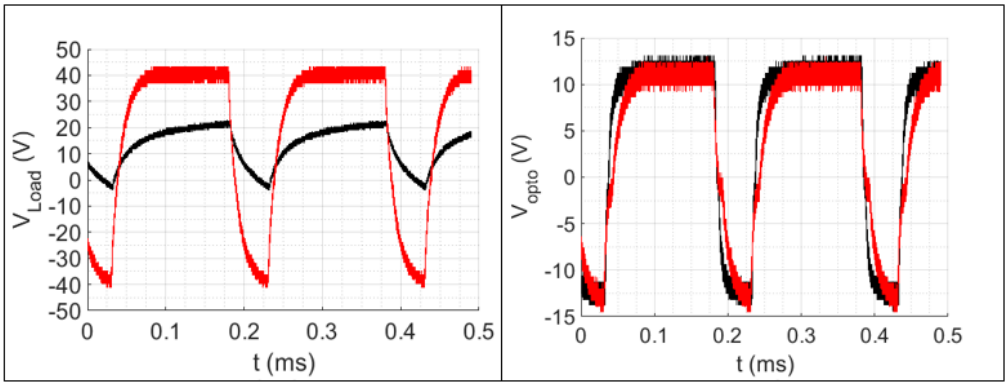


**Figure 5.4:** Voltage over load and voltage at output of optocoupler current measurement circuit (refer to figure 4.1 for circuit model). Comparison of measurements for rat (label f) and for a 5 $k\Omega$ resistor as load.

## 5.3 *In vivo* Experimentation

### 5.3.1 Electrical Measurement

In order to allow for good simultaneous monitoring of all waveforms during the experiment, the resolution of the oscilloscope was not set to its maximum. This led to lower resolution measurements, which introduced higher ground noise. The noise of the measured current is consistent across measurements in the bench top and *in vivo* setting for the same resolution settings, which indicates that the same and thus correct current is flowing through the rats. This can be seen in figures 5.2, 5.3 and 5.4, where a comparison of the experimental bench top and *in vivo* measurements is shown for the different stimulation waveforms used *in vivo*.

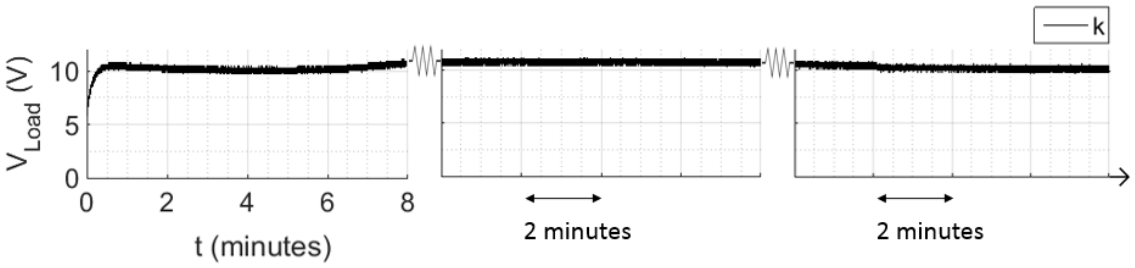


**Figure 5.5:** Voltage over rat (label k, razor was used here) with 2 mA DC current stimulation via 5 cm x 5 cm electrodes stays relatively constant over time of 30 min iontophoresis after current has ramped up to specified value.

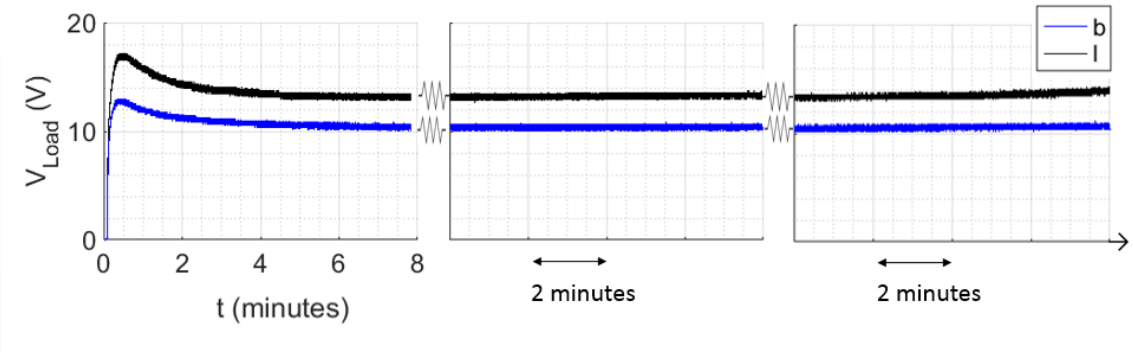


**Figure 5.6:** Voltage over rats (labels b and l) with 2 mA DC current stimulation via 5 cm x 5 cm electrodes stays relatively constant over time of 30 min iontophoresis after current has ramped up to specified value.

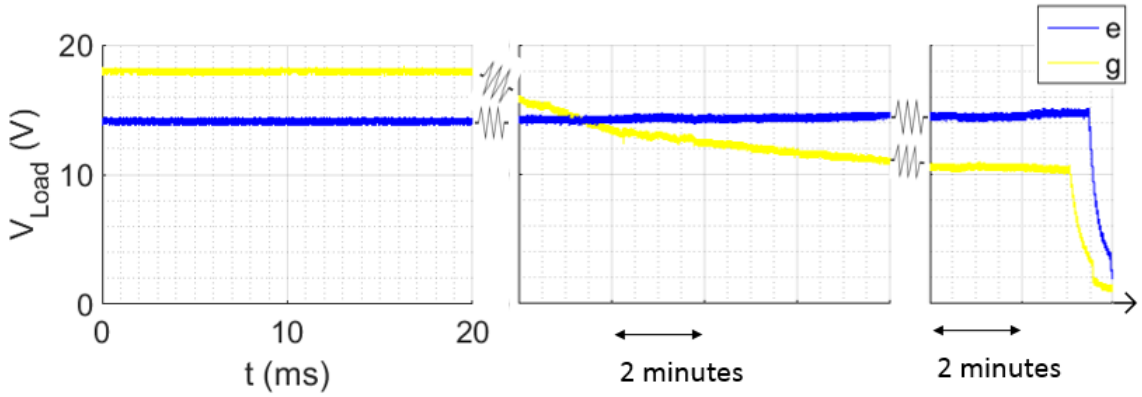


**Figure 5.7:** Voltage over rats with 4 mA DC current stimulation. The voltage shown during the first 20 milliseconds stayed at this value for around 8 minutes prior to the begin of this plot (not shown). Voltage stays relatively constant over time of 30 min iontophoresis when current is applied via 5 cm x 5 cm electrodes (label e). In contrast, voltage starts to drop significantly after some time when applied via 1 cm x 4 cm electrodes (label g).

### 5.3.2 Thermal Imaging

The thermal images aquired can be seen in figure 5.8. They show a cooler wound and fur of the rats, while the skin is warm. This is due to the cooling of the wet wound, and the insulation function of the fur which doesn't let body warmth out. Electrode placement leads to cooling around the electrodes with the electrodes being cool themselves. The locations of additional adhesive gel (the half of each electrode facing the wound) are especially cool indicating the cooling function of the gel. Current stimulation increases the temperatures again: It decreases the electrodes' cooling effect, and seems to bring the affected skin back to normal skin temperature. The parts of the electrodes with the gel (that are in contact to the skin and thus conduct the current) heat up especially. After taking the electrodes off, the remaining gel appears cool. It can further be seen, that the temperature at the top of the rat appears to be higher, which could be due to influences of the camera angel on the measurement. Although the camera was kept at a fixed position, the rats had to be taken off the isofluorane during the experiments to keep breathing normal, which made simple numerical subtraction of these images for difference detection less suitable. A precise path of current flow is thus hard to deduce and probably would require higher amplitude or longer duration of current flow. Another even bigger problem is the fact that the thermo-camera Seek Thermal does not provide a temperature scale along with its pictures, making the determination of absolute temperatures almost impossible. Further, it seems that the colors are mapped to the range of recorded temperatures at

each time point individually, thus, the temperature corresponding to a certain color depends on the range of all present temperatures at a given time point and is thus not constant over time. Seek Thermal does, however, provide a threshold setting where only temperatures above a custom set temperature threshold are shown. While this would allow for a first step towards better determination of absolute temperatures, it is still insufficient for our purposes. Ideally, a thermal camera with a custom set temperature range that is constant over time, and with a corresponding colorbar or scale that can be seen would be used in the future.

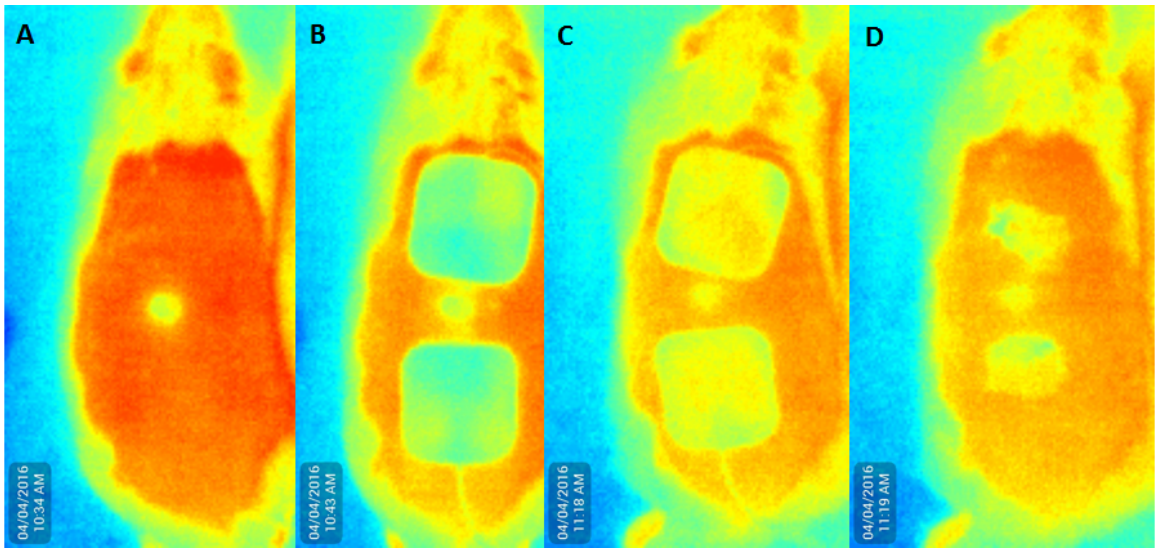


**Figure 5.8:** Thermal Images for AC experiment with ±4mA at 75% duty cycle at 1.2 kHz (average current of 2 mA): Red is warmest, then orange, yellow, green, light blue, and the coldest is dark blue. The camera used does not provide a colorscale, and maps the colors to the range of temperatures seen at each given time point.
**A:** before electrodes are placed;
**B:** after electrodes are placed but before iontophoresis;
**C:** at the end of / right after iontophoresis
**D:** after electrodes are removed (adhesive gel partially remains stuck on skin).

### 5.3.3 Electrochemistry

Electrodes after various experiments can be seen in figure 5.9. Bubble formation can be seen as the result of electrochemical reactions. A 4mA average current leads to more gas formation than a 2 mA average current, thus showing more bubbles on the electrodes. Smaller electrodes in the case of 4 mA DC have especially high and dense bubble formation. This makes sense, since a higher current density crossing the electrode-tissue interface, requires more electrochemical reactions to transfer the charge and accordingly more by-products, such as gas. These reactions should be kept in mind, since such reactions can modify electrodes and accordingly their current injection, or the voltage drop across them (which influences the load impedance seen by the Improved Howland current source).

### 5.3.4 Undesired Biological Effects

A small burn could be observed directly after the DC 4mA application with the small 1 cm x 4 cm electrodes.

7 minutes after the experiment with 2mA +-2mA, one rat was stiff (including the tail), but the breathing and heartbeat were normal. It loosened up after some time. The other rat which received the same stimulation was not stiff at that time.

Rats seized up (body moved up from table, especially the back was rounded) during AC current stimulation with low frequencies at high current values. The initial

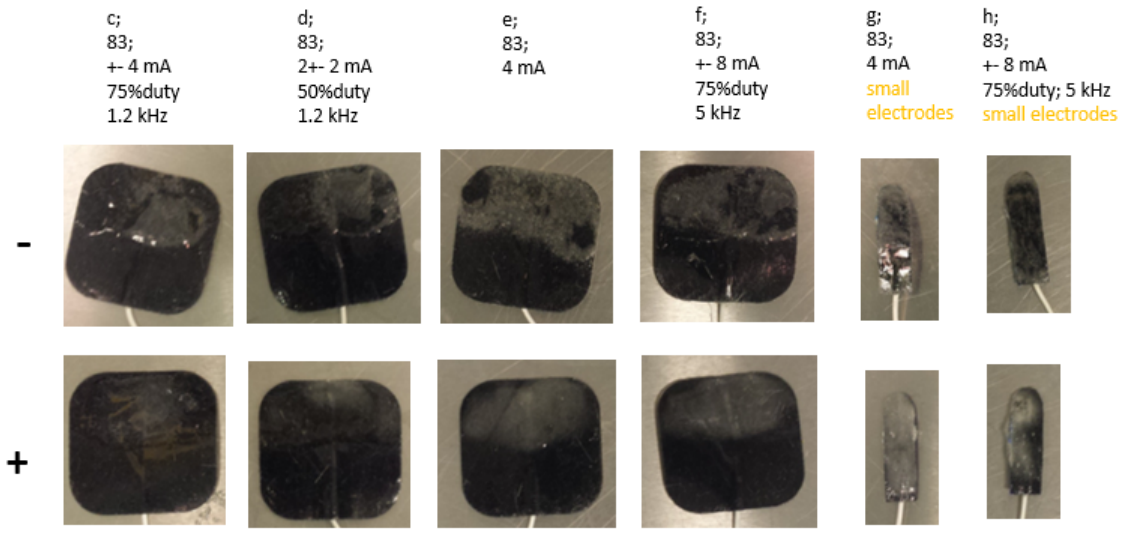


**Figure 5.9:** Electrodes from different rats after iontophoresis application through them. The top row is the negative electrode, the bottom electrode the positive one. Only the top half of each square electrode was covered in electrolyte gel before applying it to the rat skin. It can be seen that the bubbles occured only there, thus current probably mainly went through that part of the electrode. The big black spots on the negative electrodes are giant bubbles from which gas has leaked, thus allowing for re-attachement of the detached gel to the carbon film of the electrode. Negative electrodes have stronger bubble- and thus gas formation. 4 mA average leads to more gas formation than 2 mA average current. Smaller electrode in case of 4 mA DC has especially high and dense bubble formation.

plan had been to use 30 Hz instead of 1.2 kHz, but the rats seized up at the desired current amplitude and waveform for this value. The frequency had to be increased. 1.2 kHz was the lowest frequency for this amplitude where the rats did not seize up. The same occured for the the +-8mA stimulation. At low frequencies, the muscles of the rats contracted and the rats seized up, even at lower current amplitudes (when gradually increasing it at the beginning of an experiment). This effect decreased at higher frequencies with the current amplitude threshold for seizing up increasing. The current amplitude of 8mA lead to seizing up of the rats at lower frequencies, but this effect could no longer be observed at higher frequencies of 5 kHz and above (no muscle contraction was visible). There was no difference observed in the seizing up of the rat with the small electrodes and the big electrodes at any given frequency or amplitude.

### 5.3.5 Luciferase Expression

The luciferase expression on different days can be seen in figure 5.10 for plasmid 8385, and in figure 5.11 for plasmid 8685. Figure 5.17, 5.18, 5.19 and 5.20 show the average of either the average luminescence count per injection site, or of the maximum luminescence count per injection site.

It makes sense to compare within plasmids, since the control is different for both: For the plasmid 8685, the control seems to work better than iontophoresis, while the opposite is the case for the plasmid 8385. When analyzing the importance of these

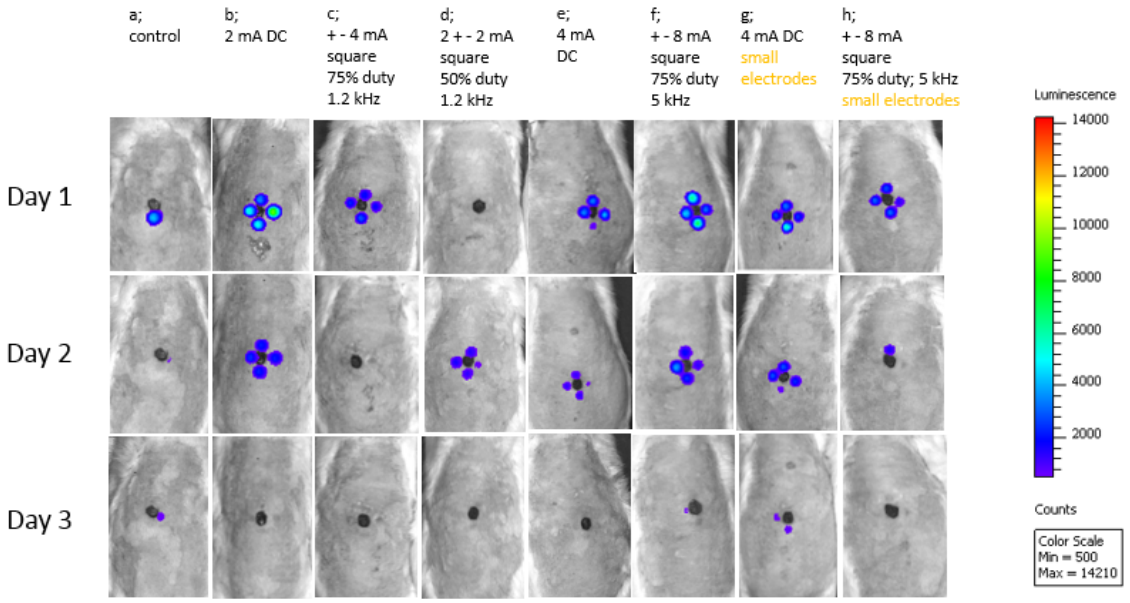


**Figure 5.10:** Plasmid 8385: Luciferase expression on Day 1, 2 and 3 for different stimulation setups, for bioluminescence counts above 500. The control rat a, which didn't receive any iontophoresis treatment, had transfection in one injection spot only, and very little transfection remaining on day 2 and 3. Rat b and f exhibited the best transfection: all four injection spots were transfected with high levels on day 1, and slightly lower levels on day 2 (some transfection on day 3 for rat f, but not for rat b). Rat c and h had very little transfection on day 2, while rat d had little transfection on day 1 but a transfection similar to many other rats on day 2. It is thus a late transfection. Rat a (control), f and g are the only ones that had some low transfection left on day 3.

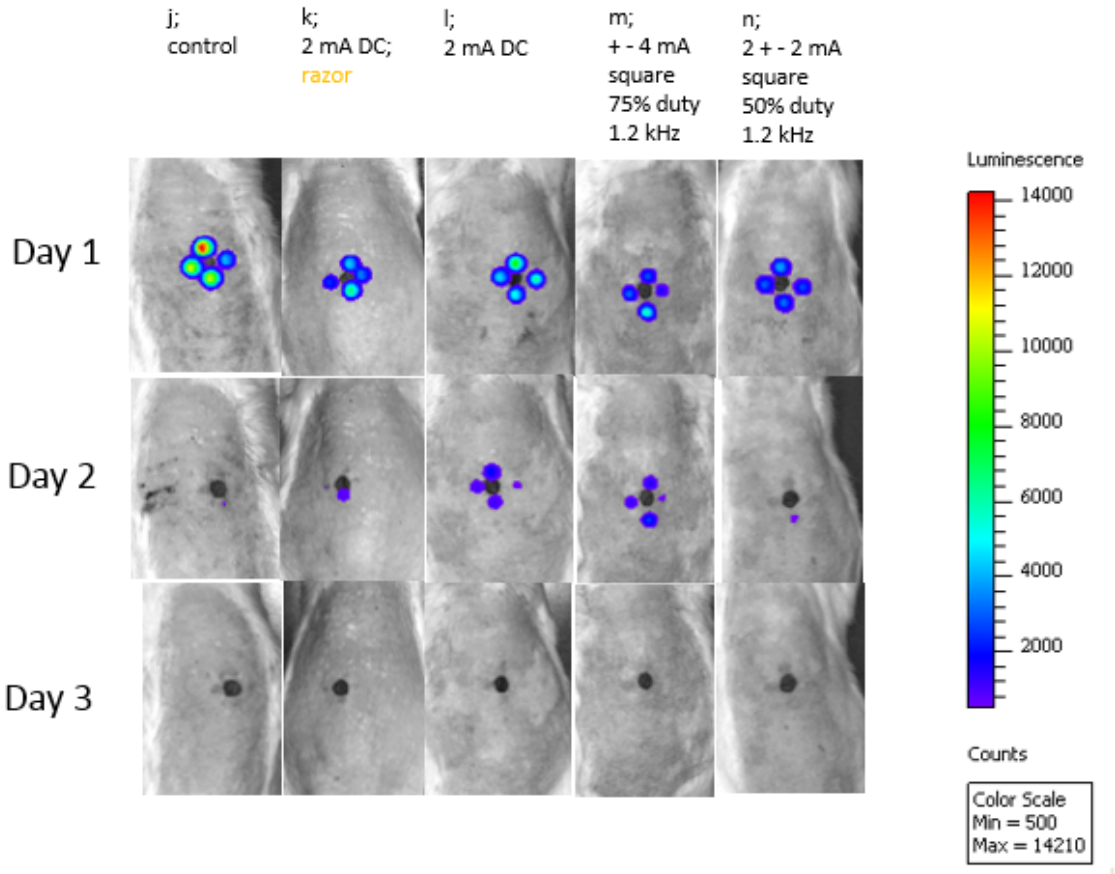


**Figure 5.11:** Plasmid 8685: Luciferase expression on Day 1,2 and 3 for different stimulation setups. Control rat (j) which didn't receive iontophoresis treatment had the highest transfection on day 1 (red spot). All other rats also had transfection in all four injection spots on day one. When iontophoresis was applied, more transfection remained on day 2 than in the case of the control on day 2. None of the rats showed transfection on day 3. Rat l with the 2 mA DC current stimulation showed the best transfection since it achieved high luminescence counts on day 1, and still had transfection in all four spots on day 2. Rat m is similar regarding this, but had lower values on day 1.

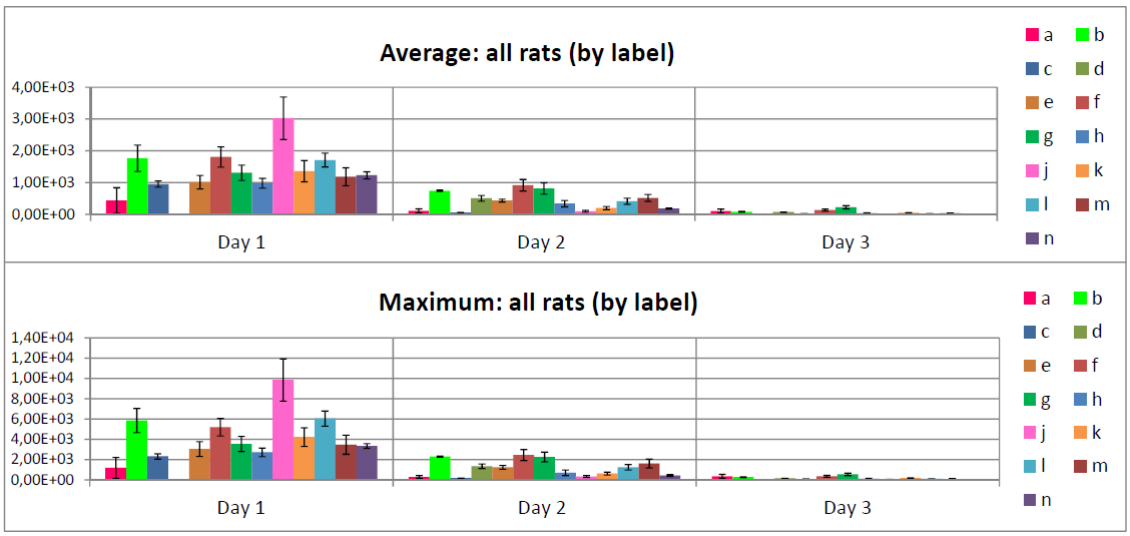


**Figure 5.12:** Average over four injection sites for each rat regarding average and maximum bioluminescence count per injection. Standard error over the four injections sites per rat is shown by error bars. a and j are control of plasmid 8385 and 8685 respectively. Refer to figure 4.4 for further label explanation.

results, it should be taken into account that only one animal was used per tested parameter setup, and that usually great variability occurs from animal to animal. Further studies are thus needed to verify these results.

#### 5.3.5.0.1 Plasmid 8385:

For plasmid 8385, it can be seen that all iontophoresis parameters except for 2+-2 mA square wave stimulation led to higher transfection (compared to the control) on day 1 regarding the average count, and the maximum count. A similar pattern can be seen on day two, where all iontophoresis parameters show higher transfection than the control, except for the case of the +-4 mA square wave, which has a lower average and maximum count.

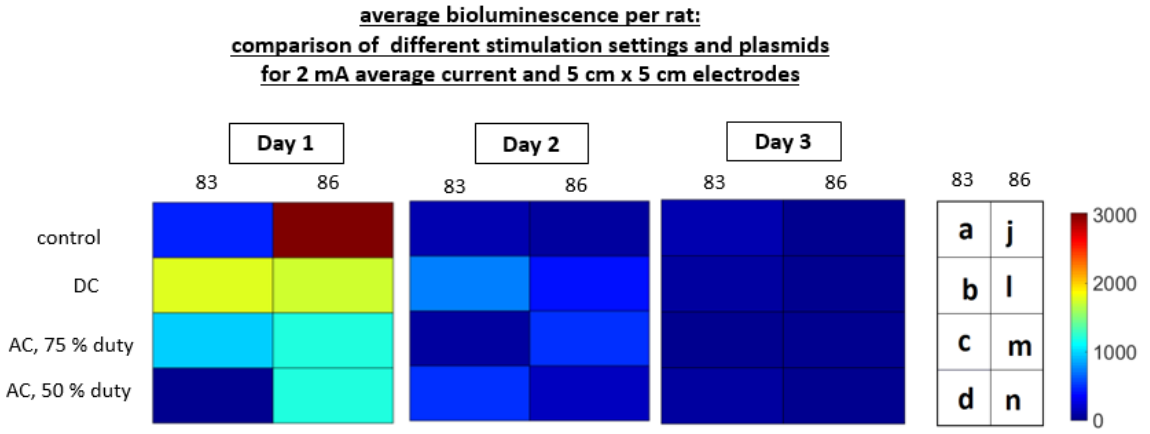


**Figure 5.13:** Average bioluminescence per rat: Comparison of different stimulation settings and plasmids for 2 mA average current and 5 cm x 5 cm electrodes. No razor used. 83 refers to plasmid 8385, 86 refers to plasmid 8685. Corresponding labels of rats (see figure 4.4 for details) and colorbar shown on right. The control rat for plasmid 8685 yielded the highest average bioluminscence value on day 1, but has low values on day 2 and 3. 2 mA DC iontophoresis stimulation was the stimulation that achieved the highest bioluminescence for both plasmids, with comparable values for both plasmids on day 1. For plasmid 8385 the control had low bioluminescence, however, the AC stimulation with 50% duty cycle had even lower bioluminescen on day 1. DC stimulation achieved the best results (highest average luminescence) on all days for plasmid 8385.

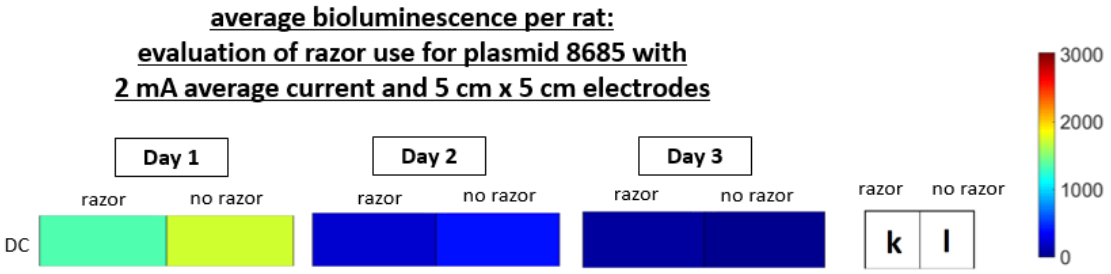


**Figure 5.14:** Average bioluminescence per rat: evaluation of razor use for plasmid 8685 with 2 mA average current and 5 cm x5 cm electrodes. The razor was used to remove part of the stratum corneum. Corresponding labels of rats (see figure 4.4 for details) and colorbar shown on right. On day 1 and 2, not using a razor yielded higher bioluminscence average values than using a razor. Using a razor to remove part of the stratum corneum did not improve transfection, which could be due to the fact that the plasmids were injected instead of applied topically and thus didn't need to pass the stratum corneum anymore to transfect the cells.

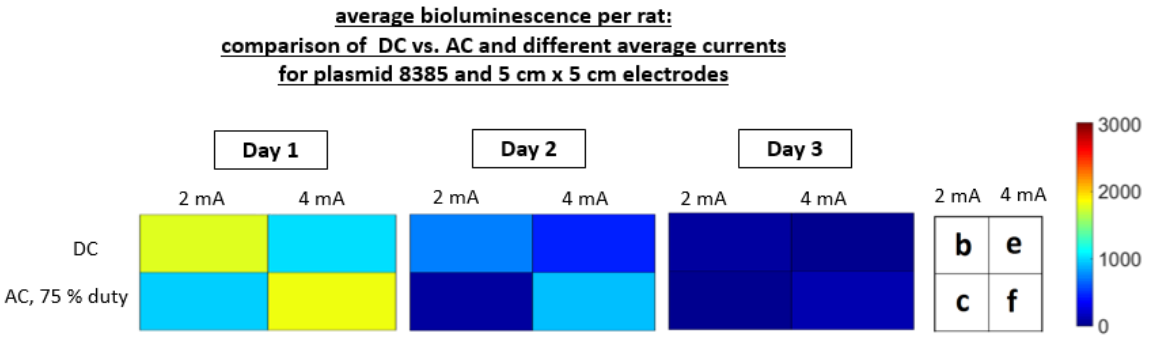


**Figure 5.15:** Average bioluminescence per rat: comparison of DC vs. AC stimulation, as well as different average currents for plasmid 8385 and 5 cm x 5 cm electrodes. Corresponding labels of rats (see figure 4.4 for details) and colorbar shown on right.

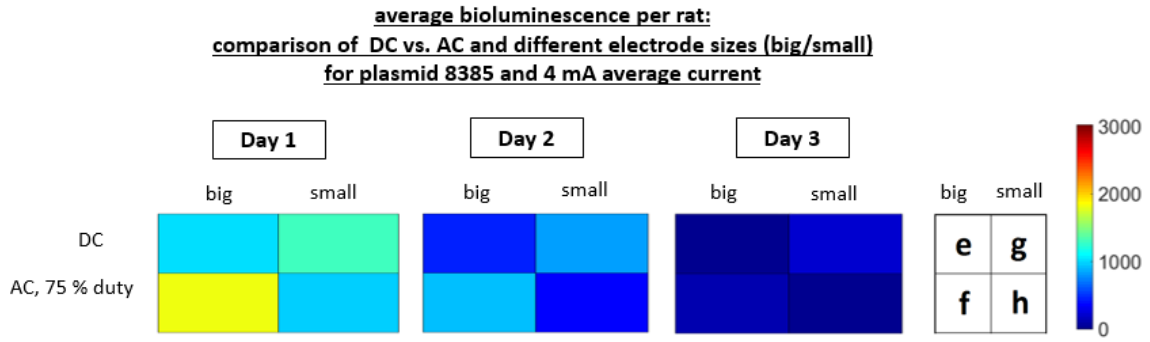


**Figure 5.16:** Average bioluminescence per rat: comparison of DC vs. AC for different electrode sizes (big electrodes of 5 cm x 5 cm / small electrodes of 4 cm x 1 cm) for plasmid 8385 and 4 mA average current. Corresponding labels of rats (see figure 4.4 for details) and colorbar shown on right.

The smaller electrodes increased the transfection for the case of DC stimulation, but decreased it for the case of square wave stimulation (for both maximum and average).

Comparing the square wave stimulation with +-4 mA to that of +-8 mA for plasmid 8385, it can be seen that the maximum count and average count are increased for the higher amplitude.

Comparing the DC stimulation with 2 mA to the DC stimulation of 4 mA, it can be seen that the 2 mA DC stimulation achieved higher transfection.

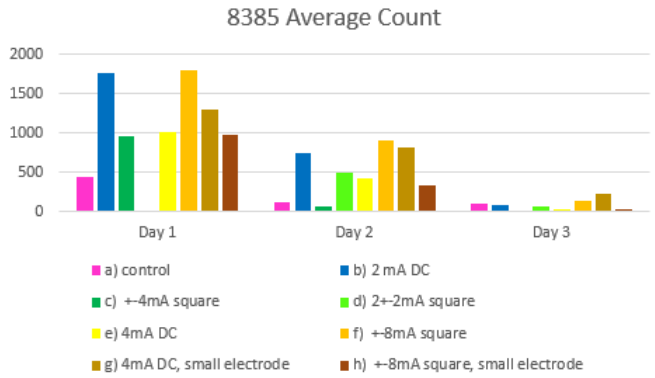


**Figure 5.17:** Plasmid 8385: Average bioluminescence count over 4 regions of interests (injection sites) per rat.

#### 5.3.5.0.2 Plasmid 8685:

It can be seen, that the control for plasmid 8685 lead to a much higher luminescence count than iontophoresis application did, thus more transfection was achieved without iontophoresis than with iontophoresis.

A higher transfection average and maximum was achieved without the razor com-

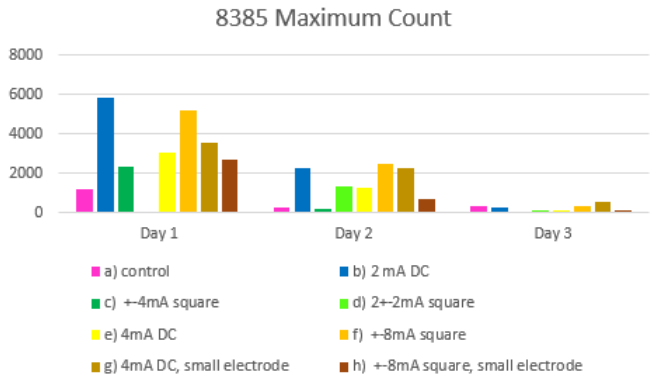


**Figure 5.18:** Plasmid 8385: Average of bioluminescence count maxima in each injection site per rat.

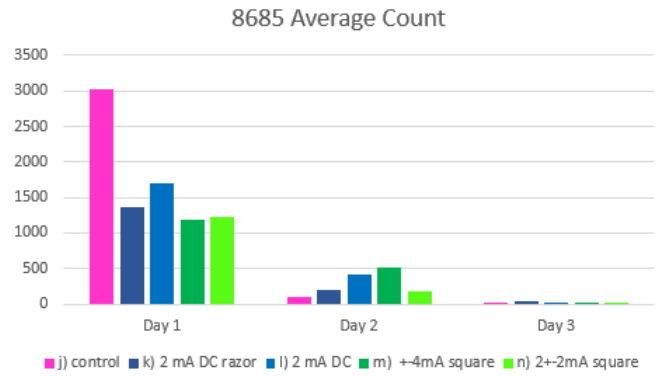


**Figure 5.19:** Plasmid 8685: Average bioluminescence count over 4 regions of interests (injection sites) per rat.

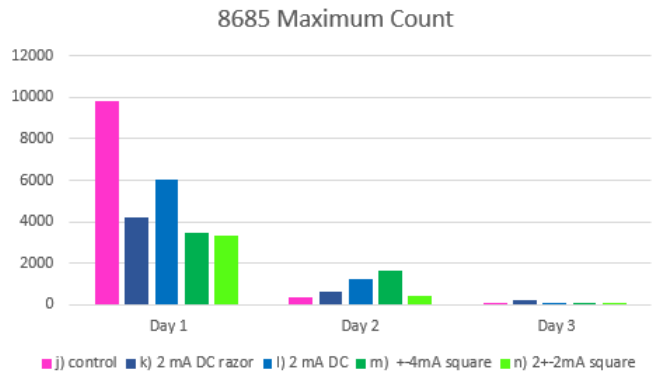


**Figure 5.20:** Plasmid 8685: Average of bioluminescence count maxima in each injection site per rat.

pared to using the razor. This might be due to the fact that the plasmid was injected intradermally, and the stratum corneum does thus not pose a physical barrier to the entry of the plasmid to the skin.

## 5.4 Conclusion

Various current density simulations predict a high current density around the wound for the used electrode setup.

The Improved Howland current source works as expected, both in bench top experimentation and *in vivo*.

The voltage drop across the rats for the defined AC currents seems to indicate the charging of a capacitor which does not get completely discharged at the applied frequency. This is probably based on the fact that a positive average current is applied.

The constant current DC iontophoresis is applied at a constant voltage in the case of big electrodes, but the voltage across the rat starts to decrease after some time for a 4 mA current applied through small electrodes. This could be due to tissue permeabilization or electrode impedance changes occuring at high current densities.

Temperature measurements seem to be useful for determining current flow, but the cooling effect of electrolyte gel and gel electrodes, as well as the cooler open wound before iontophoresis, make an analysis hard. Thermo cameras with a fixed

temperature range and colorbar should be used. Necessary movement of animals for regulation of isofluorane application poses additional challenges for digital subtraction of images to determine current flow.

Iontophoresis seems to enhance transfection of the plasmid 8385. In the case of plasmid 8685, the transfection in the control is much better than in the case of iontophoresis. Only one rat was used per setting, thus further research must be done to verify these preliminary findings.

In order to be portable and easy to use as well as more safe to use, the iontophoresis circuit should be battery powered in the future. Although mechanical switches were put in place to allow for higher safety, additional safety measures such as fuses and decoupling mechanisms (e.g. transformers or optical connections to any devices that are connected to the power net), etc. should be put in place.

# III

# Neural Stimulation Implant Power Link Design

# Chapter 6

# Introduction

## 6.1 Motivation

The function of the human brain is not yet fully understood. Before the time of neural implants, injury or resection of parts of a patient's brain gave insight to what the original functions of these areas might have been. With the advancement of modern technology, the field of neural technology has also moved forward, allowing for an increased understanding of the brain, as well as for a more effective therapy in the case of disease. Stimulating a diseased brain in a certain way could make this brain function like a healthy brain. Devices for stimulation are thus of special interest. A great example of this is deep brain stimulation for the suppression of tremor in Parkinson's Disease.[53] Other diseases that could benefit from such targeted stimulation are epilepsy,[54] brain tumors, anxiety disorders,[55] schizophrenia or depression.[56]

The brain is known to function by its multiple parts working together. Activating the brain in natural activation patterns thus requires targeted stimulation[57] at distributed locations all over the brain while causing minimal tissue damage. Most existing technology is either not covering large areas of the brain, not targeting individual or few neurons, or causes significant tissue damage. A wirelessly powered sub-millimeter implant for neural stimulation, which can be distributed in swarms all over and deep into the brain, does not exist so far, but would address these issues. We propose such an implant and call it the micro-bead: The final goal is an implant with an outer dimension of 100 $\mu m$ in each direction. Its flexibility in placement allows for many different and new applications. The distributed micro-beads can be individually addressed and synchronized to study the interactions between different areas of the brain. The small size of the implant allows it to easily fit between neurons without destroying much tissue. The power is provided through an inductively coupled link which is the focus of this work. It was of interest to see what the inductor designs possible in the available 0.18 um CMOS process could offer for such a power link.

## 6.2 Prior Art

An increasing number of publications on fully implantable neural interface chips below $1mm^2$ show the trend towards miniaturization and interest in this field. Most of these implants, however, record neural signals without having the ability to stim-

ulate neurons. Neural dust is a proposed wireless sub-millimeter implant for neural recording which is powered using ultrasound and which, like our proposed system, is supposed to be implanted in swarms[58][59] . For neural implants with submillimeter secondary inductors, the focus is often on individually implanted chips, not swarms of chips, and communication distances of 1 mm are achieved[60].[61] Neural recording implants with outer diameters of 1 mm also exist.[62] Wireless links with inductors of this size have further been characterized *in vivo* for neural applications,[63] and design methodologies for such links have been described[13][64].[65]

While not specifically made for biomedical applications, the so called $\mu$ chip for RFID applications by Hitachi has a 400 um x 400 um inductor as the internal antenna.[66] The follow up of this chip is the powder chip[67] with the same antenna size and a communication distance of up to 1.2 mm.[68]

Various authors consider submillimeter sized implants, suggesting that a passive approach which directly converts received power into a stimulating current should be considered regarding floating wireless microstimulators for neural prosthetics,[7] or that a radiofrequency (RF) powered 100 um x 100 um electromagnetically powered chip for implantation in biological tissue 'seems feasible with current technology'.[69]

A large number of sub-millimeter inductor designs is studied in the literature,[70][71][72][73][74][75][76] however, without being analyzed with regards to inductive power transfer to them.

State of the art wireless neural stimulation devices occupy larger areas such as 4.6 x 5.4 $mm^2$[77] , 4 $mm^2$[78] , or 2.25 $mm^2$[79] and include button-sized wireless microstim-

ulating 3-D arrays with areas of 4.6 mm x 4.6 mm,[8081] that are to be spread all over the brain.

# Chapter 7

# Background

## 7.1 Electrical Stimulation of the Nervous System

Electrical stimulation of the nervous system creates a functional response, such as an action potential by membrane depolarization of neurons. When an ionic current flows between electrodes and passes neural tissue, one can speak of current or charge being injected into that tissue. The influence of this injected current on the membrane potential can be seen in the Hodgkin Huxley equations (equation 7.1). C is the membrane capacitance, V is the membrane potential, $I_{injected}$ is the current that is injected into the neuron, and $I_{ionic}$ is the voltage dependent ion-channel current through the membrane.

$$C \cdot \frac{dV}{dt} = I_{injected} - I_{ionic} \tag{7.1}$$

Stimulating neurons directly can be achieved by currents as low as $2\mu A$, which is less than $\frac{1}{100}$ of the current needed with surface stimulation,[82] thus the location of charge injection is of great importance. The current waveforms required for neural stimulation greatly depend on the application and size of the electrodes, and often have amplitudes between of $1\mu A$ and $10mA$.

When a neuron spikes an action potential, this information gets carried on to other neurons. This can increase or decrease the membrane potential of the receiving neurons, depending on whether the spiking neuron is excitatory or inhibitory. Excitatory neurons are responsible for carrying information across brain regions, and inhibitory neurons can control and impede the activation of excitatory neurons. Thus, depending on which type neuron is stimulated, both excitatory or inhibitory functions can be triggered with stimulation. Using this for the control of brain function, however, remains a challenge due to the interconnectedness and complexity of the brain.

There are two mechanisms that allow for the transition of electrons flowing in the stimulation electrode, to ions flowing in the neural tissue: The faradaic stimulation involves electrochemical reactions of surface-confined chemical species which are oxidized or reduced at the electrode-tissue interface. These reactions provide high charge levels, but can become irreversible and lead to electrode or tissue damage, depending on the stimulation waveforms and changes in electrolyte composition occurring at

the interface. Capacitive stimulation involves charging and discharging the electrode-electrolyte double layer at the electrode-tissue interface. It has the advantage that a stimulation pulse does not create or consume substances which could be toxic or change the pH of the tissue.[83]

In this regard, the electrode material used is of special interest. Typical materials for safe reversible charge injection to the nervous system are iridium oxide, platinum and titanium nitride.[83] Iridium oxide is often used as a faradaic electrode coating to increase charge injection capacities, requires a positive bias for such high charge injection (it has the highest charge injection capacity of these three materials with up to $5mC/cm^2$) and can be damaged by too negative potentials or oxide delamination. Platinum is a noble metal, and although electron transfer occurs across the tissue-electrode interface (thus, a faradaic reaction) the reactions occuring are described as pseudocapacitive. This is due to the fact that the faradaic reactions are restricted to a monolayer on the surface and because double-layer charging occurs. Platinum has the lowest charge injection capacity of the three mentioned electrode materials. The reaction for titanium nitride is the capacitive double layer charging, which occurs at the porous coating. In many ways it is an ideal electrode material, however, it oxidizes at positive potentials. Besides these common materials, intrinsically conducting polymers and carbon nanotubes can be used alternatively to enhance biocompatibility.[83]

Charge balancing is another well known concern,[83] since injecting too much charge

into the tissue without taking it back out again can cause many problems.

Various established procedures of stimulating neurons are used clinically. They include transcranial magnetic stimulation (TMS) in which eddy currents are directly induced in the brain through the application of an electromagnetic field,[84] electrocortical stimulation (mapping) with surface electrodes,[85] deep brain stimulation[53] with depth electrodes, and microelectrode arrays.[86]

## 7.2 Powering of Wireless Implants

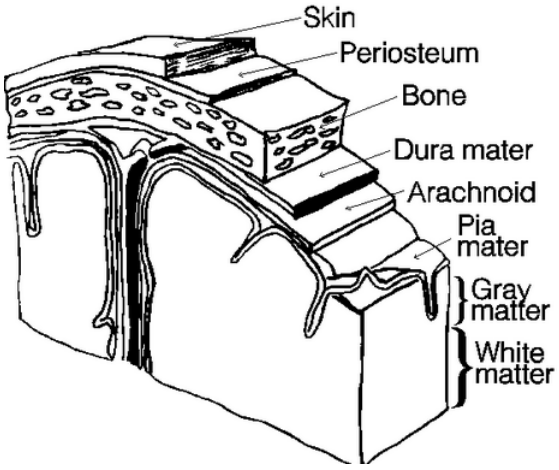


**Figure 7.1:** Layers covering brain, and cerebral cortex[6]

The various layers covering the brain (shown in figure 7.1) are important for its function and protection, but pose a special challenge when trying to stimulate the brain tissue while being minimally invasive. Neural implants with wires connecting them to an external power supply can easily be dislocated by the movement of these

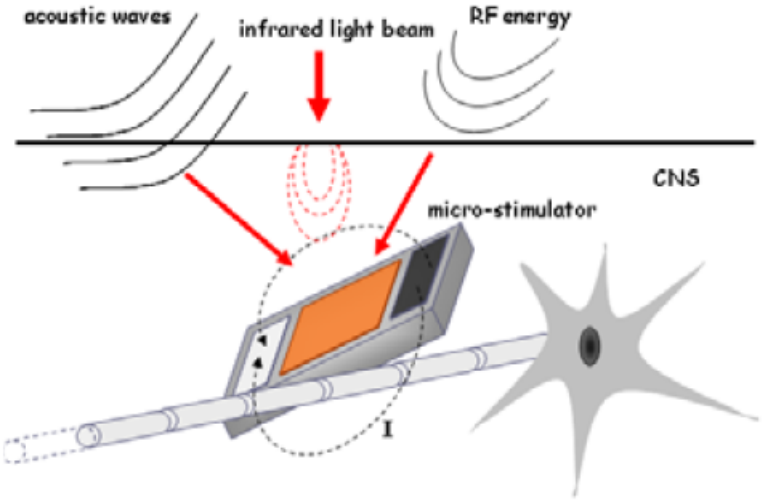


**Figure 7.2:** A wireless neural stimulation implant with acoustic (ultrasound), optical (infrared light) or electromagnetic powering. Depending on the coupling efficiency, the external power source can be located outside the body, or just above the dura mater.[7]

wires and require an opening in the biological tissue which can lead to infections. Tetherless implants are thus of great interest due to their reduced invasiveness and increased stability. Powering approaches include the use of a battery, local power harvesting from the biological tissue, or wireless power supply from an external power source. Local power harvesting approaches include generating power from glucose[87] or temperature gradients in the environment,[88] as well as the use of piezoelectric elements[89] which pick up motion from stimulated muscles.[90] Wireless power supply can be provided using light, ultrasound waves[58] or electromagnetic fields, including capacitive or inductive coupling. For neural implants, inductive near field or midfield powering at high frequencies is of special interest, since it allows for small implant sizes as will be discussed later.

### 7.2.1 Inductive Coupling

#### 7.2.1.1 Physical Modeling

The Maxwell equations, and especially two of them, form the foundation of inductive coupling, and are thus the main equations that simulation programs are based on: Ampere's law (equation 7.2) describes the generation of magnetic fields as a result of electric current or a time varying electric field. It describes the effect that occurs when a primary coil is driven with a high current in order to generate a magnetic field:

$$\vec{\nabla} \times \vec{H} = \frac{\partial \vec{D}}{\partial t} + \vec{J} \tag{7.2}$$

Here, $\vec{H}$ is the magnetic field strength, $\vec{D}$ is the electric displacement, $\vec{J}$ is the free electric current density.

Faraday's law of induction (equation 7.3) describes the fact that time-varying magnetic fields induce electric fields. This allows for voltage and thus current induction on the secondary side of a loosely coupled transformer, which can be formed by a neural implant on-chip inductor.

$$\vec{\nabla} \times \vec{E} = -\frac{\partial \vec{B}}{\partial t} \tag{7.3}$$

Here, $\vec{E}$ is the electric field strength and $\vec{B}$ is the magnetic flux density.

In the integral form of Faraday's law (equation 7.4) it can be seen, that more

voltage is induced on a loop for more change in B field over time enclosed by this loop. This can be achieved by a higher magnetic flux density, a higher field frequency, or by increasing the area that the loop encloses.

$$\oint_C \vec{E} d\vec{s} = -\iint_A \frac{\partial \vec{B}}{\partial t} d\vec{A} \tag{7.4}$$

Here, $\vec{E}$ is the electric field strength and $\vec{B}$ is the magnetic flux density, and A is a surface bounded by the contour C.

Sonnet Software, a high frequency electromagnetic simulation software,[91] is used for various electromagnetical simulations in this thesis. It uses the Method of Moments (MoM) and applies it directly to Maxwell's equations in order to solve planar 3D problems, making it ideal for analyzing layered structures such as CMOS chips or printed circuit boards. A mesh is laid over the geometrical model and multiple iterations involving 2D FFT (2D Fast Fourier Transform) are performed for each part of the mesh until an electromagnetical solution that complies with the boundary conditions of zero voltage across a conductor is found. A detailed explanation regarding this can be found online[92] and in the literature.[9394]

The other software used for electromagnetical simulations in this thesis is HFSS (high frequency structural simulator)[95] by ANSYS. In contrast to Sonnet it uses an adaptive mesh, making it more suitable to solve problems with great variation in the dimensions of geometries within the model, such as coupling between a large primary

inductor and a small secondary inductor. It allows for the use of the Finite Elements Method, as well as the Method of Moments or a Hybrid approach.[96]

#### 7.2.1.2 Radiofrequency Identification (RFID) Tags

Radiofrequency identification (RFID) tags often follow the same powering scheme as inductively powered neural implants, and thus can be used for human implant devices.[97] Passive RFID tags are read with so called readers (i.e. the primary inductor, or transmitter) that generate a magnetic near field and thereby power the RFID tag to allow for the sending of data (figure 7.3). The most common RFID frequency ranges are 125/134 kHz, 13.56 MHz, 860 - 960 MHz, and 2.4 - 2.45 GHz.[98] The frequencies in the upper MHz and lower GHz range require special attention when the frequency is so high that the corresponding wave length is small enough to be on a similar scale as the conductor length of the primary inductor. In this case, the primary inductor loop needs to be segmented into smaller parts that get matched with series capacitors in order to keep the current in phase along the conductor. This allows for the field, which is generated by the current flowing around the loop, to reinforce itself.[99]

### 7.2.2 Brain Tissue Safety in Electromagnetic Fields

When transmitting power to the implant inductively, biological tissue is exposed to electromagnetic fields. If the field strength exceeds certain limits, the tissue can be burnt or stimulated directly by the field (as desired for transcranial magnetic stimu-

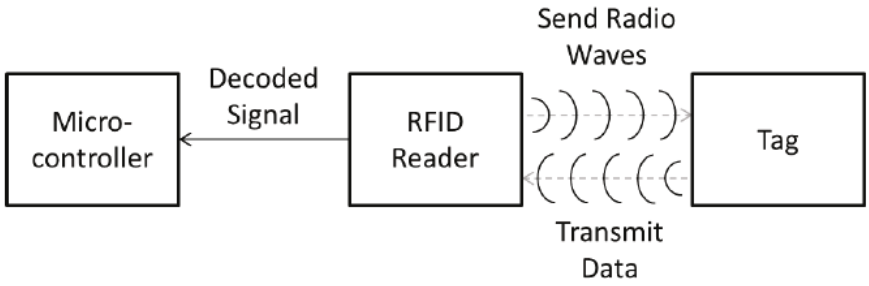


**Figure 7.3:** RFID scheme:[8] The RFID reader sends power (and possibly data) in the form of radio waves, thereby powering the RFID tag. The RFID tag sends data back to the reader where it is decoded and sent to a microcontroller for further processing.[9] This data can correspond to an ID of the tag, but can also be information that the tag has recorded using a sensor.

lation). Recommended limits can be found in various guidelines, including ICNIRP 1998.[10] Only if the induced fields have effects that go outside the range of endogenous physical and biological noise in cellular membranes, can damage be expected.[10] The specific absorption rate (SAR) is the power that is absorbed by the human body when exposed to certain electromagnetic fields, in other words, the rate at which energy is absorbed. There are recommended local maximal SAR values for brain tissue, as well as recommended local maximal SAR values for whole body average, and HFSS can be used to plot SAR in simulated biological tissue. Body simulations of frequency dependent properties of the tissue[100] can determine maximal magnetic field density values $\mathbf{B}$ (e.g. shown in figure 7.4) which lead to SAR values within safe ranges. Limiting SAR is especially important for electromagnetic fields at frequencies higher than around 100 kHz as they can lead to significant heating and power absorption.[10] It is therefore important to have a power link that is efficient and does not dissipate

unwanted power into the tissue.

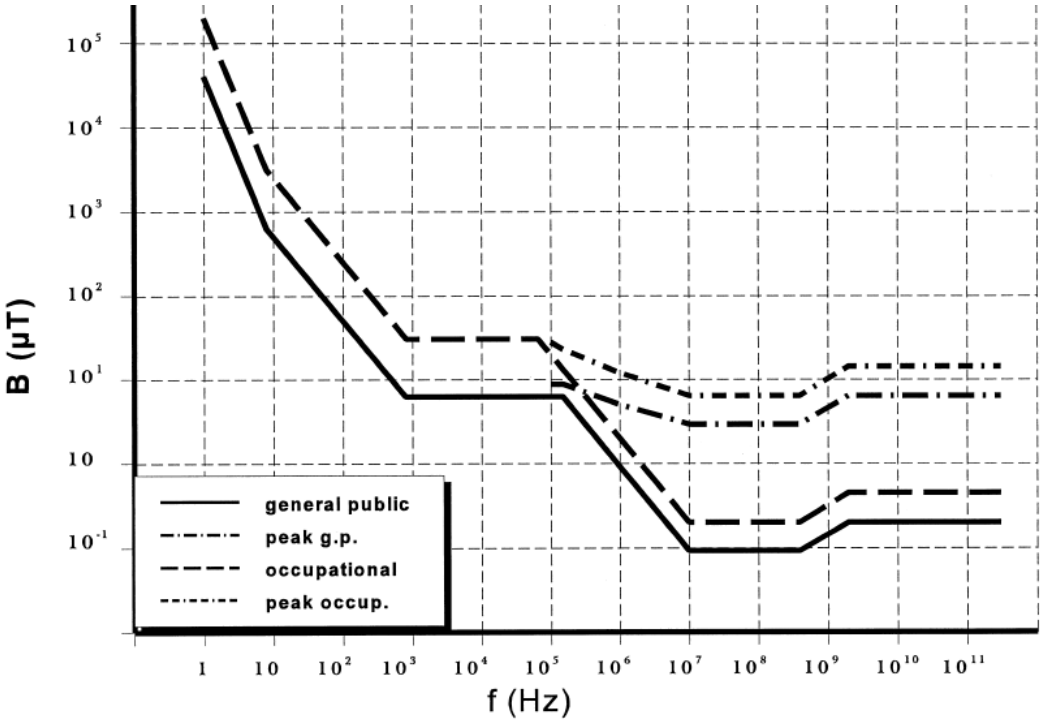


**Figure 7.4:** Reference levels of RMS magnetic field density B for time varying magnetic fields, according to ICNIRP 1998.[10] General decrease over frequency can be seen, however, reference levels increase again starting at around 800 MHz.

# Chapter 8

# Methods

The main design constraints of wireless neural implants, such as the proposed micro-bead (figure 8.1), are imposed by their small size. This limits the area available for circuitry and, in the case of inductive coupling, leads to smaller secondary inductors which can capture less power from a given oscillating magnetic field than bigger inductors would. Increasing the amplitude of the field would increase the absolute power delivered to the implant, but is limited by the specific absorption rate (SAR) regulations in order to avoid tissue damage. Reducing the power required by the circuit is thus a good approach for wireles neural implants. Optimizing the inductive power link, and especially the secondary inductor design, further ensures that as much power as possible can be delivered to the neural implant circuit, i.e. the load.

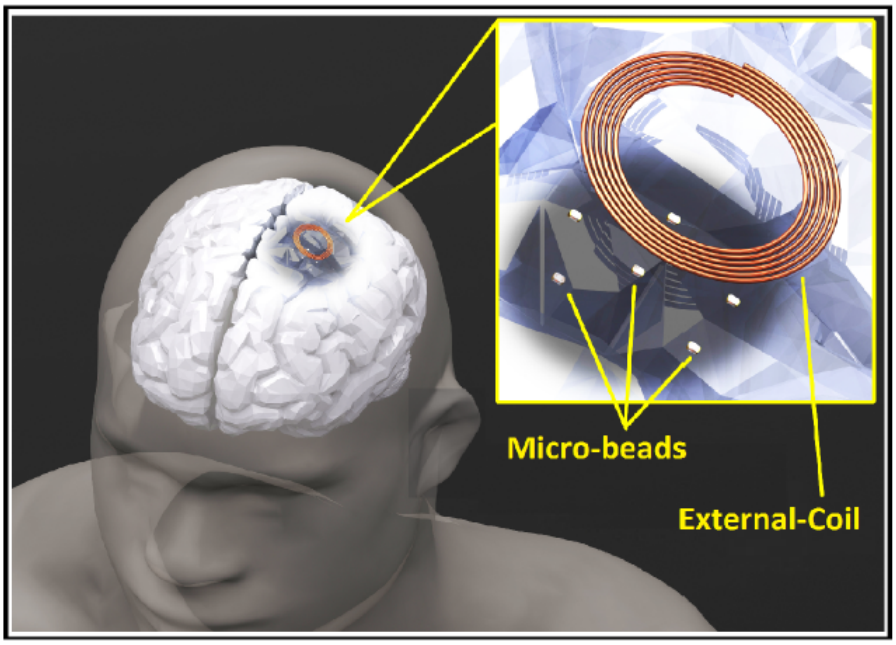


**Figure 8.1:** The micro-bead.[11]

## 8.1 Low-Power Neural Implant Circuit

In order to reduce power consumption and area, a fully analog neural implant chip was designed by Adam Khalifa.[11] It is wirelessly powered through an on-chip inductor with a matching network in the form of a resonant capacitor, and consists of a rectifier, charge pump, filter capacitor, voltage reference, regulator and a current driver. This can be seen in figure 8.2, and the individual blocks are designed to consume little area and power. The chip consumes about 16 $\mu$W and occupies an area of 220 $\mu$m x 180 $\mu$m. The blocks are discussed in[11] and are thus not further detailed here. The individual chips are addressed based on their individual resonant frequency that they are tuned for.

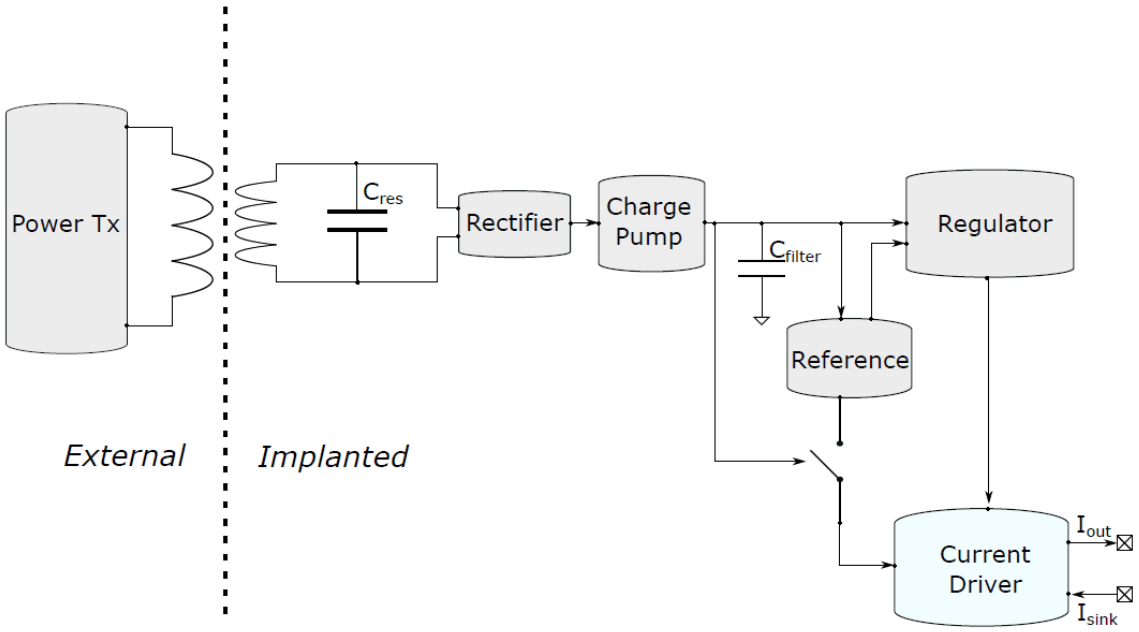


**Figure 8.2:** Block diagram of neural implant.[11]

### 8.1.1 Control Concept

The designed neural implant does not contain a digital control block since this would increase area and power consumption. Instead, the implant's control concept is that the current driver drives a preset current into the neural tissue whenever the implant is powered, and does not stimulate when the implant is not inductively powered. Stimulation frequencies between 4 Hz and 1 kHz require the least injected current to activate nerves (i.e. neurons).[10] They are thus of special interest for this design since a lower stimulation current for a given load impedance of the tissue dissipates less power in the load. With a frequency of around 900 MHz to power the implant, i.e. a frequency that is $9 \cdot 10^5$ times higher than 1 kHz, it is very feasible to switch the implant on and off at these desired stimulation frequencies, of course,

depending on the start-up time and shut-down time of the implant circuitry. Individual implants are addressed based on their resonance frequency. They are therefore designed with different matching capacitors to allow for highest power transmission at specified frequencies while filtering out other frequencies. In this thesis, an implant with a resonance frequency at 900 MHz is considered.

### 8.1.2 Injected Charge

In the present design, the stimulation current amplitude is fixed to avoid the need for digital processing of amplitude control data. An increase in the total charge delivered to the neural tissue can be achieved by prolonged stimulation (as long as the charge balancing is not perfect and the average current is thus greater than zero): The charge injected over a time interval of $\Delta t$ can be calculated from the injected current I(t) as follows:

$$Q(\Delta t) = \int_{t}^{t+\Delta t} I(t)dt \tag{8.1}$$

### 8.1.3 Input Impedance of Implant Circuit

The power consumption and thus input impedance of most implant circuits is usually time dependent, thus making the load impedance seen by the matching network time-dependent.[101] Inductive power link optimization, however, depends on the load

impedance, and thus becomes challenging for a non-constant load impedance. This challenge can be addressed by using an additional inductor that can transform any load impedance to the desired optimal load impedance, or by a Q-modulation power management technique where the duty cycle of a switch is adjusted to allow for automatic load modulation.[102] For this work, unless stated otherwise, a constant load impedance of $3k\Omega$ is assumed (which is a very rough estimate given it is the average impedance calculated from Cadence simulations of the neural implant circuit; to be specific, the input voltage is divided by the input current to the circuit at every time point). Assuming a constant load impedance is a typical, although often unrealistic, approach for inductive power link optimization. Other work assumed a fixed load impedance of $50\Omega$,[10312] $500\Omega$,[104] $1k\Omega$[105] or $1.5k\Omega$, $5k\Omega$ and $10k\Omega$[13] for the power link optimization.

## 8.2 Inductive Power Link Model

The inductive power link between a transmitter and a receiver can be described by a two port model that describes the transfer function between primary and secondary port. The behavior of such a two port model can be characterized using a complex matrix such as the scattering matrix **S** (in equation 8.2) or the impedance matrix **Z** (in equation 8.3).

At high frequencies, power waves and their reflections, rather than voltage and

currents, are the measured values of choice. This is due to the fact that open loops and shorted connections no longer provide zero current or zero voltage conditions, making analysis harder. The transmission of the incoming power waves $a$, as well as the magnitude of the outgoing or reflected wave $b$, is described by the scattering matrix as follows:

$$\begin{pmatrix} b_1 \\ b_2 \end{pmatrix} = \begin{pmatrix} S_{11} & S_{12} \\ S_{21} & S_{22} \end{pmatrix} \cdot \begin{pmatrix} a_1 \\ a_2 \end{pmatrix} \tag{8.2}$$

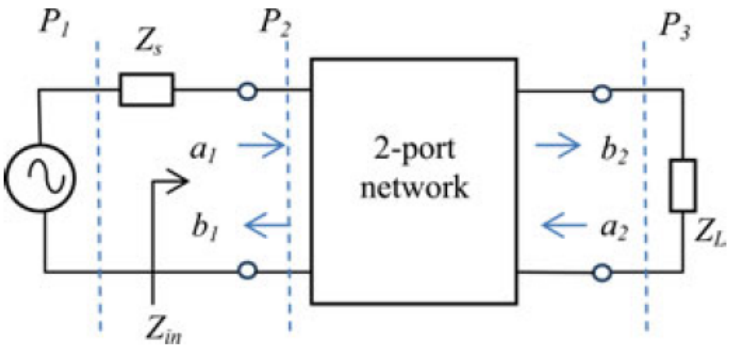


**Figure 8.3:** 2 port model power transmission with power waves.[12]

The elements $S_{11}$ and $S_{22}$ are the reflection coefficients of the individual ports for a set characteristic impedance (which is usually 50 ohms). This characteristic impedance is taken as the source impedance and as the load impedance in the S parameter measurements. High reflection coefficients mean that only a small fraction of the incoming power enters the two port network. With little power entering the input port, only little power can be transmitted to the secondary port. The elements $S_{21}$ and $S_{12}$ are the transmission coefficients and correspond to the power transfer from port 1 to port 2 and inversely. In passive networks, they are equal to each

other.[106]

A two port network that is driven by a source with the source impedance $Z_S$ and connected to a load impedance $Z_L$, as well as the power waves $a$ and $b$ corresponding to each port, can be seen in figure 8.3.

The S parameter matrix can be transformed into a Z matrix using simple equations. The resulting relationship for the impedance matrix Z describes current and voltage relationships at port 1 and 2 as follows:

$$\begin{pmatrix} V_1 \\ V_2 \end{pmatrix} = \begin{pmatrix} Z_{11} & Z_{12} \\ Z_{21} & Z_{22} \end{pmatrix} \cdot \begin{pmatrix} I_1 \\ I_2 \end{pmatrix} \tag{8.3}$$

### 8.2.1 Estimate of Power Delivered to Load using Impedance Matrix

An inductive power link can be described using the Z-matrix as shown in the equivalent circuit diagram in figure 8.4. This subsection is based on an analysis found in the literature.[13]

$Z_{in}$ is the input impedance into the 2 port network, seen on the primary side. $Z_{22}$ is the impedance of the secondary side. At a defined frequency, this impedance $Z_{22}$ can be described by a first order model of a series resistance $R_{22}$ in series to a series inductance $L_2$. They are the effective series resistance and the effective series inductance of the secondary side. $Z_L$ is the load impedance of the circuit, and includes

the matching network for the secondary inductor in the form of a parallel capacitor, as well as the load resistance $R_L$ which is described by the neural implants input impedance (assumed to be real) and is assumed to be fixed at $3k\Omega$ in this work. The resonant parallel capacitor is assumed to be lossless and to perfectly cancel the imaginary admittance of the inductor at the resonant frequency $\omega_0$. It thus has a value of:

$$C_2 = \frac{1}{\omega_0^2 \cdot L_2} \tag{8.4}$$

At the resonant frequency, the parallel connection of the load resistance $R_L$ and matching capacitor $C_2$ can also be described by a load resistance $R_{LS}$ in series to a capacitance $C_{2S}$. For the case that $R_L \gg \omega_0 L_2$ (which is usually the case for applications like ours), $C_{2S} \approx C_2$ and the equivalent series load impedance is:

$$R_{LS} \approx \frac{(\omega \cdot L_2)^2}{R_L} \tag{8.5}$$

The power delivered to the load $Z_L$ is given by the product of the squared root mean square (RMS) current flowing through it, and the resistive component of the load in which the power is dissipated:

$$P_L = (I_{2_{RMS}})^2 \cdot Re\{Z_L\} \tag{8.6}$$

In this model, the RMS secondary current $I_{2_{RMS}}$ is determined from the secondary induced voltage $V_2$ and the impedance seen by this voltage, as shown in figure 8.4:

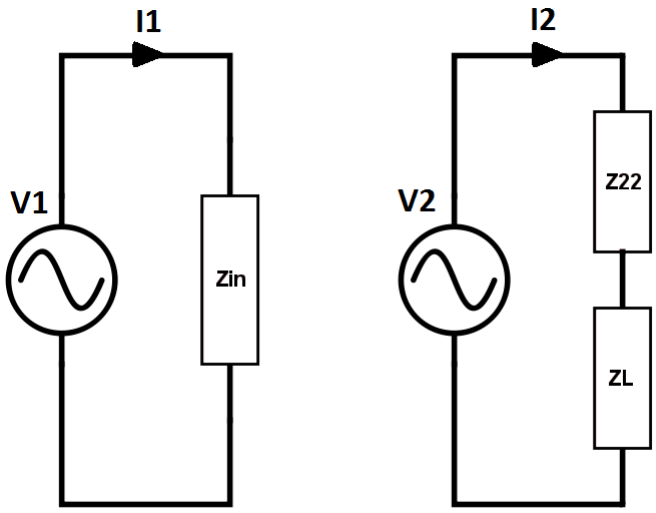


**Figure 8.4:** Schematic describing 2 port model for loosely coupled inductive coupling, where $V_2 = Z_{21} \cdot I_1$.[13]

$$I_{2_{RMS}} = \frac{V_{2_{RMS}}}{Z_{22} + Z_L} \tag{8.7}$$

In turn, the induced secondary RMS voltage $V_{2_{RMS}}$ here is dependent on the primary current and $Z_{21}$, which is related to the coupling coefficient between the coils.

$$V_{2_{RMS}} = I_{1_{RMS}} \cdot Z_{21} \tag{8.8}$$

The primary current depends on the primary voltage and the impedance seen by port 1:

$$I_{1_{RMS}} = \frac{V_{1_{RMS}}}{Z_{in}} \tag{8.9}$$

This input impedance is given by the following equation:

$$Z_{in} = Z_{11} - \frac{Z_{12} \cdot Z_{21}}{Z_{22} + Z_L} \tag{8.10}$$

For very low coupling, which is usually the case for small secondary inductor sizes, this equation simplifies to:

$$Z_{in} \approx Z_{11} \tag{8.11}$$

thus leading to

$$I_{1_{RMS}} \approx \frac{V_{1_{RMS}}}{Z_{11}} \tag{8.12}$$

The power delivered to load is described by:

$$P_L = \frac{|I_{1_{RMS}}|^2 \cdot |Z_{21}|^2}{|Z_{22} + Z_L|^2} \cdot Re\{Z_L\} \tag{8.13}$$

Since the imaginary parts of $Z_{22}$ and $Z_L$ cancel for frequency tuning, at resonance the following equation results (where $Re\{Z_{22}\} = R_{22}$ and $Re\{Z_L\} = R_{LS}$):

$$P_L = \frac{|I_{1_{RMS}}|^2 \cdot |Z_{21}|^2}{|R_{22} + R_{LS}|^2} \cdot R_{LS} \tag{8.14}$$

Equation 8.14 can be re-written using the complex coupling coefficient (includes

both the imaginary and the real parts of $Z_{21}$)

$$\kappa = \frac{|Z_{21}|}{\sqrt{|Im\{Z_{11}\} \cdot Im\{Z_{22}\}|}} \tag{8.15}$$

which leads to

$$P_L = \frac{|I_{1_{RMS}}|^2 \cdot \kappa^2 \cdot \omega^2 \cdot L_1 \cdot L_2}{|R_{22} + R_{LS}|^2} \cdot R_{LS} \tag{8.16}$$

with $R_{LS}$ from equation 8.5, and with the effective inductances $L_1$ and $L_2$ of the primary and secondary inductors:

$$Im\{Z_{11}\} = \omega \cdot L_1 \tag{8.17}$$

and

$$Im\{Z_{22}\} = \omega \cdot L_2 \tag{8.18}$$

The power transfer efficiency of the inductive link can be calculated as follows:

$$\eta = \frac{P_L}{|I_{1_{RMS}}|^2 \cdot R_{11}} \tag{8.19}$$

It corresponds to the power delivered to the load, divided by the power that is dissipated in the effective resistance of the primary inductor.

## 8.3 Inductive Power Link Optimization

The present work analyzes setups with very small coupling coefficients between the primary and secondary inductor - they are much lower than 0.1. This loose coupling allows for a more independent design of primary and secondary inductor, since detuning - the undesired change of resonant frequency, e.g. in the presence of a strongly coupled secondary inductor, only occurs at coupling coefficients of 0.1 and higher.[107] The maximum size of the secondary inductor, as well as the separation distance between the primary and secondary inductor, are determined by the application, and they influence all further design choices. The operating or transmission frequency is another important design choice, and is related to the secondary inductor size.

### 8.3.1 Transmission Frequency

Many inductively powered neural implants receive power at frequencies below 20 MHz.[108109110] Recent studies, however, have shown that increasing frequencies up to the low GHz range can improve power transfer to mm sized neural implants.[111] One special advantage of higher frequency power transmission is the increased voltage induction in smaller implants for a given magnetic field amplitude, thus allowing for a smaller implant size. A disadvantage is the increased power loss in tissue, but it is argued that the advantages overcome this disadvantage. Lower optimal frequency bounds for transmission through bone and skin were determined to be 700 MHz and

800 MHz,[108] and accordingly a transmission frequency of 800 MHz to 1200 MHz was chosen as the frequency range of operation. In a first step, a single transmission frequency from this range was chosen for the further analysis. Accordingly, all further analysis is performed with regards to a transmission frequency of 900 MHz.

### 8.3.2 Separation Distance

The separation distance that is required between the primary and secondary inductor depends on the distances given by the application: For a wireless neural implant which is placed within the brain tissue and is powered from outside the scalp, this distance is determined by the thickness of these layers. The fact that the primary power loss and related tissue damage can be reduced by placing the primary inductor a little further away (and not directly adjacent to the biological tissue)[13] adds a layer of air to this distance. The layers passed by the wireless power from primary to secondary side can be seen in figure 7.1 and include: air, scalp (skin), skull (bone), meninges (including the dura mater) and brain tissue. In later design stages, the implant coating should also be taken into account. Common approaches in the literature consider a separation distance of 15 mm[13] or 10 mm,[104] but smaller separation distances are also reasonable in smaller animal models (e.g. rats) or when skull thinning is used. In order to increase chances of successful power transfer while remaining in this range, a separation distance of 5 mm was chosen for this work. However, an even smaller separation distance would be reasonable for small or young

animals. Mouse skull bones are below 730 um thick[112] and the thickness added by the skin and meninges is on a similar range. Skull thinning in mice can even achieve a skull thickness of 10 or 15 um,[113] thus further reducing the required distance.

### 8.3.3 Primary Inductor Design

Printed circuit board (PCB) primary inductors allow for an accurate fabrication process and thus simulation, as well as for cm-sized designs. Square, hexagonal and octagonal primary inductors are the most common shapes encountered in the literature. As in the case of the secondary inductor where it will be explained in more detail, for a given outer dimension and shape, the trace width, trace spacing and number of turns are the parameters to be chosen. The skin effect is to be considered in the choice of trace width, since the current will flow on an increasingly thinner surface layer of the traces at higher frequencies, and thus resistance improvement will be slowed down for increasingly wider traces.

The skin depth can be calculated as follows:

$$\delta(f) = \frac{1}{\sqrt{\pi \cdot f \cdot \mu_0 \cdot \mu_r \cdot \sigma}} \tag{8.20}$$

Where f is the frequency, $\mu_0$ is the permeability in vacuum, $\mu_r$ is the relative permeability, and $\sigma$ is the conductivity.

A single turn or loop antenna will lead to low parasitic parallel capacitance and

thus reduces leakage compared to primary coils with multiple turns. It further leads to a trace length which is electrically small compared to the wavelength, an important feature at high frequencies.

The wavelength for a given frequency is:

$$\lambda = \frac{c}{f} \tag{8.21}$$

Here, c is the speed of light, $\lambda$ is the wavelength, and f is the frequency. The speed of light c is material dependent and can be calculated as follows:

$$c = \frac{1}{\sqrt{\epsilon_0 \cdot \epsilon_r \cdot \mu_0 \cdot \mu_r}} \tag{8.22}$$

At high frequencies such as the 900 MHz used in this work, the wavelength of the electromagnetic field is often no longer multiple magnitudes bigger than the trace length, depending on the trace length. (Specifically, at 900 MHz this wavelength is 333 mm in air, thus for $\epsilon_r = 1$ and $\mu_r = 1$.) This means that the current can then no longer be said to be in the same phase along the trace length. One can assume that the phase of the current is approximately constant along a trace of the length l when:

$$l < \frac{\lambda}{2\pi} \tag{8.23}$$

At 900 MHz in air, this leads to a length of $l < 53$ mm. If the current is in the

same phase all along the trace (and this phase is not a spatial zero crossing of the current wave), then the local current will reach its maximum at all locations in the trace at the same time, allowing for a strong build-up of magnetic field through reinforcement from all trace parts at the same time. This leads to a more uniform field and increases the field strength generated by a defined current. Further, this leads to the reduction of local field peaks which is useful when trying to adhere to local SAR limits,[14] thus increasing the transmitted power to a secondary inductor for a given input power. Since wavelength is frequency dependent, higher frequencies lead to smaller wavelengths. This means that the phase of the current along a given trace will change more than at a lower frequency.

#### 8.3.3.1 Optimal Diameter for given Separation Distance

For a given separation distance $\Delta z$ between a primary and secondary inductor, with a secondary inductor diameter of $d_2$ where $d_2 << \Delta z$, a good choice for the primary inductor diameter can be calculated as follows:[114]

$$d_{1,opt} = 2 \cdot \sqrt{2} \cdot \Delta z \tag{8.24}$$

This equation is based on the fact that a circular wire loop of that diameter will generate a maximal magnetic field strength $\vec{H}$ at the given separation distance $\Delta z$ for a defined current. It is thus a good approximation for a printed single loop square or octagonal inductor and was used here, however, could be further optimized by

simulation.

#### 8.3.3.2 Segmented Loop Antenna

Segmented loop antennas allow for this ideal size of the primary inductor in the case of otherwise electrically large inductor sizes that are comparable to the wavelength, by keeping the current along the loop in phase[115116117118] . After the maximal length for in-phase current of a trace is reached, a capacitor that is matched to this segment is connected in series to it and thereby brings the current back to zero phase shift. The other side of this capacitor is connected to the next trace segment etc. It is to be noted that a segmented loop antenna is not required for a 5 mm separation distance or less here, due to an electrically small primary inductor size at 900MHz.

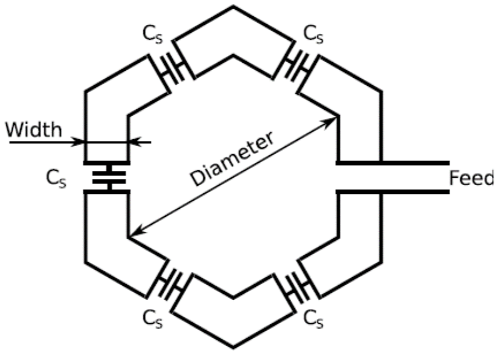


**Figure 8.5:** Segmented loop antenna with capacitors that match individual segments keep current in phase along trace.[14]

### 8.3.4 Secondary Inductor Design

The long-term goal of this project is to achieve a wirelessly powered neural implant with a dimension of $100\mu m$ in each direction. Thus, the desired maximal outer dimension of the implanted secondary inductor is $100\mu m$. In this work, in order to investigate the design space, secondary inductors with outer dimensions of 200 $um$, 100 $um$ or 50 $um$ are analyzed with regards to their ability of maximizing power transfer to the load.

On-chip spiral inductors offer the advantage of small feature sizes, as well as convenient design, and structures that can be well simulated.

#### 8.3.4.1 CMOS Technology Layers

Most CMOS (complementary metal-oxide semiconductor) processes have multiple metal layers and thick top metal layers. These thicker metal layers are ideal for the placement of secondary inductors: The thick metal allows for a lower series resistance and thus higher quality factor. In addition, these layers are very distant from the lossy doped silicon substrate of the chip which lies below the bottom layer. Despite the advantages of the top metal layer, all metal layers of the CMOS process can be used to design an optimal secondary inductor for the implant.

Including lower metal layers in addition to the thicker top metal layer can increase inductance through a higher number of turns. It can also increase the parasitic capacitance of the inductor as part of secondary parallel matching network (although

this is considered as lossy and should be avoided).

Various multi-layer inductor designs add to the number of typical design approaches, however, usually at the cost of increased series resistance from the lower metal layers and increased parallel parasitic capacitance and resistance. The so-called miniature 3D-inductors[15] are spiral inductors which form a spiral on one layer and connect the center point to another layer's spiral's center point by a via, as can be see in figure 8.6. They are used as the muli-layer inductors in this thesis, and have an increased self-resonant frequency due to reduced parasitic capacitance compared to inductors that spiral down on all layers before spiraling inwards by one turn etc.

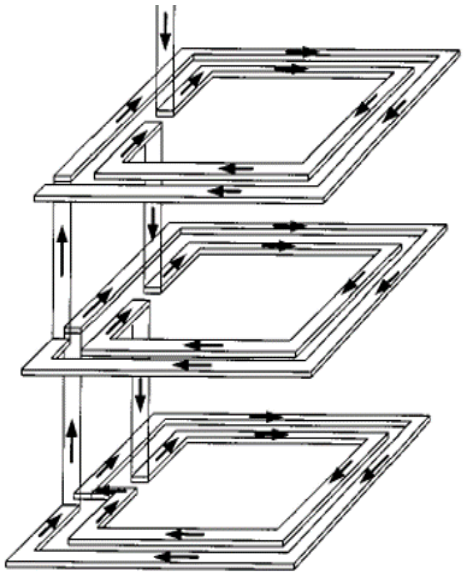

**Figure 8.6:** Miniature 3-D Inductor[15]

Typical inductor designs involve traces that enclose areas which are parallel to the chip surface. There are, however, so called interconnect technology inductors that use vias as traces and enclose areas perpendicular to the chip surface. This interconnect

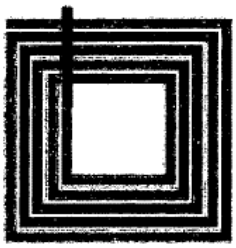

**Figure 8.7:** Conventional single layer spiral inductor with connection back out on lower metal layer.

technology can reduce substrate losses and chip area.[119] They are, however, not studied in this work since the distance between the top and bottom metal layer is not big enough to form an outer inductor dimension of 50 um or more.

### 8.3.4.2 Inductor Shape

Spiral inductors can be of different shapes, such as squares, rectangles, hexagons or octagons. For a defined outer dimension, square inductors enclose a larger area with their traces, thus - following Faraday's law (equation 7.3) - leading to a higher induced voltage on the secondary side. Hexagonal and octagonal inductors have the advantage of a more uniform field generated from current flowing through them, and a more uniform current distribution within their traces, but are not studied for the secondary inductor design here.

#### 8.3.4.3 Geometrical Inductor Parameters

Besides the outer dimension, design parameters of a top metal layer spiral inductor are the trace width, trace spacing, and the number of turns. The shape and location of the feedlines is another design parameter, but here an effort is made to keep them consistent between designs to allow for a comparison of the remaining parameters. Increasing the trace width will reduce the series resistance of an inductor, however, takes up more space and thus reduces the area enclosed by the inner turns. Increasing the spacing between traces will lead to a decreased inter-trace capacitance, thereby reducing losses, however, also decreases the area enclosed by inner turns. Increasing the number of turns will increase the inductance of the inductor, but also increases its resistance and is limited by the other parameters. This thus reduces the qualitiy factor, which is the ratio of imaginary impedance to real impedance of the inductor. Since the outer dimension of the square spiral inductor is fixed here, a trade-off between the geometrical parameters has to be made, according to the following equation for a single layer spiral inductor:

$$d_2 \geq 2 \cdot (w_2 + s_2) \cdot n_2 \tag{8.25}$$

Here, $d_2$ is the secondary side outer dimension, $w_2$ is the secondary trace width, $s_2$ is the secondary trace spacing and $n_2$ is the secondary number of turns.

Increasing the number of layers allows for increased numbers of turns, but it is to

be considered, that placing vias required to connect between layers takes away from the trace length on each layer.

#### 8.3.4.4 Further Inductor Enhancement

A vast variety of methods for further enhancing the secondary inductor design exist. This includes patterned ground shield,[120] etching part of the material and substrate around the inductor away[121] to reduce substrate losses, or creating an area with no doping below the inductor ('bipolar block').

### 8.3.5 Coupling Coefficient

The coupling coefficient indicates how much of the field generated by the primary inductor passes through the secondary inductor, and thus greatly influences the power transfer.

Optimization of power links is dependent on the medium - more than a 9% improvement in power transfer efficiency can be achieved when directly optimizing an inductive power link for a specific biological medium.[104] The main differences introduced by biological tissue compared to air as the transmission medium are the losses seen on the primary side due to coupling into the tissue. The primary side's coupling to the secondary inductor, however, is not much affected by this, since tissue conductivity is much lower than that of metal. The coupling coefficient between two inductors in biological tissue is thus very similar to their coupling coefficient in

air.[13] The coupling coefficient for two parallel conductor loops that are centered on the same z-axis can be estimated for a primary loop with radius $r_1$ and a smaller secondary loop with radius $r_2$, that are separated by a distance of $\Delta z$, as follows:[122]

$$k(\Delta z) = \frac{r_1^2 \cdot r_2^2}{\sqrt{r_1 \cdot r_2} \cdot (\sqrt{\Delta z^2 + r_1^2})^3} \tag{8.26}$$

This coupling coefficient estimation is a good first order approximation. The first order approximation of the coupling coefficient between two inductors is not affected by the number of turns of the inductors.[13]

### 8.3.6 Frequency Tuning

Frequency tuning allows for a circuit to resonate at a desired frequency, leading to a high voltage or high current at that frequency and filtering at other frequencies. It is often referred to as frequency matching. Series matching of the imaginary impedance on the primary side can be achieved by placing a resonant capacitor in series to the primary inductance. It leads to zero imaginary impedance and thus maximal current amplitudes. High current amplitudes on the primary side allow for increased magnetic fields, and thus increased power transfer. Series matching is therefore the matching of choice on the primary side. At resonance, the following equation holds for series matching:

$$Im\{Z\} = j\omega_0 L - j\frac{1}{\omega_0 C} = 0 \tag{8.27}$$

Parallel matching of the imaginary admittance on the secondary side can be achieved by placing a resonant capacitor in parallel to the secondary inductor. It leads to zero imaginary admittance and thus maximal voltage amplitudes. High voltage amplitudes on the secondary side increase the chance of supplying enough voltage for the circuit on the secondary side to turn on, thus allowing proper functioning of the implant. Parallel matching is therefore the matching of choice on the secondary side. At resonance, the following equation holds for parallel matching

$$Im\{Y\} = j\omega_0 C - j\frac{1}{\omega_0 L} = 0 \tag{8.28}$$

The resonant frequency $\omega_0 = 2\pi f_0$ is determined as follows:

$$\omega_0 = \frac{1}{\sqrt{L \cdot C}} \tag{8.29}$$

This equation can be rearranged to determine the resonant capacitance required to match a given inductor at a given frequency, as done in equation 8.4.

# Chapter 9

# Experimental Setup

## 9.1 Calculation

The optimal diameter of the primary inductor is estimated according to equation 8.24 for separation distances of 1 mm, 2 mm, 3 mm, 5 mm and 10 mm between the primary and secondary inductor. Further, the coupling coefficient between a round loop primary inductor of this respective optimal diameter and a round loop secondary inductor of 50 $\mu m$, 100 $\mu m$, 200 $\mu m$ or 300 $\mu m$ diameter is estimated for these separation distances using equation 8.26, thus assuming perfect center allignment.

## 9.2 Simulation

### 9.2.1 Primary Inductor

Primary inductors of the estimated optimal diameter are designed in Sonnet Software. Each of these primary inductors is octagonal and has a trace width of 200 $\mu m$ made of 1oz thick copper on a 1.5 mm FR4 PCB substrate. An autogrounded port is placed between the two inductor ends, and the setup simulated at 900 MHz. The current distribution is plotted on the inductor designed for 1 mm separation distance. The parameters for this are a stimulus amplitude of 1 V and a frequency of 900 MHz or 15 GHz, to compare the phase distribution of the current along the trace for both frequencies. A primary inductor with a wider trace of 3 mm width is used in the estimation of the coupling coefficient to a small secondary inductor, as is described further below.

### 9.2.2 Secondary Inductor

37 on-chip spiral inductors with outer dimensions of 50 $\mu m$, 100 $\mu m$ or 200 $\mu m$ and a wide variety of trace widths $w$, trace spacings $s$ and number of turns $n$ are investigated. Further, one 300 um diameter secondary inductor is investigated. The geometrical specifications of the secondary inductors are given in figure 10.6). The layout of each inductor is drawn in Cadence (Virtuoso Analog Design Environment,

Cadence) and the respective GDSII files are imported individually to Sonnet Software. The metal and dielectric layer thicknesses and properties uesd in the simulation (shown in figure 9.1) correspond to those of the 0.18 um CMOS process that is used for chip fabrication. (However, with the following deviations: intrinsic silicon (conductivity of 4e-4 S/m) is used as the bulk material in the simulation, instead of p-doped silicon (conductivity of 7.4 S/m); the silicon oxide layer below the bottom metal layer is 0.31 um in the simulation, instead of 0.51 um). An autogrounded port is placed between the two inductor ends (port labels '1' and '-1'), and the setup of each inductor is simulated at 900 MHz. Such a setup can be seen in figure 9.2.

| Metal Layer Idx | Material | Thickness [um] | ε_rel |
|---|---|---|---|
| | Air | 100,00 | 1,00 |
| | Polyimide | 2,50 | 3,40 |
| | Silicon Nitride | 0,45 | 7,00 |
| | Oxide (SiO2) | 1,35 | 4,10 |
| A (top) | **Aluminum** | 4,00 | - |
| | Oxide (SiO2) | 4,10 | 4,10 |
| B | **Aluminum** | 0,48 | - |
| | Oxide (SiO2) | 0,55 | 4,10 |
| C | **Aluminum** | 0,48 | - |
| | Oxide (SiO2) | 0,55 | 4,10 |
| D | **Aluminum** | 0,48 | - |
| | Oxide (SiO2) | 0,55 | 4,10 |
| E | **Aluminum** | 0,48 | - |
| | Oxide (SiO2) | 0,40 | 4,10 |
| F (bottom) | **Copper** | 0,33 | - |
| | Oxide (SiO2) | 0,31 | 4,10 |
| | Silicon Substrate | 250,00 | 11,90 |

**Figure 9.1:** Layer details for simulation in Sonnet.

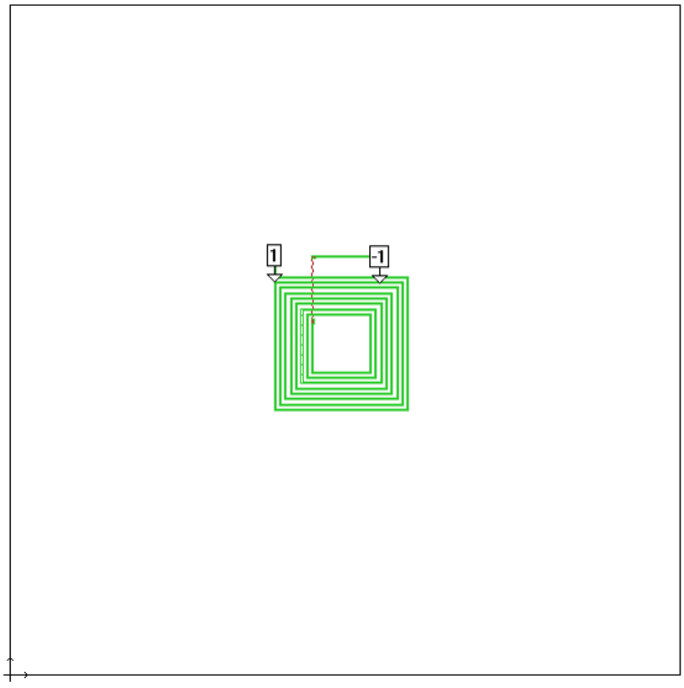


**Figure 9.2:** Simulation setup in Sonnet for a secondary inductor.

### 9.2.3 Coupling Coefficient

The two port model of an octagonal primary inductor loop and a square secondary inductor loop is simulated for a separation distance of 5 mm in air at 900 MHz, using HFSS (high frequency structural simulator, ANSYS). The two port model is then used to determine the coupling coefficient as shown in equation 8.15. The primary inductor has an average diameter (average of inner and outer diameter) based on the optimal diameter calculated for 5 mm separation distance, and a trace width of 3 mm. The secondary inductor has an outer diameter of 300 um and a trace width of 25 um. Both are one loop only. HFSS is used instead of Sonnet due to the great differences in size between primary and secondary inductor. HFSS has an adaptive

mesh that is suitable for simulating such geometry, while Sonnet uses the same mesh size across the entire setup and is thus less suitable.

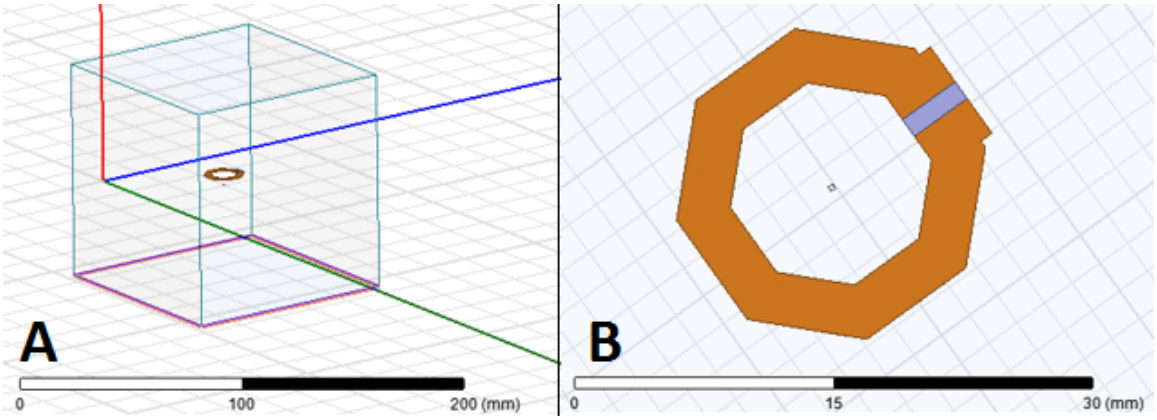


**Figure 9.3:** Simulation setup in HFSS to determine coupling coefficient for 5 mm separation distance and 300 um secondary inductor square loop. **A:** Side view, full setup. **B:** Top view, large primary inductor and small square secondary inductor loop in center.

## 9.3 Bench Top Experimentation

No measurement for the primary inductor or for the two port setup (primary and secondary inductor together; which would allow for the experimental determination of the coupling coefficient) is presented here.

### 9.3.1 Secondary Inductor

The secondary inductors are designed in Cadence (Virtuoso Analog Design Environment, Cadence) and sent out for fabrication on multiple 1.5 mm x 1.5 mm chips of a 0.18 um CMOS process (see figure 9.4). Since these chips require a metal fill that

can distort the inductor characteristics, a 'fill stop' is placed around the inductors, as can be seen in figure 9.6. Feedlines, which are considered part of the inductor in this thesis, connect both ends of the actual spiral inductor trace to two bond pads. A metal guard ring surrounds each chip, providing mechanical stability for it. This is mentioned, since it can have an effect on the coupling to a primary inductor in the presence of a magnetic field. In this case a current is induced in the large metal loop that is formed by the guard ring, which leads to an opposing field that reduces the magnetic field reaching the small secondary inductor.

For measurement, the chips with the secondary inductors are placed on a metal cylinder which is made for this purpose and forms part of a Micromanipulator probe station. Double sided tape is used to hold the chips in place, and a tweezer is used to gently press down on the chip for improved stability of contact. An RF probe with ground signal (GS) pads (Z10-GS-150; |Z|-Probe Classic, Nickel Tip, Std Body, 10GHz, GS, SG; Cascade Microtech) which is suitable for probing Aluminum pads is connected to a vector network analyzer 'VNA' (ZVL, 9 kHz - 3 GHz; Rohde & Schwarz) with a coaxial cable, via an N-to-SMA connector. This setup is calibrated (using the calibration procedure of the VNA) at the probe tips, by using the 'open', 'short' and 'match' conditions of a commercial calibration substrate (CSR-6 50-250 GS/SG; Cascade Microtech) for the RF probes used. The probe tips are carefully touched down on the bond pads of the chip, using micromanipulators to precisely direct the movement of the RF probe tips, as well as visual feedback through the

microscope. The probe tips will move horizontally ('forward') when the probe is lowered after a first contact to the bond pad has been made - this is known as overtravel. It is possible that some aluminum oxide layer is left as an isolator between the probe and the aluminum of the bond pad when first touching down. (Aluminum pads are covered with a thin aluminum oxide layer when exposed to air.) Moving the probe up and down results in a probe tip movement forth and back, and can improve the electrical contact to the bond pad. When touching down the probe, it is important that both probe tips (G and S) are at the same height compared to the chip surface. Only then can they both touch down at the same time instead of one getting bent while the other one is still in the air, which could lead to breaking the probe. Once connected to the pads, S-parameter or Z-parameter measurements are taken with the VNA. (This is done for frequencies from 100 kHz to 3 GHz, in steps of 100 kHz up to 12.5 MHz, and in steps of 12.5 MHz for the higher frequencies.) The measurements for each frequency are averaged over time in real-time using the average setting with an average factor of 100 on the VNA in order to reduce fluctuations over time. A picture of the touched down probe tips can be seen in figure 9.8.

## 9.4 Analysis

The calculated coupling coefficient derived from the HFSS simulation is compared to the estimation based on the diameter.

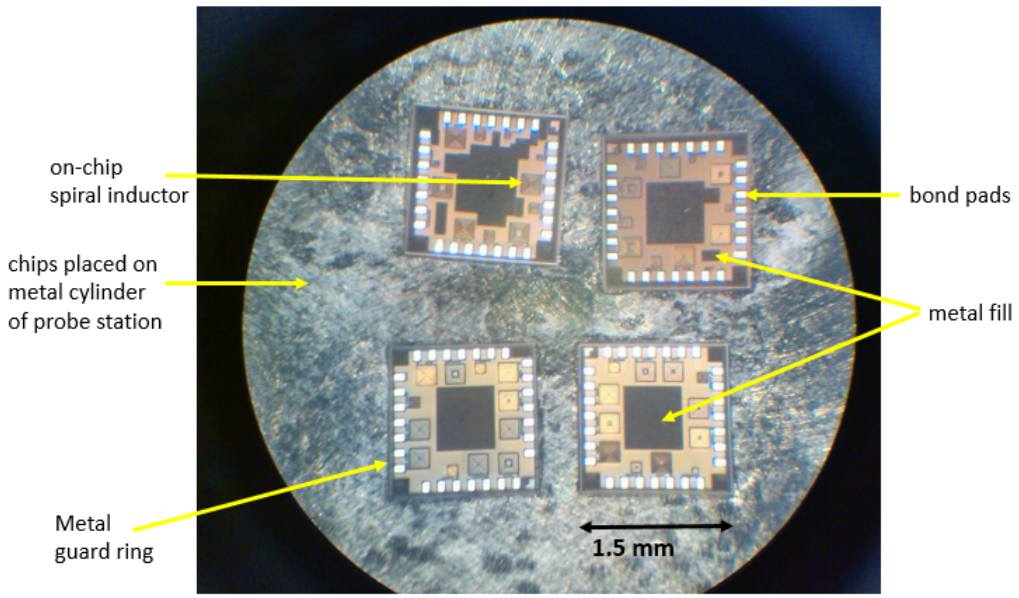


**Figure 9.4:** Microscope picture of all four fabricated inductor design chips. The dark shapes in the middle of each chip are metal fill required for the fabrication of the chips. The inductors are placed along the border of the chip to reduce the length of the required feedlines to connect to the pads.

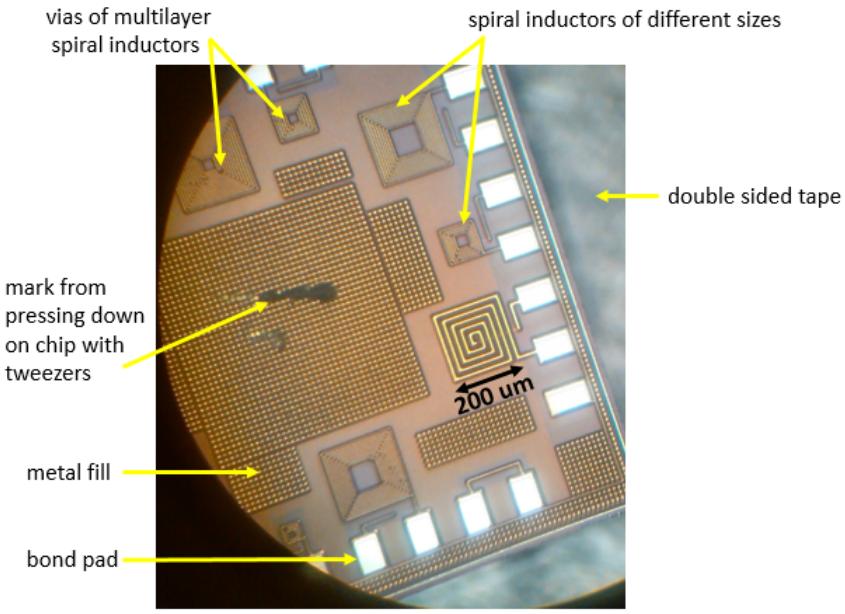


**Figure 9.5:** Closer view of part of one of the chips. Double sided tape is used to secure chip in place. Tweezer is used to press down on chip to help secure contact to tape.

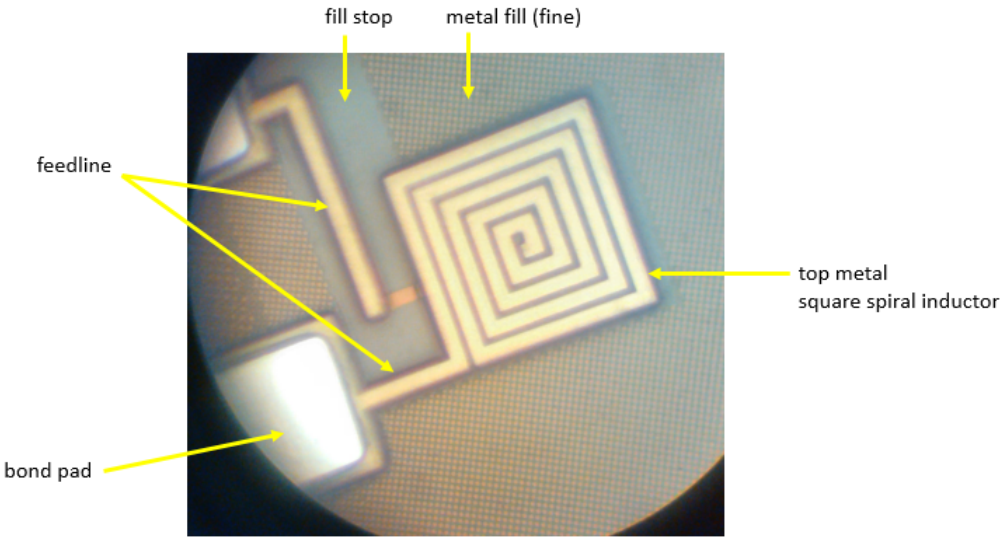


**Figure 9.6:** Microscope picture of fabricated inductor design. Fill-stop can be seen as light blue.

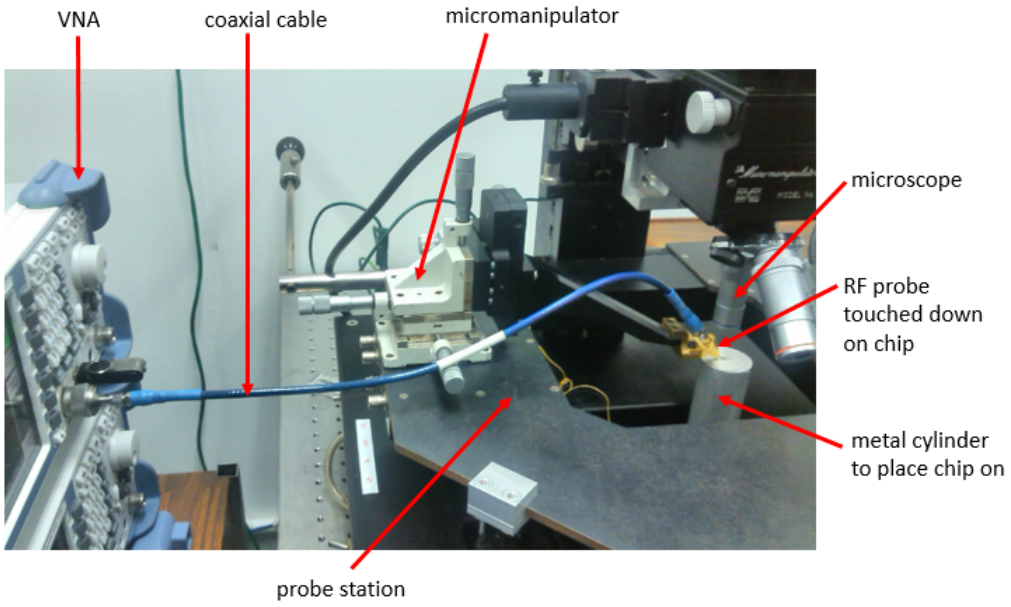


**Figure 9.7:** Measurement setup including VNA, coaxial cable, micromanipulator, and RF probe touched down using visual control through the microscope.

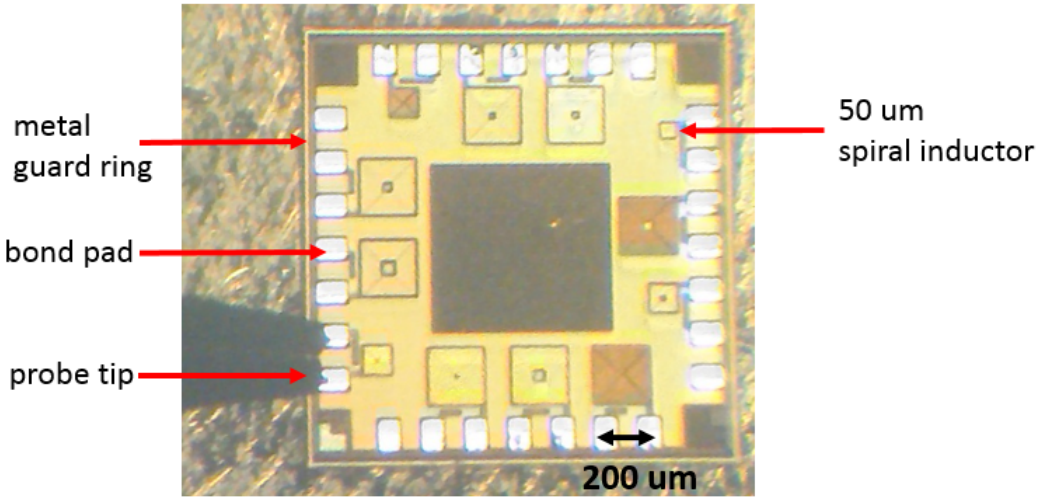


**Figure 9.8:** RF probe tips (GS) touching down on aluminum bond pads of chip with various secondary inductors.

The simulated one-port models of the primary and secondary inductors, as well as the measured one-port models of the secondary inductors, are each converted into an effective series resistance and series inductance at the frequency of interest.

An estimation of power delivery to a secondary load of 3 $k\Omega$ is made for a RMS primary current of 0.316 A according to equation 8.16. (This secondary load is the average of the simulated impedance (=voltage/current) of the neural implant circuit over time. This primary current is the expected maximal current for a 5 W power amplifier with a 50 $\Omega$ load connected to it.)

# Chapter 10

# Results and Conclusion

## 10.1 Calculation

The optimal primary inductor diameters resulting from calculations based on equation 8.24 are shown for different separation distances in figure 10.2. Corresponding coupling coefficient estimations based on equation 8.26 for a setup with a center aligned 200 um secondary inductor are shown for different separation distances in figure 10.3. Figure 10.1 shows coupling coefficients for the separation distances and secondary inductor diameters investigated.

| dz(mm) \ d2 | 50 um | 100 um | 200 um | 300 um |
|---|---|---|---|---|
| 1 | 0,001279 | 0,003619 | 0,010236 | 0,018804 |
| 2 | 0,000452 | 0,001279 | 0,003619 | 0,006648 |
| 3 | 0,000246 | 0,000696 | 0,00197 | 0,003618 |
| 5 | 0,000114 | 0,000324 | 0,000915 | 0,001682 |
| 10 | 4,05E-05 | 0,000114 | 0,000324 | 0,000595 |

**Figure 10.1:** Coupling coefficients for different separation distances dz and secondary diameters d2.

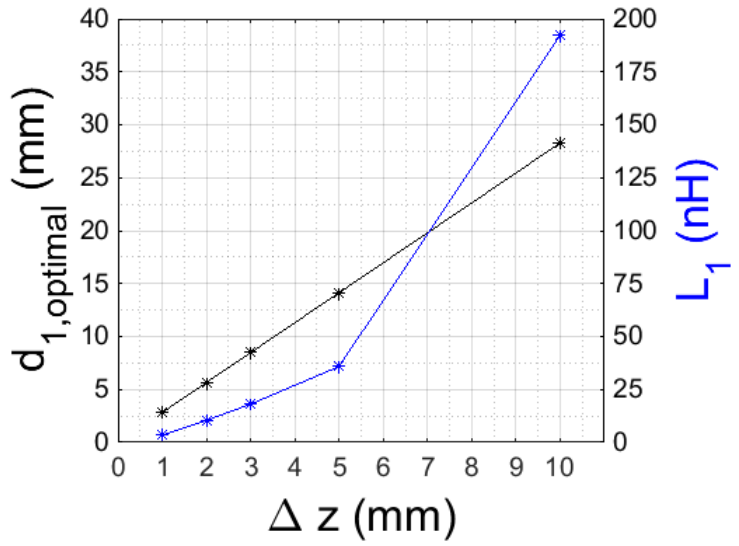


**Figure 10.2:** The estimated optimal diameter of a primary inductor for different separation distances between primary and secondary inductors is shown in black. The simulated effective inductance for a single turn octagon inductor with that optimal diameter (and a 200 um trace width) is shown in blue.

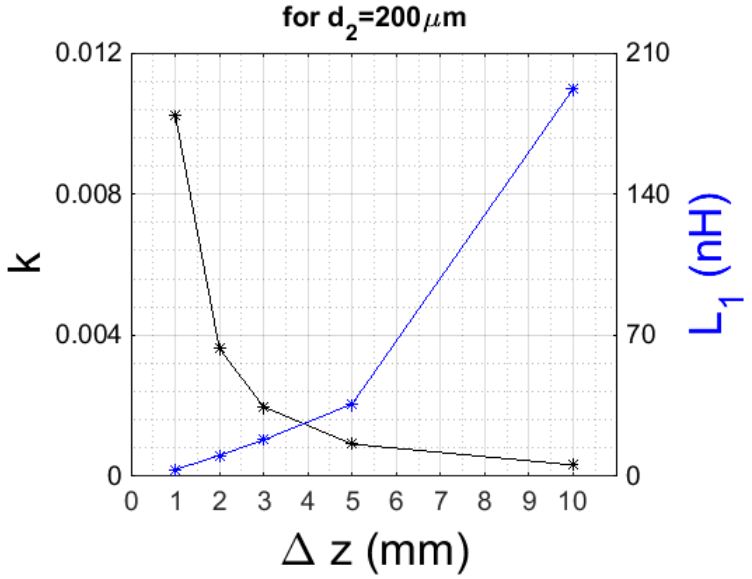


**Figure 10.3:** The estimated coupling coefficient k between a primary inductor of the optimal diameter for different separation distances, and a 200 um diameter secondary inductor is shown in black. The simulated effective inductance for a single turn octagon primary inductor with that optimal diameter (and a 200 um trace width) is shown in blue.

## 10.2 Simulation

### 10.2.1 Primary Inductor

The effective inductance (at 900 MHz) of the simulated primary inductors with the calculated optimal diameters for the given separation distances, is plotted for different separation distances between primary and secondary inductor in figures 10.2 and 10.3, along with this diameter and the estimated coupling coefficient for inductive coupling to a 200 um diameter secondary inductor. The effect of the primary inductor in the power estimation formula (equation 8.16) is limited to the product of the square of the coupling coefficient and the effective primary inductance. This product is plotted in figure 10.4 for different separation distances. The squared influence of the coupling coefficient leads to a rapid decrease of this product for an increase in separation distance. Accordingly, the shape is very similar to that of the coupling coefficient seen in figure 10.3.

Looking at the current density distribution shown in figure 10.5 for a primary inductor of an optimal diameter for 1 mm separation distance, it can be seen that the phase of the current is constant along the trace for a frequency of 900 MHz. However, this is no longer the case for a frequency of 15 GHz and current crowding with a non-homogenous current density distribution along the trace occurs. The same effect will occur at 900 MHz for primary inductors with trace lengths that are no longer electrically small at this frequency, e.g. for trace lengths that are 15 times

longer than the one plotted here. This effect becomes important at larger separation distances where larger inductors are required, or for multiple-turn inductors, and can be addressed by using segmented loops as described in section 8.3.3.2.

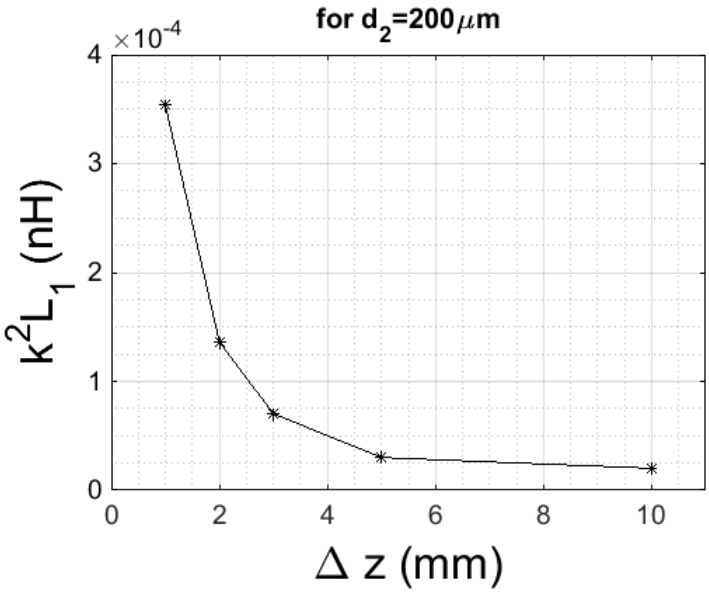


**Figure 10.4:** Product of the square of estimated coupling coefficient and the simulated inductance of the optimally sized primary inductor, for different separation distances between this primary inductor and a 200 um inductor at perfect parallel and centered alignment of inductors. This factor scales the power delivered to the load, and is the only part dependent on the primary inductor in the model used.

### 10.2.2 Secondary Inductor

The simulated effective series resistance and effective series inductance of the investigated inductor designs is shown for a frequency of 900 MHz in figure 10.6.

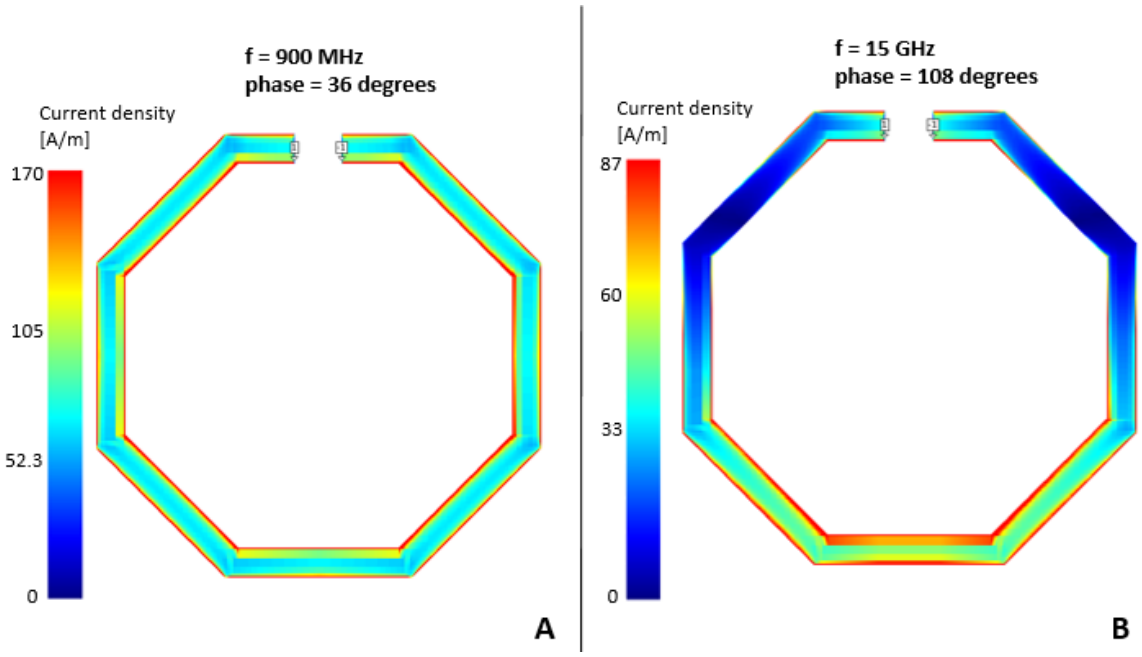


**Figure 10.5:** Current distribution on the primary inductor for 1 mm separation distance at different frequencies for a 1 V stimulation at the port at 900 MHz and 15 GHz. The phase that yielded the highest A/m values is shown here, but similar patterns could be seen at the other phases for the respective inductors. The current amplitude is constant along the entire spiral inductor for lower frequencies, allowing for the generation of a high magnetic field when the current is maximal all along the trace. On the other hand, the phase and thus amplitude of the current changes along the trace length at a higher frequency of 15 GHz. In this case, the magnetic field only gets generated by high current flow on some parts of the traces at once, which leads to a lower magnetic field than could otherwise be achieved.

| layers | d [um] | w [um] | s [um] | n | R_sim [ohm] | R_meas [ohm] | L_sim [nH] | L_meas [nH] | P_sim [uW] | P_meas [uW] |
|---|---|---|---|---|---|---|---|---|---|---|
| A (1 layer) | 300 | 5 | 4 | 16 | 17,20 | - | 39,62 | - | 49,995383 | - |
| A (1 layer) | 200 | 4 | 2,8 | 13 | 12,33 | 17,39 | 19,53 | 18,90 | 7,601784 | 4,120056 |
| A (1 layer) | 200 | 4 | 2,8 | 12 | 12,05 | 16,27 | 19,18 | 18,49 | 7,587202 | 4,371047 |
| A (1 layer) | 200 | 4 | 2,8 | 14 | 12,58 | 17,10 | 19,65 | 18,95 | 7,460794 | 4,260024 |
| A (1 layer) | 200 | 5 | 3 | 10 | 8,27 | 11,72 | 13,82 | 13,23 | 6,813059 | 3,444614 |
| A (1 layer) | 200 | 5,2 | 2,8 | 11 | 8,56 | 11,65 | 14,09 | 13,43 | 6,731660 | 3,609004 |
| A (1 layer) | 200 | 2 | 2,8 | 18 | 33,88 | 47,54 | 39,82 | 38,64 | 6,715179 | 3,928564 |
| A (1 layer) | 200 | 2 | 2,8 | 19 | 34,34 | 47,69 | 40,15 | 38,84 | 6,686264 | 3,950431 |
| A (1 layer) | 200 | 5 | 3 | 12 | 8,73 | 12,68 | 14,23 | 13,65 | 6,665340 | 3,243154 |
| A (1 layer) | 200 | 2 | 2,8 | 16 | 32,50 | 45,43 | 38,33 | 37,16 | 6,658952 | 3,889763 |
| A (1 layer) | 200 | 2 | 2,8 | 20 | 34,61 | 46,61 | 40,22 | 38,94 | 6,637752 | 4,110005 |
| A (1 layer) | 200 | 5,2 | 2,8 | 12 | 8,76 | 12,11 | 14,15 | 13,51 | 6,553397 | 3,421276 |
| A (1 layer) | 200 | 2 | 2,8 | 14 | 30,53 | 40,07 | 35,58 | 34,06 | 6,374528 | 3,941650 |
| A (1 layer) | 200 | 7 | 3 | 10 | 5,23 | 8,03 | 9,09 | 8,63 | 5,510726 | 2,265407 |
| A (1 layer) | 200 | 4 | 4 | 12 | 11,07 | 14,58 | 14,68 | 14,00 | 4,858076 | 2,709029 |
| A (1 layer) | 200 | 4 | 4 | 8 | 9,52 | 12,16 | 12,59 | 11,93 | 4,352767 | 2,490660 |
| A (1 layer) | 200 | 5 | 5 | 10 | 7,39 | 10,08 | 9,63 | 9,14 | 3,491600 | 1,743898 |
| A (1 layer) | 200 | 5,2 | 5,2 | 8 | 6,65 | 8,96 | 8,81 | 8,36 | 3,350359 | 1,699300 |
| A,B,D (3 layer) | 200 | 2 | 6 | 11 | 388,72 | 964,87 | 129,73 | 91,83 | 1,855460 | 0,190924 |
| A,B,D (3 layer) | 200 | 2 | 6 | 12 | 395,11 | 983,30 | 131,33 | 92,18 | 1,853565 | 0,186313 |
| A,B,D (3 layer) | 200 | 2 | 6 | 8 | 335,47 | 713,42 | 110,78 | 90,04 | 1,714908 | 0,312945 |
| A (1 layer) | 200 | 2 | 6 | 8 | 18,97 | 22,18 | 13,71 | 12,37 | 1,607813 | 0,916904 |
| A (1 layer) | 200 | 10 | 10 | 5 | 2,29 | 3,34 | 2,81 | 2,66 | 1,081070 | 0,445726 |
| A,B,C,D,E (5 layer) | 100 | 2 | 6 | 4 | 143,24 | 215,36 | 36,35 | 33,97 | 0,066508 | 0,025931 |
| A (1 layer) | 100 | 2 | 2,8 | 9 | 9,92 | 12,42 | 5,28 | 4,87 | 0,048429 | 0,024644 |
| A (1 layer) | 100 | 2 | 2,8 | 10 | 10,19 | 12,25 | 5,34 | 4,92 | 0,047443 | 0,026047 |
| A (1 layer) | 100 | 5,2 | 2,8 | 6 | 2,89 | 3,92 | 1,97 | 1,92 | 0,030680 | 0,015459 |
| A (1 layer) | 100 | 7 | 3 | 5 | 1,82 | 2,57 | 1,30 | 1,27 | 0,022350 | 0,010629 |
| A (1 layer) | 100 | 4 | 4 | 6 | 3,81 | 4,79 | 2,10 | 2,01 | 0,021199 | 0,011930 |
| A,B,D (3 layer) | 100 | 2 | 6 | 6 | 86,24 | 121,79 | 15,65 | 14,36 | 0,016630 | 0,006608 |
| A,B,D (3 layer) | 100 | 2 | 6 | 5 | 82,18 | 116,23 | 14,94 | 13,71 | 0,015992 | 0,006327 |
| A,B,D (3 layer) | 100 | 2 | 6 | 4 | 72,97 | 101,35 | 13,18 | 12,13 | 0,014017 | 0,005779 |
| A,B,C,D,E (5 layer) | 50 | 2 | 6 | 2 | 37,38 | 52,05 | 4,88 | 4,65 | 0,000352 | 0,000158 |
| A (1 layer) | 50 | 2 | 2,8 | 5 | 4,20 | 5,24 | 0,81 | 0,89 | 0,000128 | 0,000108 |
| A,B,D (3 layer) | 50 | 2 | 6 | 3 | 24,34 | 34,04 | 2,24 | 2,24 | 0,000081 | 0,000041 |
| A,B,D (3 layer) | 50 | 2 | 6 | 2 | 20,40 | 28,03 | 1,82 | 1,82 | 0,000062 | 0,000033 |
| A (1 layer) | 50 | 4 | 4 | 3 | 1,73 | 2,29 | 0,31 | 0,49 | 0,000044 | 0,000097 |
| A (1 layer) | 50 | 5,2 | 2,8 | 3 | 1,37 | 1,91 | 0,26 | 0,42 | 0,000040 | 0,000086 |

**Figure 10.6:** Simulated and measured effective series resistance and inductance of studied secondary inductors at 900 MHz, as well as estimated power delivered to a $3k\Omega$ load at 5 mm distance for $I_{RMS} = 0.316A$. Sorted by power estimate based on simulation. This table has commas to separate between integers and decimals. d=diameter, w=trace width, s=trace spacing, n=number of turns, R=effective series resistance, L=effective series inductance, P=estimated power delivered to load using equation 8.16, sim=based on simulation of secondary inductor, meas= based on measurement of secondary inductor.

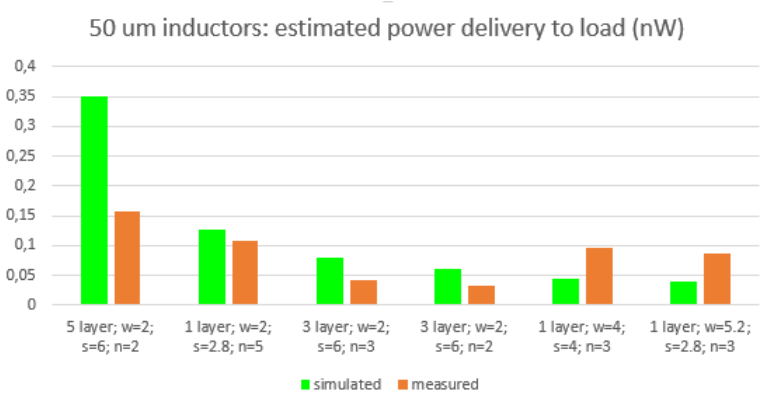


**Figure 10.7:** Estimated or expected inductive power delivery to a 3 kΩ load for 50 um diameter secondary inductors at 5 mm separation distance from a primary inductor with $I_{RMS} = 0.316A$ at 900 MHz transmission frequency, using equation 8.16. This estimation is based on simulation and measurement data of the secondary inductors. Sorted by power estimate based on simulation. Refer to figure 10.6 for details.

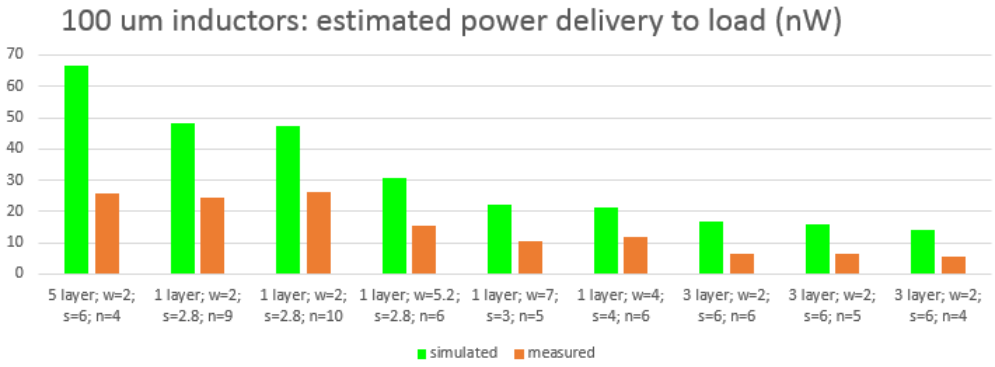


**Figure 10.8:** Estimated or expected inductive power delivery to a 3 kΩ load for 100 um diameter secondary inductors at 5 mm separation distance from a primary inductor with $I_{RMS} = 0.316A$ at 900 MHz transmission frequency, using equation 8.16. This estimation is based on simulation and measurement data of the secondary inductors. Sorted by power estimate based on simulation. Refer to figure 10.6 for details.

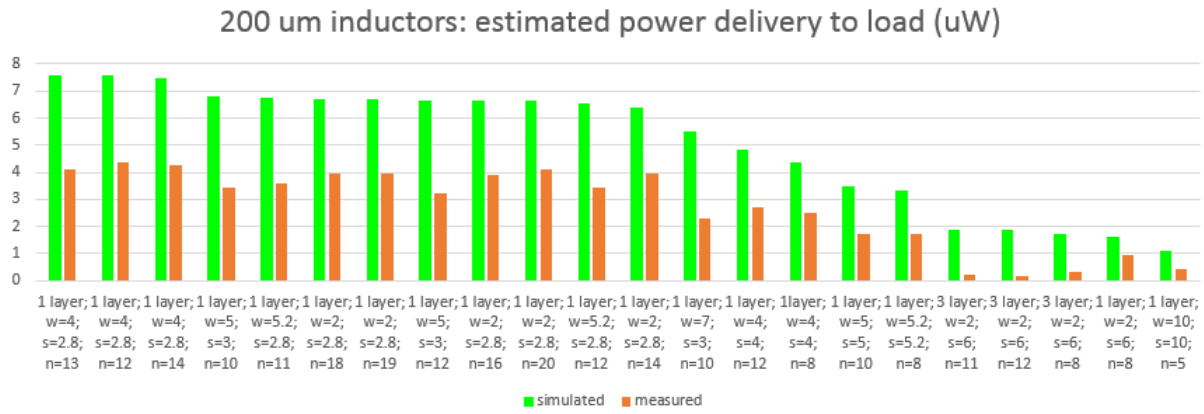


**Figure 10.9:** Estimated or expected inductive power delivery to a 3 kΩ load for 200 um diameter secondary inductors at 5 mm separation distance from a primary inductor with $I_{RMS} = 0.316A$ at 900 MHz transmission frequency, using equation 8.16. This estimation is based on simulation and measurement data of the secondary inductors. Sorted by power estimate based on simulation. Refer to figure 10.6 for details.

### 10.2.3 Coupling Coefficient

The HFSS simulation yielded $Im\{Z_{11}\} = 119.925578$ , $Im\{Z_{22}\} = 3.629318$ and $|Z_{21}| = 0.025760$. According to equation 8.15 this corresponds to a coupling coefficient of 0.0012347 between the primary and secondary inductor. The separation distance between primary and secondary inductor here is 5 mm, and the secondary square inductor with a single loop has a diameter of 300 um.

## 10.3 Bench Top Experimentation

### 10.3.1 Secondary Inductor

The effective series resistance and effective series inductance of the investigated inductor designs is shown for a frequency of 900 MHz in figure 10.6. The inductance values resulting from Sonnet software simulation are very similar to the measured values. This is very useful, since it means that a high trust can be put into the simulations for future designs. It can, however, be seen that the measured resistance is typically higher than the simulated ones. This could be due to poor probing with a high contact resistance between RF probe and inductor pads, which is usually due to a thin layer of Aluminum Oxide forming on the Aluminum surface. Other reasons for this added resistance in the measurements could be a high loss in the substrate on chip (especially, since intrinsic silicon was used in the simulations), or fabrication tolerances. These reasons seem to explain the increase in resistance better, since the increase in resistance is dependent on the simulated restistance. For most inductors, the measured resistance is around 0.4 times higher than the simulated one, showing the resistance dependence of this increase.

## 10.4 Analysis

The estimated power delivery to a 3 $k\Omega$ load can be seen for different secondary inductor sizes and designs in figures 10.7, 10.8 and 10.8. The separation distance between primary and secondary inductors was set to 5mm, and an ideal primary inductor diameter of 14.14 mm was determined for this. A simulated octagonal inductor with 3 mm trace width of this dimension had a primary inductance of L=9.6 nH. The primary current is another very crucial parameter in determining the delivered power. Here, an estimate of the RMS current that delivers 5W to a 50 $\Omega$ resistance was chosen as this current. This was based on the 5 W power amplifier that is available, thus curresponding to a current of $I_{1_{RMS}} = 0.316A$.

When comparing the power delivered to different inductor sizes, it can be seen that about two orders of magnitude are added to the estimated power for doubling the outer dimension of the secondary inductor. This stresses the challenge imposed by the desired small inductor size in this project. The estimated power delivered to 50 $\mu m$ inductors and 100 $\mu m$ inductors are on the scale of one tenth of a nano Watt, and tens of nano Watts, respectively. The estimated power delivered to 200 $\mu m$ inductors is on the scale of single digit $\mu W$, which is still much lower than required. Figure 10.6 shows that the estimated power to a 300 um inductor of the specified parameters is around 50 uW. When the primary current is increased to $I_{1_{RMS}} = 1A$, this is increased to 0.5 mW which is sufficient to power the implant, even in the face of additional unexpected losses. When increasing the current to this amplitude, however,

estimating SAR values becomes of special importance to avoid tissue damage. Such an increase in current scales the delivered power with the square of the current, but does not influence the relative distribution seen in the figures 10.7, 10.8 and 10.8.

Comparing multilayer to single layer designs, it can be seen that the 5 layer inductor designs achieve the highest power delivered to load for a given inductor size (no 5 layer inductors of 200 um diameter were studied here), while the 3 layer inductor designs only perform relatively good for the simulations of the 50 um inductors. However, they perform poorly when their measured data is used in the power estimation, and in all cases studied with larger diameters.

The following can be concluded from the 200 um inductors. It can be seen, that the three inductor designs achieving highest power delivery according to the simulations, also achieve the highest power delivery according to the measured values. Minimal spacing of 2.8 um seems to be of advantage, while increasing the trace width from a minimum of 2 um to 4um (around 2 times the skin depth in aluminum at 900 MHz) increases the delivered power. Further increasing the trace width to 5.2 um is not of advantage, even when the same number of turns is kept (n=12), due to the cost of less area enclosed by the individual turns, but this depends on the load resistance (a low series resistance of the secondary inductor becomes more important at a small load resistance).

Although a high number of turns is of advantage, it is not always of advantage to maximize this number (e.g. 12 and 13 turns are better off for the w=4um, s=2.8 um

designs, compared to n=14 turns).

It is to be noted, that the the present analysis is greatly dependent on the load impedance. This is shown in figure 10.10. There is thus an optimum load for each inductor. Future efforts should include to keep the load seen by the inductor fixed and to then optimize the inductor design according to that fixed load.

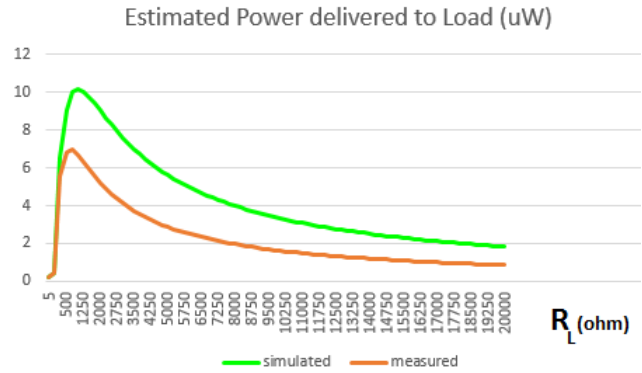


**Figure 10.10:** Estimated power delivery for best simulated 200 um inductor (w=4 um, s=2.8 um, n=13) over load resistance.

## 10.5 Conclusion

A first step towards powering the wireless neural implant by the name of micro-bead was performed. Multiple inductor designs were analyzed with respect to their ability to power the circuit.

The coupling coefficient between primary inductor and secondary inductor greatly influences the power delivered to the load, and rapidly decreases with increased separation distance. It is therefore suggested to focus on a separation distance of around

1 mm or 2 mm in the future, to improve implant powering. While estimates of the coupling coefficient seem to be close to their simulated values, use of HFSS simulations should be made to numerically optimize designs, also regarding the coupling coefficient.

The same applies to the design of the primary inductor, which was not yet optimized numerically or by iterative optimization. Segmented loop antennas are a promising solution to make electrically large primary inductors suitable for inductive power delivery at high frequencies.

Various secondary inductors were simulated and measured at 900 MHz and their effective series resistance and series inductance are shown and used for an estimate of expected power delivery to a fixed load. When comparing the power delivered to different inductor sizes, it can be seen that about two orders of magnitude are added to the estimated power for doubling the outer dimension of the secondary inductor, which is due to the coupling coefficient and the secondary inductance. This stresses the challenge imposed by the desired small inductor size in this project.

Based on the used model, as well as the simulated and measured data of the secondary inductor designs, inductors that are expected to best deliver power to a load impedance of 3 $k\Omega$ at 900 MHz are determined. The best inductor based on simulated data has w=4 um, s=2.8 um and n=13. The best inductor based on measured data has w=4 um, s=2.8 um and n=12. The difference between these inductors is one turn, all other parameters are equal. However, this result greatly depends on the

load impedance, and other inductors might be more suitable for power delivery to other load impedances.

The required resonant capacitors to form the matching circuit are assumed to be ideal here, but their parasitics are of similar importance as those of the inductors and greatly influence the choice of an optimal design.

This work is thus to be seen as a first step in approaching the goal of powering the micro-bead, however, not as the final picture.

The model used to estimate the power design here might require revisiting with regards to limitations indicated in[123] and pointed out in.[108]

Future steps should include numerical optimization of the two-port power link while adhering to SAR limits, and a combined optimization of the power link and neural implant circuit to account for the load that the secondary inductor sees at the interface to the circuit. Further, experimental two-port characterizations of the inductive power link should be performed.

Coupling is greatly dependent on the parallel alignment, as well as on the axial dislocation of the implant with respect to the primary inductor, which is expected to be non-optimal *in vivo*. The use of multiple primary inductors such as envisioned in[13] is a good approach to address this.

CMOS chips come with various disadvantages regarding power delivery to on-chip inductors, including a metal guard ring, lossy substrate, and metal fill requirements. Chip thinning[124] would not only be required to reduce the typically 250 um thick

substrate to a thickness of 100 um, but could also reduce losses. Etching the metal of the inductor out of the silicon is another approach in this respect.

Topics for a later design stage that need to be taken into account regarding the microbead include migration, i.e. far movement of the implant once it is implanted, and biocompatibility, since the body might otherwise form encapsulation around the implant, which works as electrical insulation and would thus inhibit the correct functioning of the implant.

# IV

# Conclusion

The design of instrumentation for the control of biological function requires the integration of approaches from multiple fields of science and engineering. This makes it especially challenging and requires multiple iterations of design. First steps in providing instrumentation for two applications regarding the control of cell function of non-excitable and excitable cells are presented in this thesis. Each application comes with its specific requirements for the stimulation instrumentation.

Firstly, a functioning current stimulator circuit was designed, and employed *in vivo* to study the electrical enhancement of plasmid gene therapy through iontophoresis. Various stimulation waveforms were applied through different electrode setups, and their effect on the transgene expression of two different luciferase encoding plasmids was studied. Iontophoresis improved cutaneous transgene expression for one plasmid studied (NTC 8385-Luc), while it seemed to worsen transgene expression for the other plasmid. Specifically, the most successful transfection was achieved by a 2 mA DC current and by an AC square wave current with 4 mA average current at a duty cycle of 75% and a frequency of 5 kHz. However, more animals are required to verify these results. Further steps in the circuit design involve battery powering for increased safety and portability, as well as miniaturization.

Secondly, a first step towards the inductive powering of a wireless neural stimulation implant by the name of the micro-bead was performed. Power link optimization greatly depends on the load impedance seen on the secondary side of the inductor, which was assumed to be constant here for simplification. Although inductor designs

that are expected to be optimal for power delivery to a load of $3k\Omega$ are determined here, other inductors might perform better for power delivery to other loads. Future steps should include an optimization of the implant circuit in conjunction with the power link to address this. Small separation distances between primary and secondary inductor, and thus small animal models with thin layers above the brain, are suggested to increase power delivery to the implant through the tissue. Simulations in HFSS (ANSYS) of the coupled inductors in tissue should be a significant part of the further design, since numerical optimization methods can determine a best coupling setup, and tissue safety can be verified by plotting SAR values in the simulated tissue. Two port measurements with a VNA are suggested for an experimental characterization of the power link to verify simulations.

Various lessons have been learned while conducting the research presented here. This includes the following:

Simulation tools such as Comsol, Sonnet, HFSS or Cadence are very useful in the design of instrumentation for electrical stimulation of biological tissue. High frequency design is greatly reliant on these powerful and often expensive simulation tools. Further, specialized high-frequency equipment is required for testing instrumentation at high frequencies, and every connecting wire or metal in the vicinity can have a significant influence that needs to be taken into account.

The effect of the tissue-circuit interface is very important and requires special

attention. Non-reversible reactions can occur and lead to cell death or great load impedance changes which in turn can influence the functioning of the circuit. While current in metal is in the form of electrons, it is in the form of various ions in biological tissue, and these ions can have electrochemical effects that need to be considered.

While electrical stimulation of non-excitable cells can be successful in the control of biological function, it is probable that excitable cells which are placed close to or within this non-excitable tissue, are excited by the stimulation. This can result in muscle contraction or sensation of pain etc. Therefore, stimulation frequencies which don't cause unwanted excitation at the respective stimulation levels have to be chosen.

*In vivo* experimentation requires a strict protocol to allow for a comparison of parameters in the endless parameter space of biology. The fact that each animal is different from another, requires the use of multiple animals per parameter setup, to allow for statistically significant results. Studies on single animals, as in this thesis, can merely be seen as a preliminary result to direct future investigations and they require validation in larger sample sizes, i.e. in more animals.

In conclusion, it can be said that a small contribution to the vast pool of instrumentation for the control of biological function through electrical stimulation has been made. Opportunities of two specific approaches are investigated and remaining challenges are pointed out with a suggestion of how to address them in the future.

# Bibliography

[1] M. L. Yarmush, A. Golberg, G. Serša, T. Kotnik, and D. Miklavčič, "Electroporation-based technologies for medicine: principles, applications, and challenges," *Biomedical Engineering*, vol. 16, no. 1, p. 295, 2014.

[2] A. K. Banga, S. Bose, and T. K. Ghosh, "Iontophoresis and electroporation: comparisons and contrasts," *International journal of pharmaceutics*, vol. 179, no. 1, pp. 1–19, 1999.

[3] A. S. Tucker, R. M. Fox, and R. J. Sadleir, "Biocompatible, high precision, wideband, improved howland current source with lead-lag compensation," *Biomedical Circuits and Systems, IEEE Transactions on*, vol. 7, no. 1, pp. 63–70, 2013.

[4] N. Pavselj, V. Preat, and D. Miklavcic, "A numerical model of skin electroporation as a method to enhance gene transfection in skin," in *11th Mediterranean Conference on Medical and Biomedical Engineering and Computing 2007*. Springer, 2007, pp. 597–601.

[5] T. Ngawhirunpat, T. Hatanaka, K. Katayama, H. Yoshikawa, J. Kawakami,

and I. Adachi, "Changes in electrophysiological properties of rat skin with age." *Biological and Pharmaceutical Bulletin*, vol. 25, no. 9, pp. 1192–1196, 2002.

[6] http://www.carelife.com.

[7] M. Sahin and V. Pikov, "Wireless microstimulators for neural prosthetics," *Critical Reviews in Biomedical Engineering*, vol. 39, no. 1, 2011.

[8] M. Vilarino, "Enhancing the control of upper limb myoelectric prostheses using radio frequency identification."

[9] K. Domdouzis, B. Kumar, and C. Anumba, "Radio-frequency identification (rfid) applications: A brief introduction," *Advanced Engineering Informatics*, vol. 21, no. 4, pp. 350–355, 2007.

[10] I. Guideline, "Guidelines for limiting exposure to time-varying electric, magnetic, and electromagnetic fields (up to 300 ghz)," *Health Phys*, vol. 74, no. 4, pp. 494–522, 1998.

[11] M. L. R. E.-C. Adam Khalifa, Jie Zhang, "A compact, low-power, fully analog implantable microstimulator."

[12] S. Y. R. Hui, W. Zhong, and C. K. Lee, "A critical review of recent progress in mid-range wireless power transfer," *Power Electronics, IEEE Transactions on*, vol. 29, no. 9, pp. 4500–4511, 2014.

[13] D. Ahn and M. Ghovanloo, "Optimal design of wireless power transmission links for millimeter-sized biomedical implants," 2015.

[14] M. Mark, T. Björninen, L. Ukkonen, L. Sydänheimo, and J. M. Rabaey, "Sar reduction and link optimization for mm-size remotely powered wireless implants using segmented loop antennas," in *Biomedical Wireless Technologies, Networks, and Sensing Systems (BioWireleSS), 2011 IEEE Topical Conference on.* IEEE, 2011, pp. 7–10.

[15] C.-C. Tang, C.-H. Wu, and S.-I. Liu, "Miniature 3-d inductors in standard cmos process," *Solid-State Circuits, IEEE Journal of*, vol. 37, no. 4, pp. 471–480, 2002.

[16] S. D. Patil, D. G. Rhodes, and D. J. Burgess, "Dna-based therapeutics and dna delivery systems: a comprehensive review," *The AAPS journal*, vol. 7, no. 1, pp. E61–E77, 2005.

[17] D. S. Strayer, R. Akkina, B. A. Bunnell, B. Dropulic, V. Planelles, R. J. Pomerantz, J. J. Rossi, and J. A. Zaia, "Current status of gene therapy strategies to treat hiv/aids," *Molecular therapy*, vol. 11, no. 6, pp. 823–842, 2005.

[18] M. H. Tuszynski, L. Thal, M. Pay, D. P. Salmon, R. Bakay, P. Patel, A. Blesch, H. L. Vahlsing, G. Ho, G. Tong *et al.*, "A phase 1 clinical trial of nerve growth factor gene therapy for alzheimer disease," *Nature medicine*, vol. 11, no. 5, pp. 551–555, 2005.

[19] G. U. Dachs, G. J. Dougherty, I. J. Stratford, and D. J. Chaplin, "Targeting gene therapy to cancer: a review." *Oncology research*, vol. 9, no. 6-7, pp. 313–325, 1996.

[20] L. L. Nielsen and D. C. Maneval, "P53 tumor suppressor gene therapy for cancer." *Cancer gene therapy*, vol. 5, no. 1, pp. 52–63, 1997.

[21] J. Zabner, L. A. Couture, R. J. Gregory, S. M. Graham, A. E. Smith, and M. J. Welsh, "Adenovirus-mediated gene transfer transiently corrects the chloride transport defect in nasal epithelia of patients with cystic fibrosis," *Cell*, vol. 75, no. 2, pp. 207–216, 1993.

[22] R. Pawliuk, K. A. Westerman, M. E. Fabry, E. Payen, R. Tighe, E. E. Bouhassira, S. A. Acharya, J. Ellis, I. M. London, C. J. Eaves *et al.*, "Correction of sickle cell disease in transgenic mouse models by gene therapy," *Science*, vol. 294, no. 5550, pp. 2368–2371, 2001.

[23] G. L. Brown, L. B. Nanney, J. Griffen, A. B. Cramer, J. M. Yancey, L. J. Curtsinger III, L. Holtzin, G. S. Schultz, M. J. Jurkiewicz, and J. B. Lynch, "Enhancement of wound healing by topical treatment with epidermal growth factor," *New England Journal of Medicine*, vol. 321, no. 2, pp. 76–79, 1989.

[24] D. Mathieu, J.-C. Linke, and F. Wattel, "Non-healing wounds," in *Handbook on hyperbaric medicine*. Springer, 2006, pp. 401–428.

[25] L. Liu, G. P. Marti, X. Wei, X. Zhang, H. Zhang, Y. V. Liu, M. Nastai, G. L. Semenza, and J. W. Harmon, "Age-dependent impairment of hif-1$\alpha$ expression in diabetic mice: Correction with electroporation-facilitated gene therapy increases wound healing, angiogenesis, and circulating angiogenic cells," *Journal of cellular physiology*, vol. 217, no. 2, pp. 319–327, 2008.

[26] K. A. Mace, D. H. Yu, K. Z. Paydar, N. Boudreau, and D. M. Young, "Sustained expression of hif-1$\alpha$ in the diabetic environment promotes angiogenesis and cutaneous wound repair," *Wound repair and regeneration*, vol. 15, no. 5, pp. 636–645, 2007.

[27] S. E. Gardner, R. A. Frantz, and F. L. Schmidt, "Effect of electrical stimulation on chronic wound healing: a meta-analysis," *Wound Repair and Regeneration*, vol. 7, no. 6, pp. 495–503, 1999.

[28] S. I. Reger, A. Hyodo, S. Negami, H. E. Kambic, and V. Sahgal, "Experimental wound healing with electrical stimulation," *Artificial organs*, vol. 23, no. 5, pp. 460–462, 1999.

[29] M. Ferguson, C. Byrnes, L. Sun, G. Marti, P. Bonde, M. Duncan, and J. W. Harmon, "Wound healing enhancement: electroporation to address a classic problem of military medicine," *World journal of surgery*, vol. 29, no. 1, pp. S55–S59, 2005.

[30] G. Chu, H. Hayakawa, and P. Berg, "Electroporation for the efficient transfec-

tion of mammalian cells with dna," *Nucleic acids research*, vol. 15, no. 3, pp. 1311–1326, 1987.

[31] T. Asahara, K. Shinomiya, T. Naito, and H. Shiota, "Induction of gene into the rabbit eye by iontophoresis: preliminary report," *Japanese journal of ophthalmology*, vol. 45, no. 1, pp. 31–39, 2001.

[32] A. Manosroi, N. Khositsuntiwong, F. Götz, R. G. Werner, and J. Manosroi, "Transdermal enhancement through rat skin of luciferase plasmid dna loaded in elastic nanovesicles: Biological recognition and interactions of liposomes," *Journal of liposome research*, vol. 19, no. 2, pp. 91–98, 2009.

[33] A. Hill, G. Baker, and G. Jansen, "Mechanism of action of iontophoresis in the treatment of palmar hyperhidrosis." *Cutis*, vol. 28, no. 1, pp. 69–70, 1981.

[34] R. O. Potts, J. A Tamada, and M. J Tierney, "Glucose monitoring by reverse iontophoresis," *Diabetes/metabolism research and reviews*, vol. 18, no. S1, pp. S49–S53, 2002.

[35] A. K. Banga and P. C. Panus, "Clinical applications of lontophoretic devices in rehabilitation medicine," *Critical Reviews in Physical and Rehabilitation Medicine*, vol. 10, no. 2, 1998.

[36] J. A. Vernon, M. R. Kaufman, R. E. Brummett, and H. G. Bender, "Ion-

tophoresis apparatus for applying local anesthetics," Nov. 16 1976, uS Patent 3,991,755.

[37] J. P. Howard, T. R. Drake, and D. L. Kellogg, "Effects of alternating current iontophoresis on drug delivery," *Archives of physical medicine and rehabilitation*, vol. 76, no. 5, pp. 463–466, 1995.

[38] C. Ching, I. Camilleri, and P. Connolly, "A low-cost, programmable device for versatile current delivery in iontophoresis applications," *Sensors and Actuators B: Chemical*, vol. 106, no. 2, pp. 534–540, 2005.

[39] G. Yan, S. K. Li, and W. I. Higuchi, "Evaluation of constant current alternating current iontophoresis for transdermal drug delivery," *Journal of controlled release*, vol. 110, no. 1, pp. 141–150, 2005.

[40] B. W. Barry, "Novel mechanisms and devices to enable successful transdermal drug delivery," *European journal of pharmaceutical sciences*, vol. 14, no. 2, pp. 101–114, 2001.

[41] P. M. Elias, "Stratum corneum defensive functions: an integrated view," *Journal of General Internal Medicine*, vol. 20, no. 5, pp. 183–200, 2005.

[42] S.-K. Han, *Innovations and Advances in Wound Healing*. Springer, 2015.

[43] T. Velnar, T. Bailey, and V. Smrkolj, "The wound healing process: an overview

of the cellular and molecular mechanisms," *Journal of International Medical Research*, vol. 37, no. 5, pp. 1528–1542, 2009.

[44] W. X. Hong, M. S. Hu, M. Esquivel, G. Y. Liang, R. C. Rennert, A. McArdle, K. J. Paik, D. Duscher, G. C. Gurtner, H. P. Lorenz *et al.*, "The role of hypoxia-inducible factor in wound healing," *Advances in wound care*, vol. 3, no. 5, pp. 390–399, 2014.

[45] W. A. Dorsett-Martin, "Rat models of skin wound healing: a review," *Wound Repair and Regeneration*, vol. 12, no. 6, pp. 591–599, 2004.

[46] Y. N. Kalia, A. Naik, J. Garrison, and R. H. Guy, "Iontophoretic drug delivery," *Advanced drug delivery reviews*, vol. 56, no. 5, pp. 619–658, 2004.

[47] Q. Xu, R. P. Kochambilli, Y. Song, J. Hao, W. I. Higuchi, and S. K. Li, "Effects of alternating current frequency and permeation enhancers upon human epidermal membrane," *International journal of pharmaceutics*, vol. 372, no. 1, pp. 24–32, 2009.

[48] D. R. Merrill, M. Bikson, and J. G. Jefferys, "Electrical stimulation of excitable tissue: design of efficacious and safe protocols," *Journal of neuroscience methods*, vol. 141, no. 2, pp. 171–198, 2005.

[49] A. Straume, G. Oftedal, and A. Johnsson, "Skin temperature increase caused by

a mobile phone: a methodological infrared camera study," *Bioelectromagnetics*, vol. 26, no. 6, pp. 510–519, 2005.

[50] P. Bertemes-Filho, B. Brown, and A. Wilson, "A comparison of modified howland circuits as current generators with current mirror type circuits," *Physiological Measurement*, vol. 21, no. 1, p. 1, 2000.

[51] T. Instruments, "A comprehensive study of the howland current pump," *AN-1515 A*, 2008.

[52] J. Ho, P. Minhas, M. Bikson, A. Datta, V. Bansal, J. Patel, D. Steingart, J. Vega, and L. Parra, "Methods for reducing discomfort during electrostimulation, and compositions and apparatus therefor," Dec. 30 2009, uS Patent App. 13/142,140.

[53] S. K. Kalia, T. Sankar, and A. M. Lozano, "Deep brain stimulation for parkinson's disease and other movement disorders," *Current opinion in neurology*, vol. 26, no. 4, pp. 374–380, 2013.

[54] Y. Li and D. J. Mogul, "Electrical control of epileptic seizures," *Journal of Clinical Neurophysiology*, vol. 24, no. 2, pp. 197–204, 2007.

[55] V. Sturm, D. Lenartz, A. Koulousakis, H. Treuer, K. Herholz, J. C. Klein, and J. Klosterkötter, "The nucleus accumbens: a target for deep brain stimula-

tion in obsessive–compulsive-and anxiety-disorders," *Journal of chemical neuroanatomy*, vol. 26, no. 4, pp. 293–299, 2003.

[56] H. S. Mayberg, A. M. Lozano, V. Voon, H. E. McNeely, D. Seminowicz, C. Hamani, J. M. Schwalb, and S. H. Kennedy, "Deep brain stimulation for treatment-resistant depression," *Neuron*, vol. 45, no. 5, pp. 651–660, 2005.

[57] W. L. Rutten, "Selective electrical interfaces with the nervous system," *Annual Review of Biomedical Engineering*, vol. 4, no. 1, pp. 407–452, 2002.

[58] D. Seo, J. M. Carmena, J. M. Rabaey, E. Alon, and M. M. Maharbiz, "Neural dust: An ultrasonic, low power solution for chronic brain-machine interfaces," *arXiv preprint arXiv:1307.2196*, 2013.

[59] D. Seo, J. M. Carmena, J. M. Rabaey, M. M. Maharbiz, and E. Alon, "Model validation of untethered, ultrasonic neural dust motes for cortical recording," *Journal of neuroscience methods*, vol. 244, pp. 114–122, 2015.

[60] W. Biederman, D. J. Yeager, N. Narevsky, A. C. Koralek, J. M. Carmena, E. Alon, and J. M. Rabaey, "A fully-integrated, miniaturized (0.125 $mm^2$) 10.5 $\mu$w wireless neural sensor," *Solid-State Circuits, IEEE Journal of*, vol. 48, no. 4, pp. 960–970, 2013.

[61] D. Yeager, W. Biederman, N. Narevsky, E. Alon, and J. Rabaey, "A fully-

integrated 10.5$\mu$w miniaturized (0.125 mm 2) wireless neural sensor," in *2012 Symposium on VLSI Circuits (VLSIC)*, 2012.

[62] E. Moradi, S. Amendola, T. Bjorninen, L. Sydanheimo, J. M. Carmena, J. M. Rabaey, and L. Ukkonen, "Backscattering neural tags for wireless brain-machine interface systems," *Antennas and Propagation, IEEE Transactions on*, vol. 63, no. 2, pp. 719–726, 2015.

[63] M. Mark, T. Björninen, Y. D. Chen, S. Venkatraman, L. Ukkonen, L. Sydänheimo, J. M. Carmena, and J. M. Rabaey, "Wireless channel characterization for mm-size neural implants," in *Engineering in Medicine and Biology Society (EMBC), 2010 Annual International Conference of the IEEE.* IEEE, 2010, pp. 1565–1568.

[64] W. J. Heetderks, "Rf powering of millimeter-and submillimeter-sized neural prosthetic implants," *Biomedical Engineering, IEEE Transactions on*, vol. 35, no. 5, pp. 323–327, 1988.

[65] M. Zargham and P. G. Gulak, "Maximum achievable efficiency in near-field coupled power-transfer systems," *Biomedical Circuits and Systems, IEEE Transactions on*, vol. 6, no. 3, pp. 228–245, 2012.

[66] M. Usami, "An ultra-small rfid chip: $\mu$-chip," in *Advanced System Integrated Circuits 2004. Proceedings of 2004 IEEE Asia-Pacific Conference on.* IEEE, 2004, pp. 2–5.

[67] T. Hornyak, "Rfid powder," *Scientific American*, vol. 298, no. 2, pp. 68–71, 2008.

[68] M. Usami, "Powder rfid chip technology," in *APCCAS 2008-2008 IEEE Asia Pacific Conference on Circuits and Systems*, 2008.

[69] P. Burke and C. Rutherglen, "Towards a single-chip, implantable rfid system: is a single-cell radio possible?" *Biomedical microdevices*, vol. 12, no. 4, pp. 589–596, 2010.

[70] J. N. Burghartz, D. Edelstein, M. Soyuer, H. Ainspan, and K. A. Jenkins, "Rf circuit design aspects of spiral inductors on silicon," *Solid-State Circuits, IEEE Journal of*, vol. 33, no. 12, pp. 2028–2034, 1998.

[71] J. N. Burghartz, M. Soyuer, and K. A. Jenkins, "Microwave inductors and capacitors in standard multilevel interconnect silicon technology," *Microwave Theory and Techniques, IEEE Transactions on*, vol. 44, no. 1, pp. 100–104, 1996.

[72] A. Pun, T. Yeung, J. Lau, F. J. Clement, and D. Su, "Experimental results and simulation of substrate noise coupling via planar spiral inductor in rf ics," in *Electron Devices Meeting, 1997. IEDM'97. Technical Digest., International*. IEEE, 1997, pp. 325–328.

[73] S.-C. Leong, "Design, optimization of rf spiral inductors using scalable compact

and accurate models," *Analog Integrated Circuits and Signal Processing*, vol. 37, no. 3, pp. 165–177, 2003.

[74] J. Gao and C. Yang, "Microwave modeling and parameter extraction method for multilayer on-chip inductors," *International Journal of RF and Microwave Computer-Aided Engineering*, vol. 23, no. 3, pp. 343–348, 2013.

[75] K. Tong and C. Tsui, "A physical analytical model of multilayer on-chip inductors," *Microwave Theory and Techniques, IEEE Transactions on*, vol. 53, no. 4, pp. 1143–1149, 2005.

[76] J. N. Burghartz, A. E. Ruehli, K. A. Jenkins, M. Soyuer, and D. Nguyen-Ngoc, "Novel substrate contact structure for high-q silicon-integrated spiral inductors," in *Electron Devices Meeting, 1997. IEDM'97. Technical Digest., International*. IEEE, 1997, pp. 55–58.

[77] B. K. Thurgood, D. J. Warren, N. M. Ledbetter, G. A. Clark, and R. R. Harrison, "A wireless integrated circuit for 100-channel charge-balanced neural stimulation," *Biomedical Circuits and Systems, IEEE Transactions on*, vol. 3, no. 6, pp. 405–414, 2009.

[78] H.-G. Rhew, J. Jeong, J. A. Fredenburg, S. Dodani, P. G. Patil, and M. P. Flynn, "A fully self-contained logarithmic closed-loop deep brain stimulation soc with wireless telemetry and wireless power management," *Solid-State Circuits, IEEE Journal of*, vol. 49, no. 10, pp. 2213–2227, 2014.

[79] H.-M. Lee, H. Park, and M. Ghovanloo, "A power-efficient wireless system with adaptive supply control for deep brain stimulation," *Solid-State Circuits, IEEE Journal of*, vol. 48, no. 9, pp. 2203–2216, 2013.

[80] M. Ghovanloo and K. Najafi, "A modular 32-site wireless neural stimulation microsystem," *Solid-State Circuits, IEEE Journal of*, vol. 39, no. 12, pp. 2457–2466, 2004.

[81] M. Ghovanloo, K. D. Wise, and K. Najafi, "Towards a button-sized 1024-site wireless cortical microstimulating array," in *Neural Engineering, 2003. Conference Proceedings. First International IEEE EMBS Conference on.* IEEE, 2003, pp. 138–141.

[82] S. Stoney, W. Thompson, and H. Asanuma, "Excitation of pyramidal tract cells by intracortical microstimulation: effective extent of stimulating current." *Journal of neurophysiology*, vol. 31, no. 5, pp. 659–669, 1968.

[83] S. F. Cogan, "Neural stimulation and recording electrodes," *Annu. Rev. Biomed. Eng.*, vol. 10, pp. 275–309, 2008.

[84] Z. J. Daskalakis, B. K. Christensen, P. B. Fitzgerald, and R. Chen, "Transcranial magnetic stimulation," *The Journal of neuropsychiatry and clinical neurosciences*, 2002.

[85] G. Ojemann, J. Ojemann, E. Lettich, and M. Berger, "Cortical language local-

ization in left, dominant hemisphere: an electrical stimulation mapping investigation in 117 patients," *Journal of neurosurgery*, vol. 71, no. 3, pp. 316–326, 1989.

[86] J. F. Rizzo, J. Wyatt, J. Loewenstein, S. Kelly, and D. Shire, "Methods and perceptual thresholds for short-term electrical stimulation of human retina with microelectrode arrays," *Investigative ophthalmology & visual science*, vol. 44, no. 12, pp. 5355–5361, 2003.

[87] P. Cinquin, C. Gondran, F. Giroud, S. Mazabrard, A. Pellissier, F. Boucher, J.-P. Alcaraz, K. Gorgy, F. Lenouvel, S. Mathé *et al.*, "A glucose biofuel cell implanted in rats," *PloS one*, vol. 5, no. 5, p. e10476, 2010.

[88] I. Stark, "Invited talk: Thermal energy harvesting with thermo life," in *Wearable and Implantable Body Sensor Networks, 2006. BSN 2006. International Workshop on.* IEEE, 2006, pp. 19–22.

[89] H. A. Sodano, D. J. Inman, and G. Park, "A review of power harvesting from vibration using piezoelectric materials," *Shock and Vibration Digest*, vol. 36, no. 3, pp. 197–206, 2004.

[90] B. Lewandowski, K. Kilgore, and K. Gustafson, "Feasibility of an implantable, stimulated muscle-powered piezoelectric generator as a power source for implanted medical devices," in *Energy harvesting technologies.* Springer, 2009, pp. 389–404.

[91] http://www.sonnetsoftware.com/.

[92] http://www.sonnetsoftware.com/products/sonnet-suites/how-em-works.html.

[93] R. Harrington, "Field computation by moment methods, réimprimée, illustrée ed," 1993.

[94] J. C. Rautio and R. F. Harrington, "An electromagnetic time-harmonic analysis of shielded microstrip circuits," *Microwave Theory and Techniques, IEEE Transactions on*, vol. 35, no. 8, pp. 726–730, 1987.

[95] http://www.ansys.com/products/electronics/ansys-hfss.

[96] http://resource.ansys.com/products/electronics/ansys+hfss/features/.

[97] H. Aubert, "Rfid technology for human implant devices," *Comptes Rendus Physique*, vol. 12, no. 7, pp. 675–683, 2011.

[98] D. M. Dobkin, *The RF in RFID: UHF RFID in Practice*. Newnes, 2012.

[99] D. M. Dobkin, S. M. Weigand, and N. Iyer, "Segmented magnetic antennas for near-field uhf rfid." *Microwave Journal*, vol. 50, no. 6, 2007.

[100] K. Foster, J. Schepps, R. Stoy, and H. P. Schwan, "Dielectric properties of brain tissue between 0.01 and 10 ghz," *Physics in medicine and biology*, vol. 24, no. 6, p. 1177, 1979.

[101] S. Stoecklin, T. Volk, A. Yousaf, and L. Reindl, "A maximum efficiency point tracking system for wireless powering of biomedical implants," *Procedia Engineering*, vol. 120, pp. 451–454, 2015.

[102] M. Kiani, B. Lee, P. Yeon, and M. Ghovanloo, "A q-modulation technique for efficient inductive power transmission," *Solid-State Circuits, IEEE Journal of*, vol. 50, no. 12, pp. 2839–2848, 2015.

[103] D. Ahn, M. Kiani, and M. Ghovanloo, "Enhanced wireless power transmission using strong paramagnetic response," *Magnetics, IEEE Transactions on*, vol. 50, no. 3, pp. 96–103, 2014.

[104] U.-M. Jow and M. Ghovanloo, "Modeling and optimization of printed spiral coils in air, saline, and muscle tissue environments," *Biomedical Circuits and Systems, IEEE Transactions on*, vol. 3, no. 5, pp. 339–347, 2009.

[105] Z. Duan, Y.-X. Guo, and D.-L. Kwong, "Rectangular coils optimization for wireless power transmission," *Radio Science*, vol. 47, no. 3, 2012.

[106] K. Kurokawa, "Power waves and the scattering matrix," *Microwave Theory and Techniques, IEEE Transactions on*, vol. 13, no. 2, pp. 194–202, 1965.

[107] K. Van Schuylenbergh and R. Puers, *Inductive powering: basic theory and application to biomedical systems*. Springer Science & Business Media, 2009.

[108] A. S. Poon, S. O'Driscoll, and T. H. Meng, "Optimal operating frequency

in wireless power transmission for implantable devices," in *Engineering in Medicine and Biology Society, 2007. EMBS 2007. 29th Annual International Conference of the IEEE*. IEEE, 2007, pp. 5673–5678.

[109] R. R. Harrison, P. T. Watkins, R. J. Kier, R. O. Lovejoy, D. J. Black, B. Greger, and F. Solzbacher, "A low-power integrated circuit for a wireless 100-electrode neural recording system," *Solid-State Circuits, IEEE Journal of*, vol. 42, no. 1, pp. 123–133, 2007.

[110] A. M. Sodagar, G. E. Perlin, Y. Yao, K. Najafi, and K. D. Wise, "An implantable 64-channel wireless microsystem for single-unit neural recording," *Solid-State Circuits, IEEE Journal of*, vol. 44, no. 9, pp. 2591–2604, 2009.

[111] A. S. Poon, S. O'Driscoll, and T. H. Meng, "Optimal frequency for wireless power transmission into dispersive tissue," *Antennas and Propagation, IEEE Transactions on*, vol. 58, no. 5, pp. 1739–1750, 2010.

[112] M. Weiergräber, M. Henry, J. Hescheler, N. Smyth, and T. Schneider, "Electrocorticographic and deep intracerebral eeg recording in mice using a telemetry system," *Brain research protocols*, vol. 14, no. 3, pp. 154–164, 2005.

[113] A. Y. Shih, C. Mateo, P. J. Drew, P. S. Tsai, and D. Kleinfeld, "A polished and reinforced thinned-skull window for long-term imaging of the mouse brain," *JoVE (Journal of Visualized Experiments)*, no. 61, pp. e3742–e3742, 2012.

[114] U.-M. Jow and M. Ghovanloo, "Design and optimization of printed spiral coils for efficient transcutaneous inductive power transmission," *Biomedical Circuits and Systems, IEEE Transactions on*, vol. 1, no. 3, pp. 193–202, 2007.

[115] R. Pansomboon and C. Phongcharoenpanich, "The multiple loop antenna for enhanced readability performances of near-field uhf rfid applications," *International Journal of RF and Microwave Computer-Aided Engineering*, 2016.

[116] X. Qing, C. Goh, and Z. N. Chen, "Segmented loop antenna for uhf near-field rfid applications," *Electronics Letters*, vol. 45, no. 17, pp. 872–873, 2009.

[117] Y. S. Ong, X. Qing, C. K. Goh, and Z. N. Chen, "A segmented loop antenna for uhf near-field rfid," in *Antennas and Propagation Society International Symposium (APSURSI), 2010 IEEE*. IEEE, 2010, pp. 1–4.

[118] Q. Liu, Y. Yu, and S. He, "Capacitively loaded, inductively coupled fed loop antenna with an omnidirectional radiation pattern for uhf rfid tags," *Antennas and Wireless Propagation Letters, IEEE*, vol. 12, pp. 1161–1164, 2013.

[119] H. Namba, T. Hashimoto, and M. Furumiya, "On-chip vertically coiled solenoid inductors and transformers for rf soc using 90nm cmos interconnect technology," in *Radio Frequency Integrated Circuits Symposium (RFIC), 2011 IEEE*. IEEE, 2011, pp. 1–4.

[120] J. N. Burghartz, "Progress in rf inductors on silicon-understanding substrate

losses," in *Electron Devices Meeting, 1998. IEDM'98. Technical Digest., International*. IEEE, 1998, pp. 523–526.

[121] R. P. Ribas, J. Lescot, J.-L. Leclercq, J. M. Karam, and F. Ndagijimana, "Micromachined microwave planar spiral inductors and transformers," *Microwave Theory and Techniques, IEEE Transactions on*, vol. 48, no. 8, pp. 1326–1335, 2000.

[122] K. Finkenzeller, *RFID Handbook: Radio-frequency identification fundamentals and applications*. Wiley, 1999.

[123] R. Collin, "Limitations of the thevenin and norton equivalent circuits for a receiving antenna," *Antennas and Propagation Magazine, IEEE*, vol. 45, no. 2, pp. 119–124, 2003.

[124] H. Noda, M. Usami, A. Sato, S. Terasaki, and H. Ishizaka, "Self-aligned positioning technology to connect ultra-small rfid powder-chip to an antenna," in *Electronic Components and Technology Conference (ECTC), 2011 IEEE 61st*. IEEE, 2011, pp. 1009–1014.

# Vita

Martina Charlotte Leistner was born in Germany. She received her B.Sc. degree in Biomedical Engineering with focus areas Electrical Engineering and Computer Science from Friedrich-Alexander-University Erlangen-Nuremberg, Germany, in 2014. The research for her Bachelors thesis was conducted at Johns Hopkins University, Baltimore, MD, USA. She pursued a M.S.E. degree in Biomedical Engineering at Johns Hopkins University starting in August 2014, with her main focus on Neuroengineering and Electrical Engineering. Advised by Dr. Ralph Etienne-Cummings, she is conducting research on wireless implantable devices for neural stimulation and recording, as well as electrical stimulation for gene therapy, at the Computational Sensory-Motor Systems Lab.